FRACTAL-INSPIRED SUBWAVELENGTH GEOMETRIC INCLUSIONS FOR IMPROVEMENT OF HIGH-FREQUENCY ELECTROMAGNETIC DEVICES

by

Kathryn Leigh Smith

A dissertation submitted to the faculty of
The University of North Carolina at Charlotte
in partial fulfillment of the requirements
for the degree of Doctor of Philosophy in
Electrical Engineering

Charlotte

2018

Approved by:

Dr. Ryan S. Adams

Dr. Thomas P. Weldon

Dr. Yogendra Kakad

Dr. Wesley Williams

ABSTRACT

KATHRYN LEIGH SMITH. Fractal-inspired subwavelength geometric inclusions for improvement of high-frequency electromagnetic devices. (Under the direction of DR. RYAN S. ADAMS)

This dissertation presents research results demonstrating the efficacy of fractal-inspired subwavelength geometric inclusions for improvement of high-frequency electromagnetic devices. It begins with a review of the open literature in the area of fractal applications in antennas and metamaterials. This is followed by a detailed discussion of three high-frequency electromagnetic devices that demonstrate performance improvement through incorporation of subwavelength geometric design elements.

The first of these devices is a spherical spiral metamaterial unit cell that was developed as a three-dimensional fractal expansion of the traditional split ring resonator, and is shown to be capable of producing broadband negative permeability, negative permittivity, or both, depending solely on the orientation of the unit cells with respect to the incident electric field.

The second device is a ringed rectangular patch antenna that has four resonant frequencies. All four of these operative frequencies are shown to produce similar radiation patterns, which also closely match the pattern of a traditional patch antenna. Several minor geometric modifications of the basic shape of the device are also presented, and are shown to enable modification of the number of resonances, as well as tuning of frequencies of resonance.

The third and final topic is a modified horn antenna that incorporates a spiral metamaterial as a phase-shifting device in order to achieve circularly polarized radi-

ation. The handedness of the radiated wave is shown to be tunable through simple reorientation of the loading unit cells.

In each of these cases, electrically-small geometric modification of existing device geometries is shown to greatly affect performance, either by increasing bandwidth, by inducing multiband behavior, or by enabling exotic radiation characteristics.

ACKNOWLEDGMENTS

This material is based upon work supported by the National Science Foundation under Grant No. DGE-1439650. Any opinion, findings, and conclusions or recommendations expressed in this material are those of the authors(s) and do not necessarily reflect the views of the National Science Foundation.

My sincere thanks go to the following:

To my advisor, Dr. Ryan Adams, for generously giving of his time and of his extensive technical and practical knowledge, both as a teacher and as a mentor, and for his unfailing patience and encouragement.

To the other members of my committee, Dr. Thomas Weldon, Dr. Wesley Williams, and Dr. Yogendra Kakad, for serving on my committee, and for their advice and mentorship.

To the students who have worked with me in the lab, for their collaboration in study and research, and for their friendship.

To my family - my Smith family, my Bartholomew family, my Rehobeth family, and my Sovereign Grace family - and also to the DeBoers, the Johnsons, and the Satterfields, for their invaluable support and encouragement.

Finally, to Him who is from everlasting to everlasting, who formed the earth by the word of His power, who sustains the universe by His mighty hand, and who alone teaches man knowledge; to the LORD, my Redeemer - I will praise You as long as I have being, for You have dealt wondrously with me.

TABLE OF CONTENTS

LIST OF ILLUSTRATIONS

CHAPTER 1: INTRODUCTION

The intriguing possibilities presented by the use of fractals in electromagnetics were first explored by Dwight Jaggard, who coined the term "fractal electrodynamics" in 1990 to label this field of study. In [1], Jaggard introduced the use of fractals in electromagnetic applications to induce multi-band and/or wideband performance in resonant structures. The proposed work will develop several specific applications in which fractal-inspired sub-wavelength geometric inclusions are used to improve the performance of electromagnetic structures, specifically, antennas and metamaterials.

Chapter 2 will begin in section 2.1 with an introduction to basic electromagnetic theory, where Maxwells equations will be introduced and the mechanism for wave generation and propagation discussed. This will be followed in section 2.2 by an introduction to geometric fractals, along with some examples of historical fractals and their generation techniques. The remainder of the chapter will give an overview of relevant publications from the open literature. Several publications showcasing the use of fractals in antenna engineering will be discussed in section 2.3. In section 2.4, the historical development of metamaterials will be outlined, and existing publications on fractal metamaterial unit cells will be summarized. This chapter will conclude in section 2.5 with the presentation of published literature showcasing the integration of metamaterials into horn antenna applications.

Chapter 3 will present a novel metamaterial unit cell that utilizes fractal notions

to create a three-dimensional expansion of the basic negative permeability unit cell - the split ring resonator. This new unit cell, a spherical spiral, is shown to be capable of producing negative permeability, negative permittivity, or negative index of refraction, depending on the orientation of the unit cells with respect to the incident electric field. These findings are verified through fabrication and measurement of the unit cells in a finite parallel plate waveguide test fixture designed for that purpose.

Chapter 4 presents a ringed rectangular patch antenna. This device incorporates concentric rings into the geometry of a traditional rectangular patch antenna to allow support of multiple similar but differently-sized current patterns within the same structure. This led to multiple frequencies of resonance at which similar radiation patterns were produced. Various geometric modifications of this antenna were used to demonstrate adaptability of the number of resonances and their frequencies.

Chapter 5 presents a modified horn antenna that utilizes a rectangular-to-square transition section and metamaterial loading to achieve circularly polarized radiation. The handedness of the radiated field is shown to be tunable through repositioning of the loading unit cells. Buildability considerations are also discussed, and simulation results demonstrating the effects of the proposed dielectric supports for metamaterial fabrication and positioning are presented.

Finally, Chapter 6 will give a concluding overview of the findings presented herein.

CHAPTER 2: BACKGROUND AND LITERATURE REVIEW

2.1 Basic Electromagnetic Theory

Electric fields can be created by two things: the presence of an electric charge, or a time-variant magnetic field. Magnetic fields are created by the presence of moving electric charge, or by time-variant electric fields. Quantitatively, the relationship between magnetic fields, electric fields, and electric charge, is described by the following four equations:

$$\nabla \times \vec{\mathcal{E}} = -\frac{\partial \vec{\mathcal{B}}}{\partial t} \tag{1}$$

$$\nabla \times \vec{\mathcal{H}} = \frac{\partial \vec{\mathcal{D}}}{\partial t} + \vec{\mathcal{J}} \tag{2}$$

$$\nabla \cdot \vec{\mathcal{D}} = \rho \tag{3}$$

$$\nabla \cdot \vec{\mathcal{B}} = 0 \tag{4}$$

where $\vec{\mathcal{E}}$ is the electric field in Volts per meter, $\vec{\mathcal{H}}$ is the magnetic field in Amperes per meter, $\vec{\mathcal{D}}$ is the electric flux density in Coulombs per meter squared, $\vec{\mathcal{B}}$ is the magnetic flux density in Webers per meter squared, $\vec{\mathcal{J}}$ is the electric current density in Amperes per square meter, and ρ is the electric charge density in Coulombs per cubic meter. In free space, the constitutive relations between $\vec{\mathcal{E}}$ and $\vec{\mathcal{D}}$ and between $\vec{\mathcal{H}}$ and $\vec{\mathcal{B}}$ are given by:

$$\vec{\mathcal{B}} = \mu_0 \vec{\mathcal{H}} \tag{5}$$

$$\vec{\mathcal{D}} = \epsilon_0 \vec{\mathcal{E}} \tag{6}$$

where μ_0 is the magnetic permeability of free space, and ϵ_0 is the electric susceptibility of free space. The continuity equation gives the relationship between charge density ρ and current density $\vec{J}$, as follows:

$$\nabla \cdot \vec{\mathcal{J}} = -\frac{\partial \rho}{\partial t} \tag{7}$$

[2].

Looking at the equations above, let us consider two special cases.

Case I: If there exists an infinite line of constant current $\vec{\mathcal{J}}$, this constant current will give rise to a constant component of the magnetic field $\vec{\mathcal{H}}$ via Eq. 2, which corresponds to a constant $\vec{\mathcal{B}}$ (Eq. 5). This leads to $\frac{\partial \vec{\mathcal{B}}}{\partial t} = 0$ on the right hand side of Eq. 1. Therefore the total electric field is directly proportional to ρ (Eq. 3), which is constant (Eq. 7). This electric field feeds back into Eq. 2 as $\frac{\partial \vec{\mathcal{D}}}{\partial t} = 0$, so that the total magnetic field also is constant and directly proportional to $\vec{\mathcal{J}}$.

Case II: If there exists an infinite line of current $\vec{\mathcal{J}}$ that varies according to a function $f(t)$ that is a non-trivial solution to the differential equation $\frac{d^2 f(t)}{dt^2} + k^2 f(t) = 0$, where k is some constant, this current will give rise to an $f(t)$-dependent $\vec{\mathcal{H}}$ via Eq. 2, which corresponds to a $\frac{df(t)}{dt}$-dependent $\vec{\mathcal{E}}$, according to Eq. 1, which in turn will give rise to a scaled $f(t)$ in the first term of Eq. 2, which feeds back into Eq. 1 and so on. This feedback loop between Eq. 1 and Eq. 2 gives rise to the electromagnetic wave.

An electromagnetic wave is a self-propagating packet of oscillating electric and

magnetic fields. They can be generated through oscillation of current on a conductor, as discussed above, and they can also generate current via incidence onto a conductor, through the same process performed in reverse. Antenna engineering is the field of engineering concerned with such generation and reception of electromagnetic waves. Antennas are conductive elements used to transition energy from guided electric currents to electromagnetic fields in free space and vice versa [3, 4].

The direction of propagation and the polarization of a created electromagnetic wave can be controlled via antenna design. The energy transmitted by an antenna is typically fed to that antenna by a tightly controlled physical structure, such as a coaxial cable or microstrip transmission line. Similarly, the energy received by an antenna is typically fed from that antenna into a tightly controlled physical transmission line structure. Antennas generally have frequency-variant input impedance, and function at the highest efficiency when operated within the frequency range where the geometry and dimensions of the antenna best work to match the impedance of the feed to the impedance of free space. Often this matching is closely tied to some resonance of the antenna structure, since the impedance of free space is a purely real quantity.

When an electromagnetic wave is traveling in free space, far from any sources, it always travels as a TEM (transverse electromagnetic) wave, meaning that the electric and magnetic fields are perpendicular to one another, and to the direction of propagation. Such a wave also travels at a fixed velocity $c = 1/\sqrt{\mu_0 \epsilon_0}$, has a fixed wavelength $\lambda_0 = \frac{c}{f}$ where f is the frequency of oscillation, and has a fixed ratio of the amplitude of the electric field to the amplitude of the magnetic field, given by the

intrinsic impedance of free space $\eta_0 = \sqrt{\frac{\mu_0}{\epsilon_0}}$.

When an electromagnetic wave travels in a homogeneous material, it interacts with that material in a way that is dictated by the material's atomic makeup. The atoms in the material can acquire both electric and magnetic polarization through the response of their electrons to the fields of the incident wave. If the atoms are much smaller than the wavelength of the traveling wave, the total effect of the polarizations of all the individual atoms can be modeled with bulk "material parameters". For instance, the effect of the magnetic polarization response of the material can be modeled as:

$$\vec{\mathcal{B}}(t) = \mu_0(1 + \chi_m) * \vec{\mathcal{H}}(t) \tag{8}$$

(compare to Eq. 5) where χ_m is called the "magnetic susceptibility" of the material. The term $(1 + \chi_m)$ is called the "relative magnetic permeability" of the material, and is given the symbol μ_r. Also note the use of '$*$', denoting convolution, which is necessary because of the general-case frequency-dependence of χ_m. Similarly, the effect of the electric polarization response is modeled as:

$$\vec{\mathcal{D}}(t) = \epsilon_0(1 + \chi_e) * \vec{\mathcal{E}}(t) \tag{9}$$

(compare to Eq. 6) where χ_e is called the "electric susceptibility" of the material. The term $(1+\chi_e)$ is called the "relative electric permittivity", and is given the symbol ϵ_r [2, 5].

The important effect these material parameters have on the foregoing equations begins with the constitutive relations, formerly given in Eqns. 5 and 6, and impacts every other equation by scaling μ_0 and ϵ_0 by μ_r and ϵ_r, respectively. Thus, the material

parameters can be used to change the group and phase velocities, wavelength, intrinsic impedance, and even direction of a propagating wave. They therefore comprise an important design tool for electromagnetics engineering.

It is important to note that the term 'homogeneous material' necessarily has a frequency dependence when discussing actual physical materials. At some frequency, even atoms become large relative to a wavelength, and the bulk material parameter approximations break down. Conversely, the lower the frequency of the incident wave, the larger the unit cells are allowed to be without violating the homogeneity approximation. The rule of thumb for judging conformity to the homogeneity model (and therefore the usefulness of bulk material parameters) is that the unit cell size should be smaller than one tenth of a wavelength. This means that non-atomic periodic structures can be used to produce effective bulk material parameters, provided the frequency of operation is sufficiently low relative to the lattice constant of the structure. As an example, for waves oscillating at 1 GHz, the unit cell size can be around a cubic inch while remaining sufficiently electrically small for the electromagnetic response of an array of such unit cells to be modeled by bulk material parameters. Such "metamaterials" can theoretically be engineered to have any desired combination of effective permeability and permittivity properties, even those not found in the normal range of atomic material permutations, such as simultaneously negative permeability and permittivity. This extra degree of control has been shown to have several interesting implications [6, 7], which will be discussed in further detail in Section 2.4 of this document.

From a bulk material perspective, then, an electromagnetic metamaterial is a pe-

riodic array of unit cells that together are assumed to approximate a homogeneous material over certain frequencies. Their interaction with electromagnetic waves can then be modeled using bulk material parameters. From an 'atomic' perspective, an individual metamaterial unit cell is a structure that, like a true atom, receives energy from an electromagnetic wave and releases that energy again as an electromagnetic wave. The effect of the interaction is dictated by the currents that set up on the structure in response to the incident wave, in a manner analogous to the response of electrons in a true atomic material.

In both antennas and metamaterials, the desired response is often a resonance-induced phenomenon, occurring over a narrow band of frequencies [8–11]. This resonance is a product of the geometry of the structure in question, and the formation of current patterns on its surface. Wider bandwidth responses have been achieved

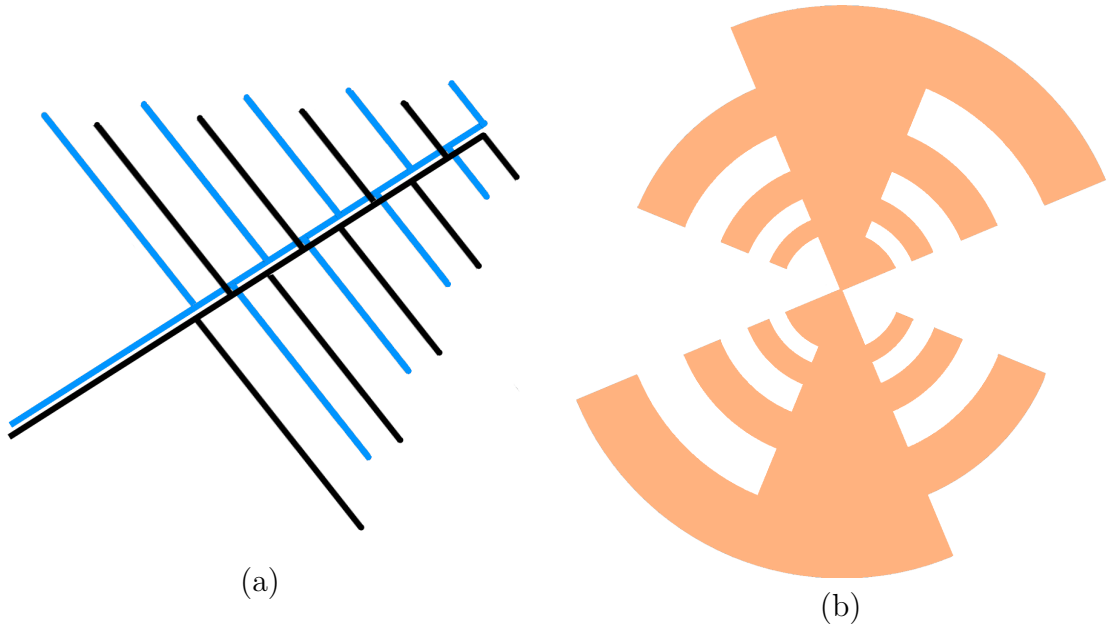

(a) (b)

Figure 1: (a) The general form of a dipole array antenna with nine dipole element pairs. (b) The general form of a log-periodic antenna with seven different arm lengths.

in antennas using log-periodic structures, where one feature of the antenna occurs in the geometry repeatedly at various scales [12]. This allows similar current patterns to repeat at multiple frequencies by utilizing different portions of the structure. For instance, a dipole array antenna like that shown in Fig. 1(a) consists of several dipoles of different lengths, connected along the feed gaps [13]. Similarly, the log-periodic antenna shown in Fig. 1(b) is formed of a bowtie antenna with concentric circular arc extensions of various lengths. In each case, the largest pair of elements will be active at the lowest frequency of operation, then a slightly smaller pair will become active as the frequency increases, and so forth until at the highest frequency of operation the currents will be concentrated in the smallest dipole element pair. The effectiveness of this technique at inducing broadband and/or multiband responses in resonant electromagnetic structures such as antennas and metamaterials has led to interest in the use of fractals in electromagnetics engineering.

2.2 Fractal Geometries

Fractal geometry was first formally developed by Benoit Mandelbrot, who had noted the inadequacy of traditional Euclidean geometry for addressing the order of complexity found in nature [14]. One of the earliest examples he used to illustrate this inadequacy was the question of the length of Britain's coastline, originally posed by Lewis Richardson in [15]. Mandelbrot showed that the measured length of the coastline would depend on the resolution of the polygon used to approximate it [16]. He pointed out that this characteristic was shared by many naturally occurring shapes, such as those of clouds or mountains. He proceeded to develop an entire class of struc-

tures that shared this characteristic, to which he assigned the appellation “fractal”, derived from the Latin for “to break”. He also retroactively applied this term to several existing geometries, including the Koch and Hausdorff curves, and the Sierpinski gasket [14].

Fractals are geometric designs that are characterized by some feature that is infinitely repeated at ever-reduced scales. Some of these designs are generated through spatial mapping of sets of complex numbers that fit a given criteria, such as the Mandelbrot set shown in Fig. 2.

Other fractal geometries are formed through an iterative process in which a given simple geometric feature is transformed into some number of scaled repetitions of itself. For instance, the Koch fractal is formed from a straight horizontal line segment (the original simple feature, or “initiator”) through infinite repetition of a process whereby the single straight line is transformed into a specific arrangement of four

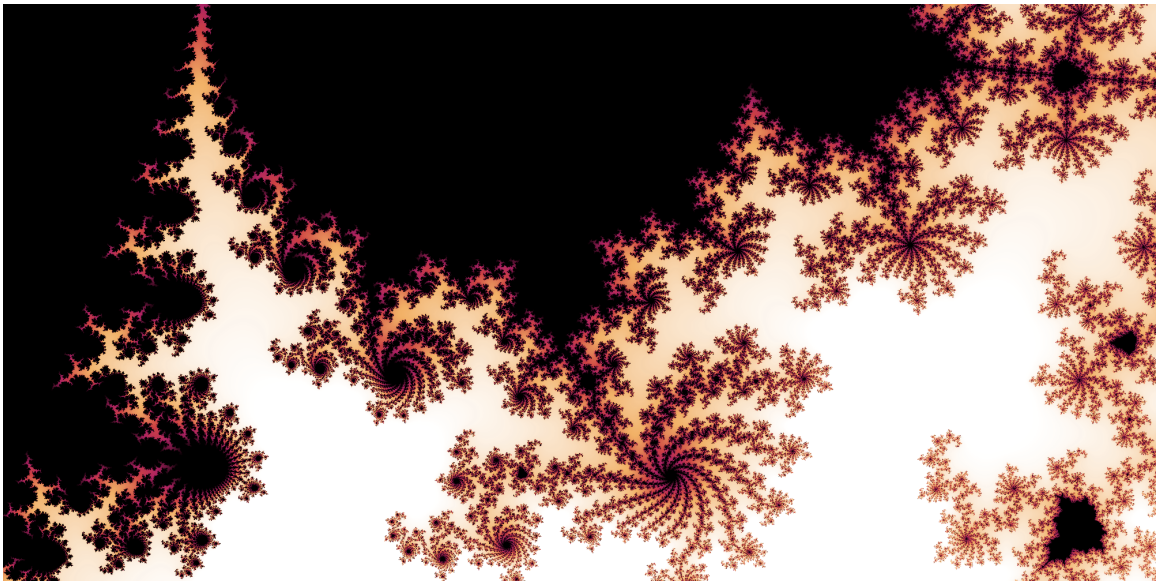

Figure 2: The Mandelbrot Fractal.

(a) (b)

Figure 3: Examples of naturally occurring fractals. (a) A head of Romanesco broccoli [17]. (b) A fern frond [18].

line segments, each of which has a length equal to one-third that of the original line segment. Fig. 4 shows the Koch fractal at the zeroth, first, second, and third iterations of the formation process.

Another example of an iteratively-constructed fractal is the fractal tree. This fractal is formed from a 'V' by replacing a portion of each branch of the 'V' with a scaled version of itself, as shown in Fig. 5. It is also possible to introduce a component of chance to the formation of such a tree, for instance by randomizing the branch lengths, or by having some probability of splitting into three or four branches rather than two, or even of not splitting at all. Further iterations of both the Koch curve and the fractal tree, as well as a three-dimensional fractal tree and other iteratively constructed fractals can be found in [3, 20].

In order for the product to be a true fractal, the formation process must continue for an infinite number of iterations. This will result in a geometry that is infinitely jagged, or, in mathematical terms, non-differentiable at every point. A true mathematical fractal curve will also have an infinite length and/or perimeter, though it is

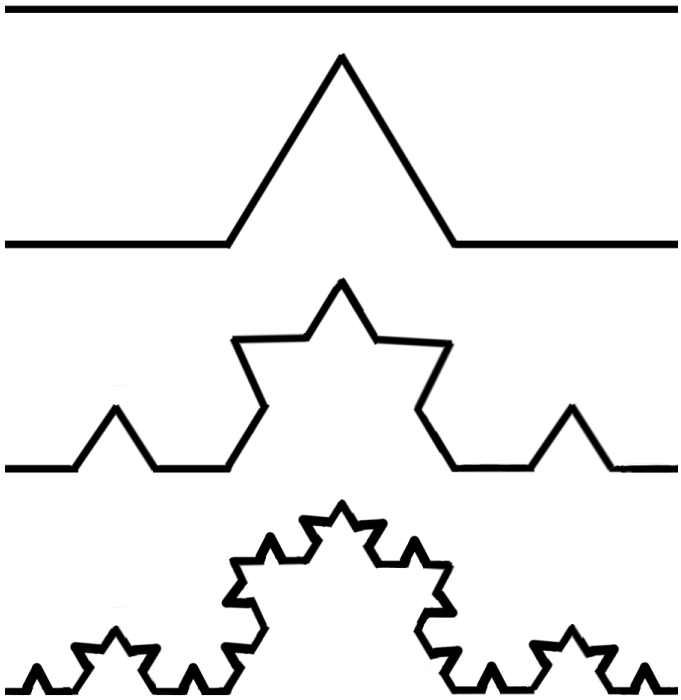

Figure 4: The first four iterations of the Koch fractal, first presented by Helge von Koch in 1904, and translated into English in [19].

contained in a finite space. Practically, however, only a certain amount of complexity is physically realizable. In actual practice, therefore, the generation process is truncated after some finite number of iterations, resulting in a fractal approximation, or "prefractal" [20]. Since this is the only realizable form of a fractal geometry, we will henceforth use the term "fractal" more loosely, to include geometries composed of finite iterations.

2.3 Fractal Antennas

Fractal geometries lend themselves quite naturally to design of multiband or wideband antennas, because of the scaled repetition of similar shapes, as in the log periodic antennas discussed earlier. They are also uniquely suitable for electrically-small an-

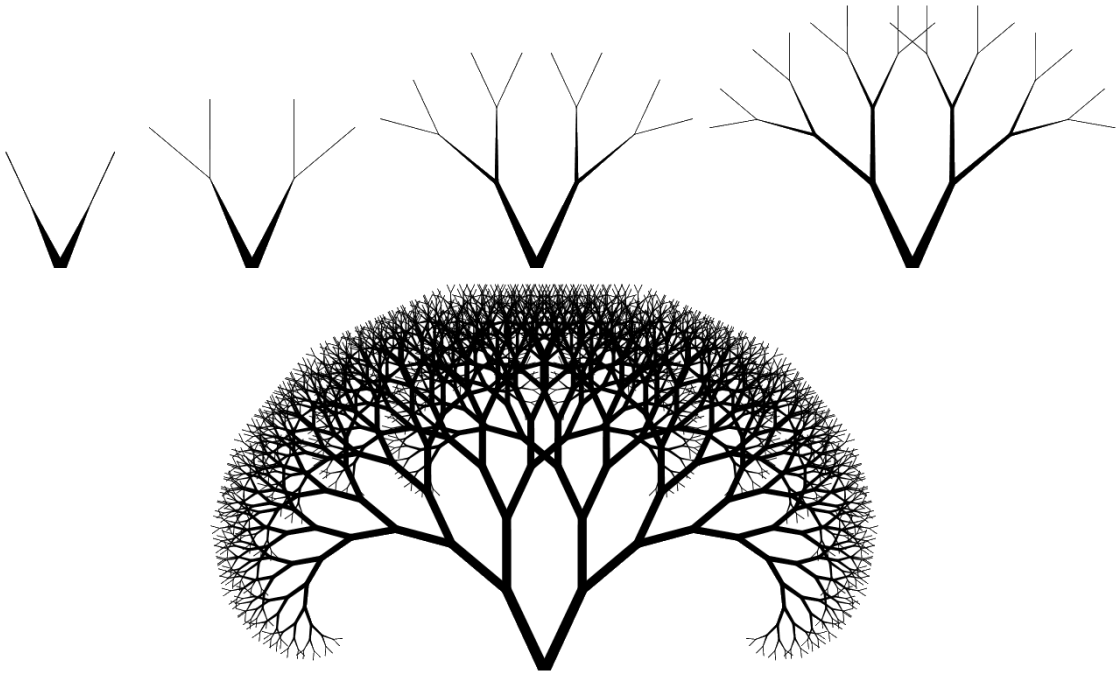

Figure 5: The first four and the tenth iterations of a fractal tree.

tenna design, because of the efficiency of spacial utilization resulting from the high complexity [3]. The left side of Fig. 6 shows a fractal monopole that was shown in [21] to exhibit multiband performance. This fractal consists of a circular ground,

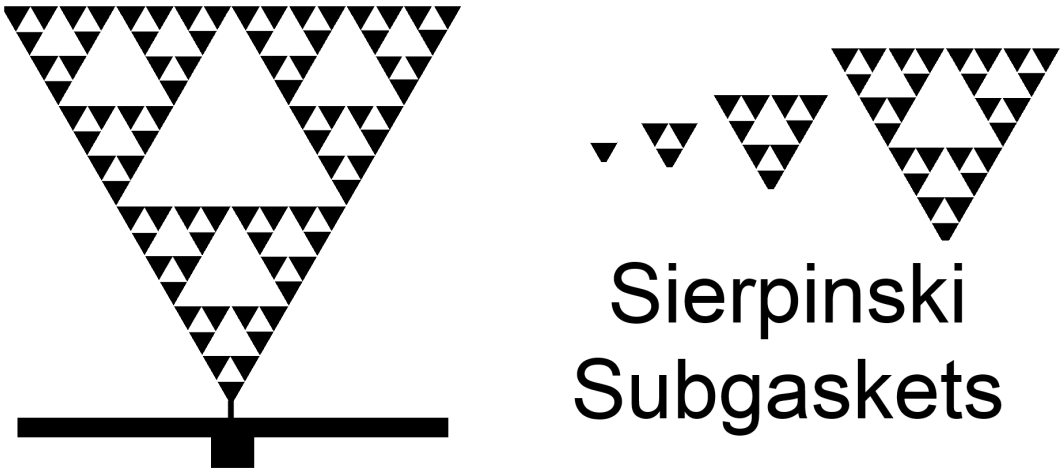

Figure 6: The Sierpinski gasket monopole antenna presented in [21, 22] (left), and its four subgaskets (right).

like that of a disk-cone antenna, and a two-dimensional radiating element fashioned after a Sierpinski gasket fractal. This fractal has four iterations beyond the initiator, which in this case is the outermost triangle. It was shown in [22] that each band of operation for this antenna corresponded to activity in a particular subgasket of the fractal. The resonant frequencies approximately matched those of bowtie antennas sized to correspond to the Sierpinski gasket antenna and its four subgaskets, with some shifting to lower frequencies because of added capacitance. It was also shown in [23] that the frequencies of operation could be tuned by deforming the inner triangles to increase the size of the smaller subgaskets, as shown in Fig. 7. Further manipulation of this antenna design is explored in [24–27].

Figure 8 (a) shows another two-dimensional monopole antenna, originally presented in [28]. This antenna is based on a variation of the tree fractal, and has a two-dimensional ground, with a curve used to help match the antenna to a 50 Ω feed. This antenna was shown to be extremely wideband, with each increase in number

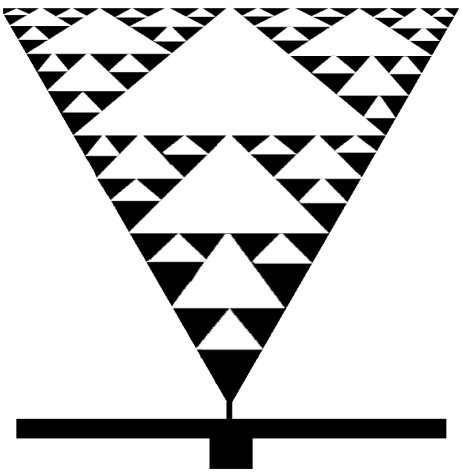

Figure 7: A "perturbed" Sierpinski gasket monopole antenna like those presented in [23].

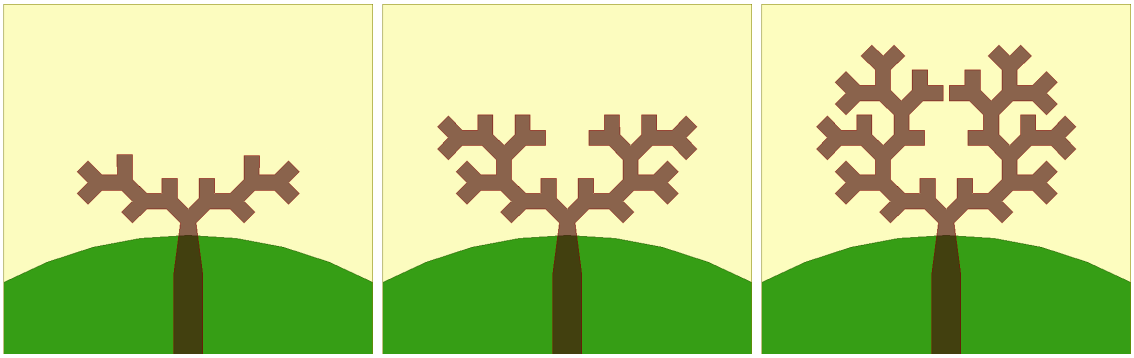

(a) (b) (c)

Figure 8: A family of two-dimensional fractal tree monopole antennas like those presented in [28]. (a) One iteration (b) Two iterations (c) Three iterations

of iterations creating an additional resonance in the response. The three-iteration model, which was 22 mm high, was shown to operate from 2.1 GHz to 11.52 GHz, a bandwidth of 138%.

Figure 9 shows a third two-dimensional fractal tree antenna, this one based on the Pythagorean tree fractal. This antenna was 25 mm high, and the five-iteration model was shown to operate from 2.64 GHz to 11.14 GHz, which is a bandwidth of 123%. Other two-dimensional fractal monopole and dipole antennas are presented in [30–41], among others.

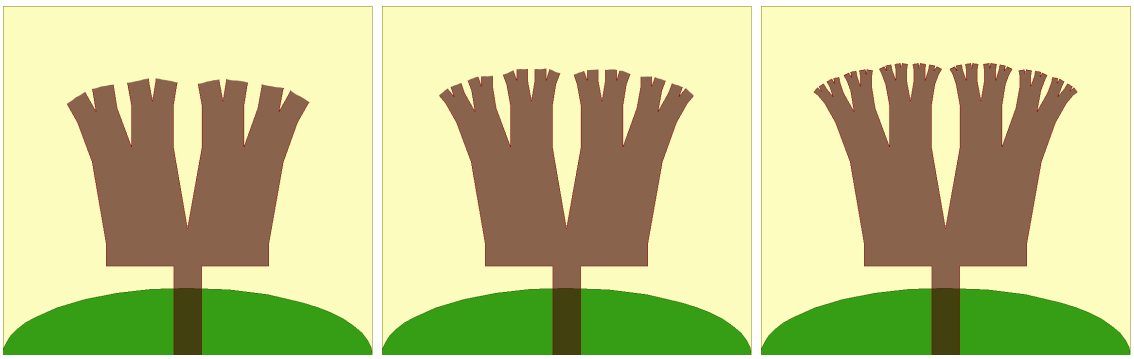

(a) (b) (c)

Figure 9: A family of two-dimensional Pythagorean tree monopole antennas like those presented in [29]. (a) Three iterations (b) Four iterations (c) Five iterations

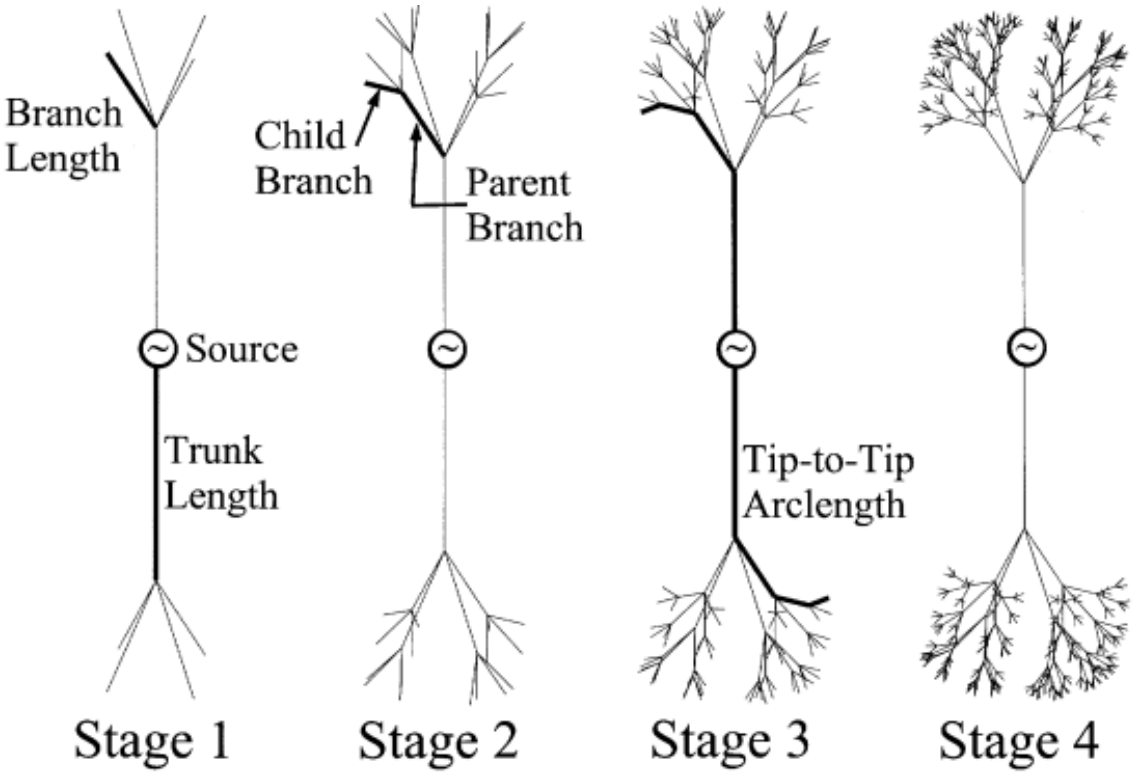

Figure 10: Several iterations of the three-dimensional fractal tree dipole antenna from [42].

The innate drawback to two-dimensional fractal tree antennas is that, unlike traditional monopole or dipole antennas, they are asymmetric in the H-plane, which can result in aberrant radiation patterns and polarization. Taking this into consideration, the natural progression from a two-dimensional fractal tree is to a three-dimensional fractal tree. These were theoretically explored in [42], where the fractal trees were used in a dipole configuration, as shown in Fig. 10. Several variations were simulated, with various numbers of branches, various numbers of iterations, and various angles of branch elevation. Lumpled-element reactive loading of the fractal branches was also explored. This paper showed that these fractal tree antennas were capable of operation at much lower frequencies than a traditional dipole, and also showed how each

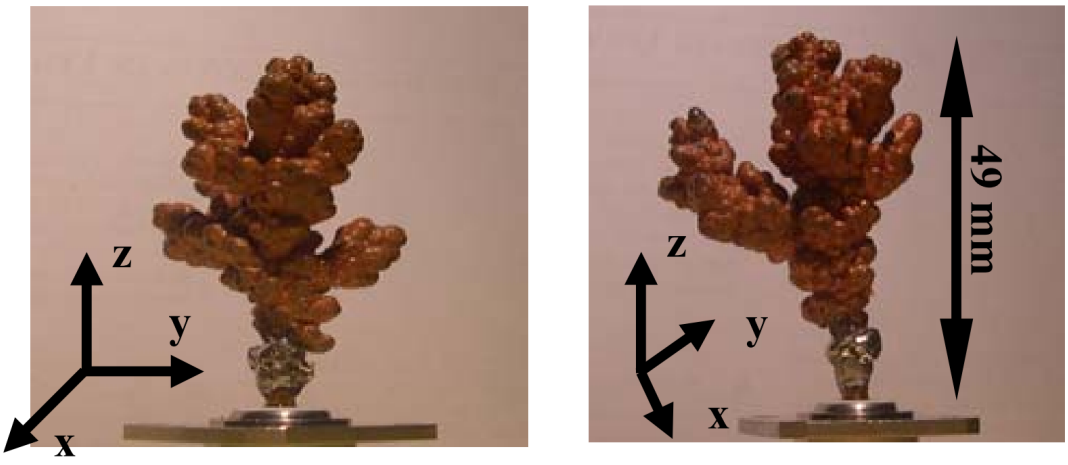

(a) (b)

Figure 11: An electrochemically deposited fractal tree antenna, taken from [46].

of the aforementioned variables affected the response. It is important to note that this paper only presented simulation results, however, because of the complexity of fabrication. Three-dimensional fractal antennas are also investigated via simulation in [43–45].

In [46], a fabricated 3D fractal tree antenna is presented. The antenna was fabricated through electrochemical deposition in a copper electrolyte bath, which resulted in a copper fractal tree which was then used as the radiating element of a monopole. The resulting antenna, shown in Fig. 11, was 49 mm long, and was shown to have four bands of operation between 1 and 20 GHz. However, the nature of the generation process was innately random, and therefore unrepeatable, as well as being impossible to design or simulate prior to fabrication.

Chapter 5 of [47] was dedicated to developing a deterministic three-dimensional fractal tree monopole antenna that could be fabricated using 3D printing. The original approach used a three-dimensional expansion of the Pythagorean tree fractal antenna

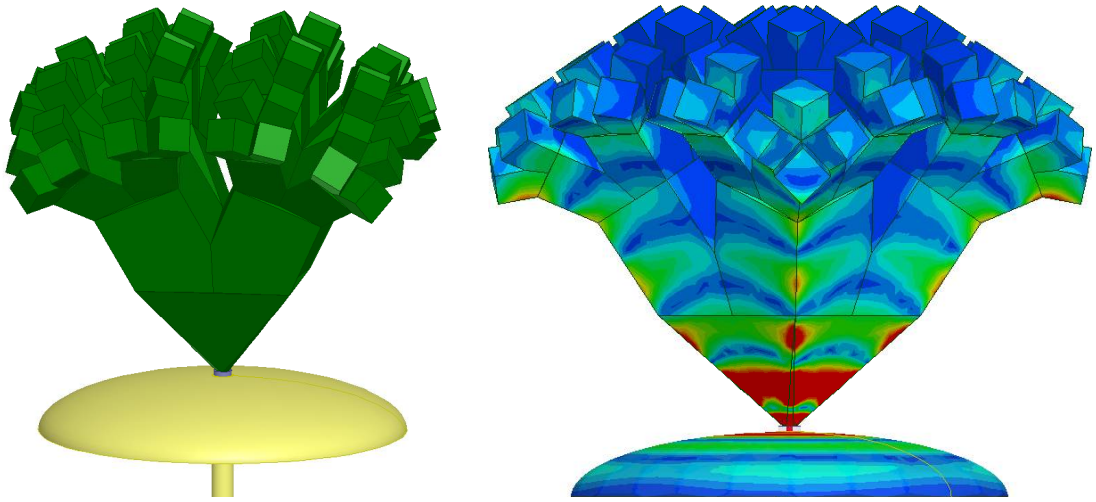

(a) (b)

Figure 12: (a) A three-dimensional version of the Pythagorean tree fractal monopole antenna. (b) Surface current density on the antenna at 15 GHz

shown in Fig. 9. This resulted in the antenna shown in Fig. 12 (a). This antenna was shown to have extremely wideband performance - from 1.24 GHz beyond 25 GHz. However, the cross-polarization was very high, which was theorized to be largely due to the high current density on the sharp edges of the fractal tree, which can be seen in Fig. 12 (b).

In an attempt to improve the polarization characteristics, a cone-based fractal tree antenna was developed. This antenna, originally published in [48], is shown in Fig. 13. Several variations of this antenna were investigated, including versions with three, four, five, and six branches per iteration, and versions with one, two, and three iterations. The best case was found to be the version shown in Fig. 13, which was shown in both measurement and simulation to have an extremely wide band of operation, from 1.22 GHz to 24.1 GHz. This antenna also had much better polarization characteristics than the cubic fractal tree antenna.

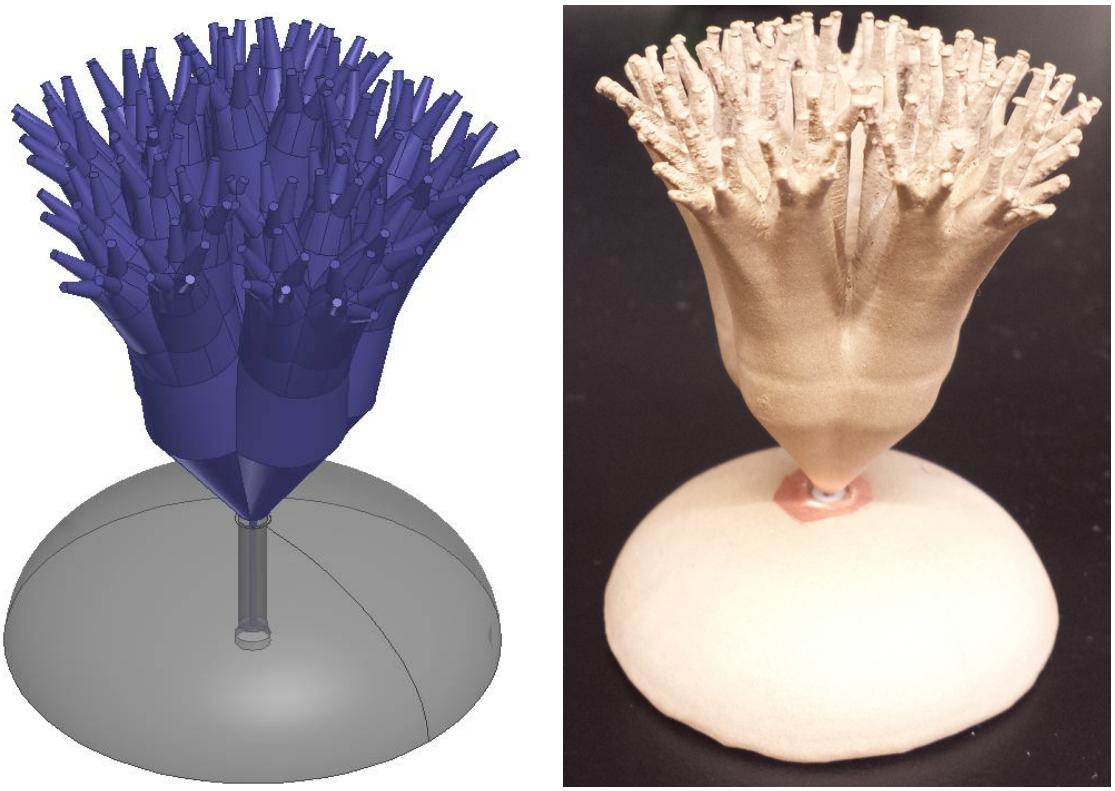

(a) (b)

Figure 13: A three-dimensional fractal tree monopole antenna with a conical basis (a) as a model in HFSS. (b) 3D printed and spray-painted with conductive paint.

Fractals can similarly be used to miniaturize loop antennas. In [49], a fractal loop antenna based on a Minkowski island like that shown in Fig. 14 is simulated at its zeroth, first, second, and third iterations. The return loss for each of these cases is presented, and it is demonstrated that each increase in number of iterations corresponds to an increase in the number of resonant frequencies, and a decrease in the lowest frequency of resonance.

A similar loop antenna using a Koch fractal is presented in [50], and is shown to have increasing bandwidth and decreasing frequency of operation with each increase in number of iterations. Additional fractal loop antennas are presented in [51–54], among others.

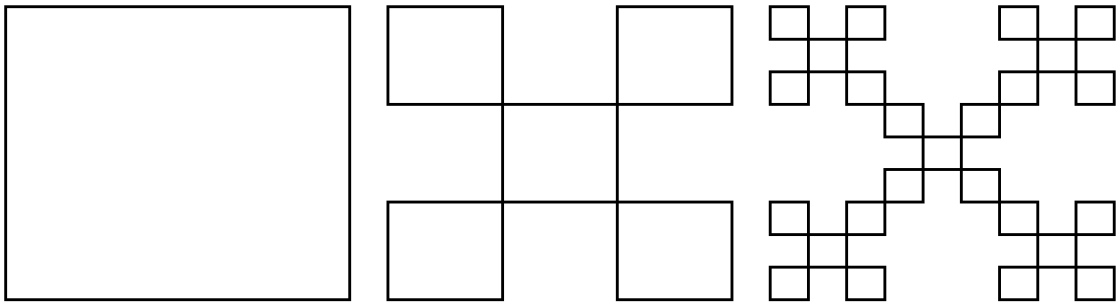

Figure 14: The zeroth, first, and second iterations of the Minkowski fractal.

Fractals have also been utilized in design of patch antennas. In [55] and [56], a bowtie patch is modified through addition of several "perturbation slots" following the pattern of a Sierpinski gasket, as shown in Fig. 15, from [55]). The effect of this modification is shown to be a frequency shift in the resonance of the patch, from approximately 1.95 GHz unperturbed to 1.13 GHz after addition of the Sierpinski slots. A high directivity of around 10 dB is maintained, though the bandwidth is reduced by about half.

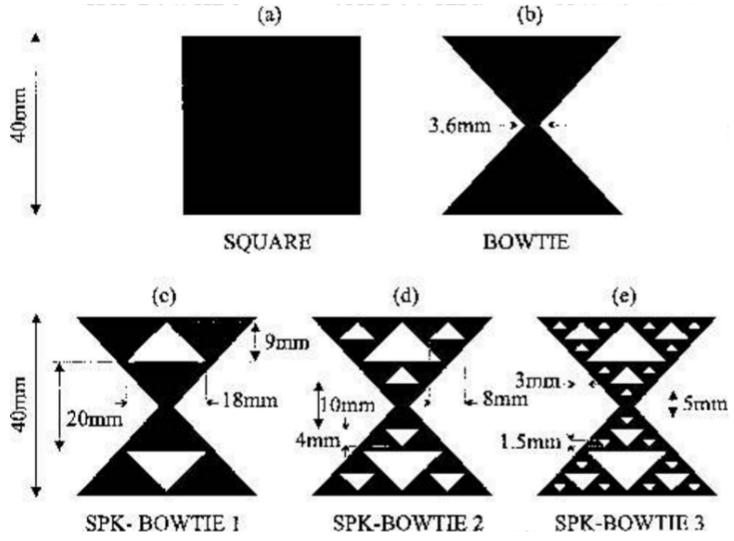

Figure 15: A bowtie patch antenna, modified according to a Sierpinski gasket, from [55].

Figure 16: A "crown square fractal" patch antenna from [57].

In [57], the patch antenna shown in Fig. 16 is presented. In this case, the addition of the fractal geometric features is shown to introduce a second band of operation over which similar polarization characteristics are maintained. This antenna is further developed in [58], where its resonant frequency is further reduced through increasing fractal complexity.

In [59], a triangular patch antenna incorporating a Sierpinski gasket fractal pattern is presented. The three-iteration model is shown in Fig. 17. This paper presents simulated and measured return loss for the zeroth, first, second, and third iterations. It shows that, though the zeroth iteration has no frequency of efficient radiation, the first iteration has one radiating frequency, the second iteration has two radiating frequencies, and the third iteration has three radiation frequencies. No information concerning the antenna radiation pattern is presented.

A fractal patch antenna based on a Minkowski fractal is presented in [60]. The three-iteration version of this antenna is shown in Fig. 18. Again, the increasing number of fractal iterations was shown to correspondingly increase the number of resonant frequencies. However, the radiation patterns presented for the four radiation frequencies of the three-iteration case bear no similarity to one another, or to that of

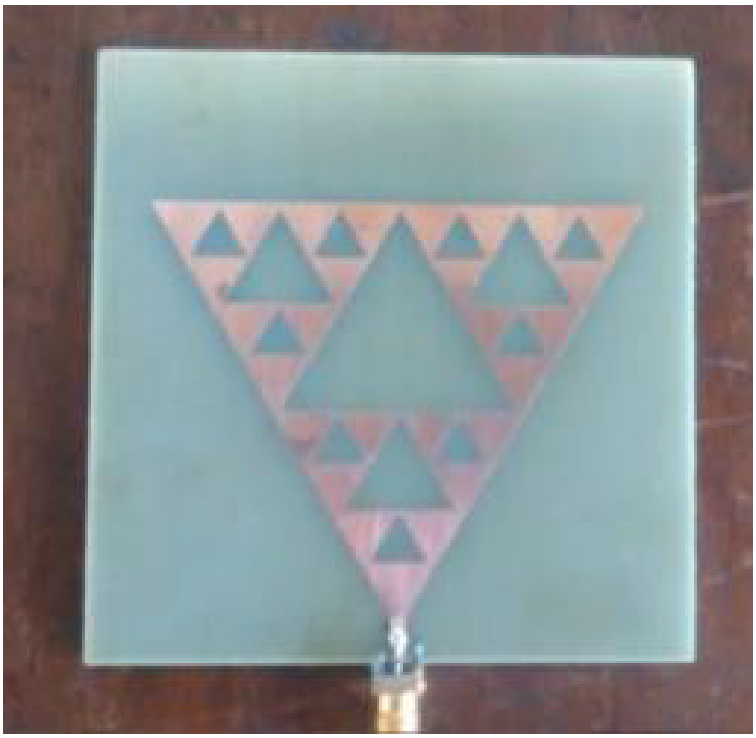

Figure 17: A multiband fractal patch antenna based on a Sierpinski gasket from [59].

a traditional rectangular patch antenna.

Other fractal patch antennas are presented in [61, 62], among others. Fractal geometries also have application in the design of antenna arrays, as discussed in [63–65].

Up to this point, the discussion of electrically small antennas has focused on a single miniaturization methodology - that of exotic radiation element geometries. Another method is to load the antenna with electromagnetic metamaterial unit cells [66–70]. Therefore, the following section will discuss the history and development of electromagnetic metamaterials, and discuss how fractal geometries can be used to improve their performance.

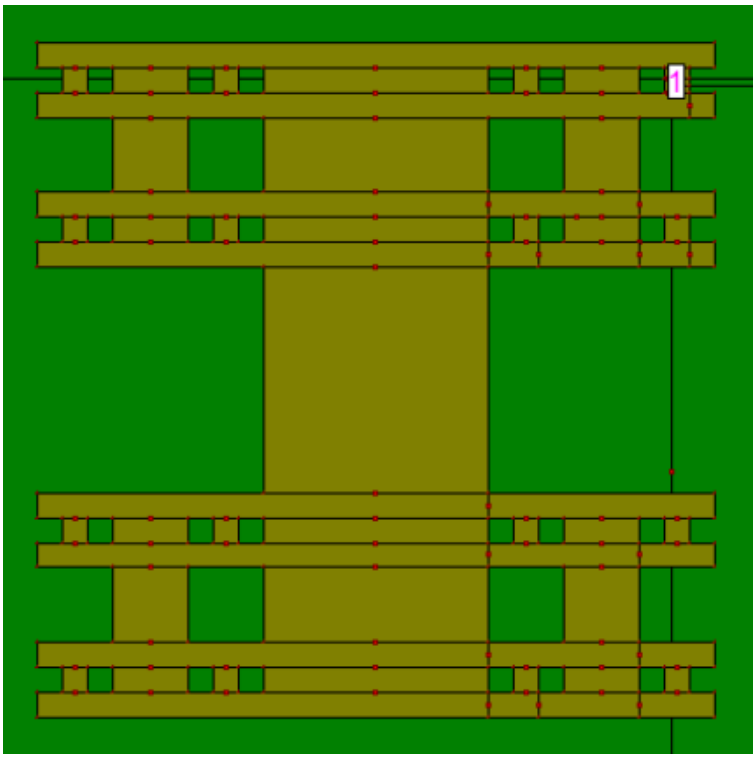

Figure 18: A multiband fractal patch antenna based on a Minkowski curve, from [60].

2.4 Electromagnetic Metamaterials

As discussed in Section 2.1, electromagnetic field interaction with materials is modeled using bulk material parameters μ_r and ϵ_r. If we look at the relatively simple case where both permeability and permittivity are required to be purely real, the possible values of permeability and permittivity fall into four regions, as depicted in Fig. 19.

Quadrants I and III of Fig. 19 represent materials in which an electromagnetic wave may propagate, and quadrants II and IV represent materials in which an electromagnetic wave may not propagate. To demonstrate this point, consider the case of a plane wave traveling in a lossless dielectric, with electric field given by $\vec{E} = E_\circ e^{-j\beta r}\vec{a_E}$, where $E_\circ$ is the amplitude of the electric field, r is the spatial dimension in which the

wave is propagating, $\vec{a_E}$ is a unit vector perpendicular to the direction of propagation, pointing in the direction of electric field oscillation, and β is the propagation constant, given by $\beta = \omega\sqrt{\mu_r\epsilon_r}/c$, where ω is the radial frequency of the wave oscillation and c is the speed of light in a vacuum, approximately equal to 3×10^8 m/s. Clearly, if both μ_r and ϵ_r have the same sign, as in quadrants I and III of Fig. 19, β is a real number, and $\vec{E}$ represents a propagating wave. However, if either μ_r or ϵ_r is negative,

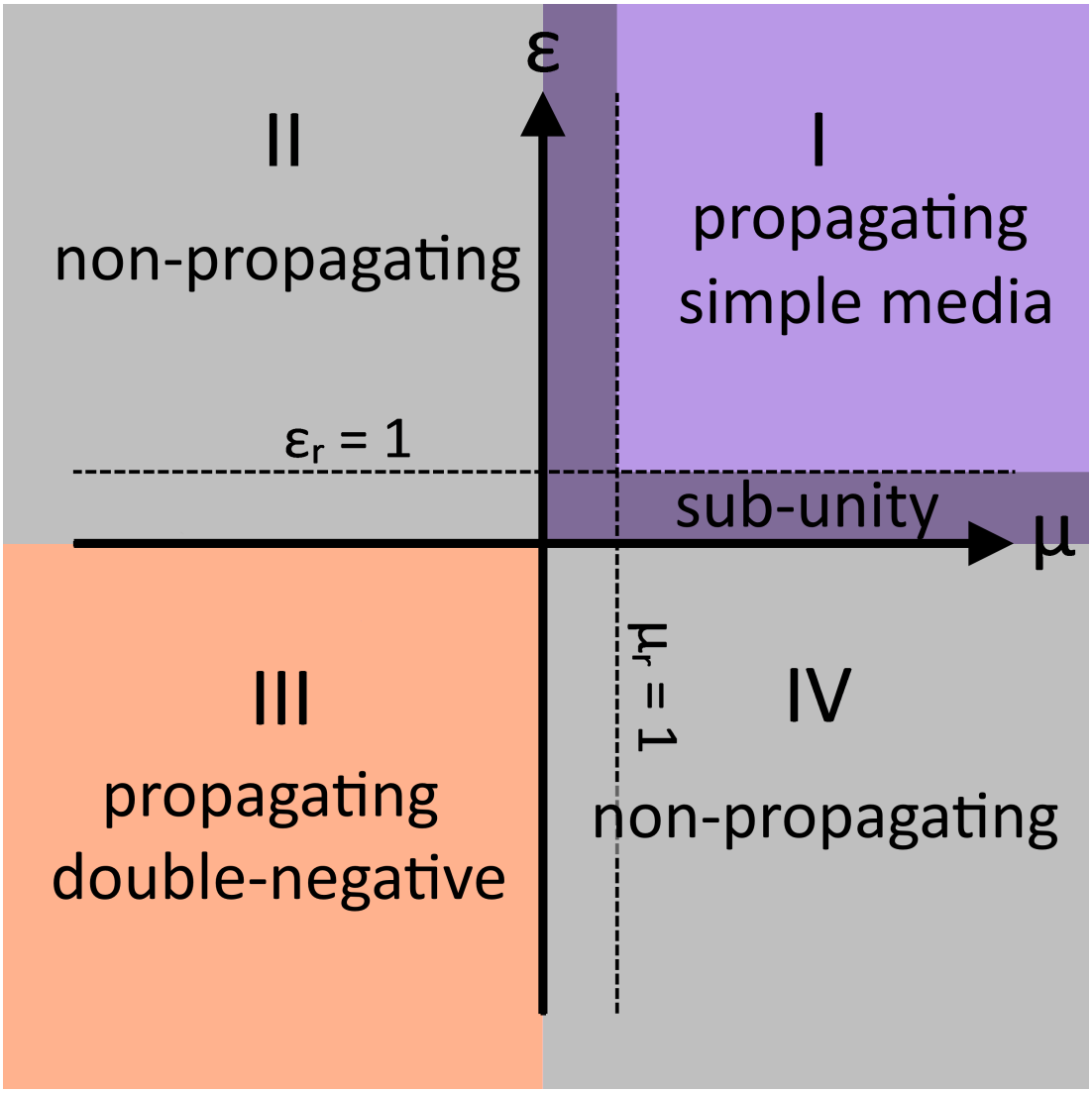

Figure 19: The four possible sign combinations of μ_r and ϵ_r.

while the other is positive, as in quadrants II and IV of Fig. 19, β is purely imaginary, and the wave represented by $\vec{E}$ becomes evanescent. No known naturally occurring materials fall in quadrant III [71].

In 1964, Veselago posited that if a material could be created that had simultaneously negative permeability and permittivity, such "double-negative" materials would have several unique properties, such as a left-handed $\vec{E}$, $\vec{H}$, $\vec{k}$ triplet, negative index of refraction, and phase velocity in the opposite direction of the Poynting vector [6].

The index of refraction of a given material is defined by:

$$n = \pm\sqrt{\mu_r \epsilon_r} \tag{10}$$

where μ_r and ϵ_r are the relative permeability and permittivity of the material. Veselago showed that for a left handed medium, in which both μ_r and ϵ_r are negative (quadrant III of Fig. 19), the negative root of n must be chosen. The time-averaged pointing Poynting vector, which indicates the direction of power flow, is given by:

$$\vec{S}_{av} = \frac{1}{2} Re\{\vec{E} \times \vec{H}^*\} \tag{11}$$

where $\vec{E}$ is the electric field vector, and $\vec{H}^*$ is the complex conjugate of the magnetic field vector. The phase velocity $\vec{v}_{ph}$ of a plane wave traveling in a medium is given by:

$$\vec{v}_{ph} = \frac{c}{n} \frac{\vec{S}_{av}}{|\vec{S}_{av}|} \tag{12}$$

where c is the speed of light in a vacuum. The propagation vector $\vec{k}$ is given by:

$$\vec{k} = \frac{\omega}{|\vec{v}_{ph}|^2} \vec{v}_{ph} \tag{13}$$

where ω is the angular frequency, equal to 2π times the frequency in Hz.

It can be seen from these equations that, for a plane wave traveling in a medium, changing the sign of n will change the direction of phase velocity, but not the direction of power flow. This principle is demonstrated in Fig. 20. This figure shows the magnitude of the electric field in a parallel plate waveguide. The waveguide is divided into three sections. The left-hand and right-hand sections are filled with a vacuum, where $\epsilon_r = 1$, $\mu_r = 1$, and $n = 1$. The middle section is filled with a material where $\epsilon_r = -1$, $\mu_r = -1$, and $n = -1$. The phase of the excitation is varied from 0° (top) to 180° (bottom), in steps of 30°. The wave is excited at the left side of the plot, and it can be observed in the progression from the top plot to the bottom plot that the phase moves from left to right (positive phase velocity) in the left-hand and right-hand sections, but from right to left (negative phase velocity) in the center section. Power flow, indicated by the direction of $\vec{S}_{av}$, is consistently directed to the right.

Snell's law for refraction of light at an interface between two materials is given by:

$$\frac{\sin\theta_i}{\sin\theta_t} = \frac{n_2}{n_1} \tag{14}$$

or

$$\theta_t = \sin^{-1}\left(\frac{n_1}{n_2}\sin\theta_i\right) \tag{15}$$

where n_1 is the index of refraction in the first medium, n_2 is the index of refraction in the second medium, θ_i is the incident angle, measured between the direction of propagation in the first medium and the normal to the plane of incidence, and θ_t is the transmitted angle, measured between the direction of propagation in the second

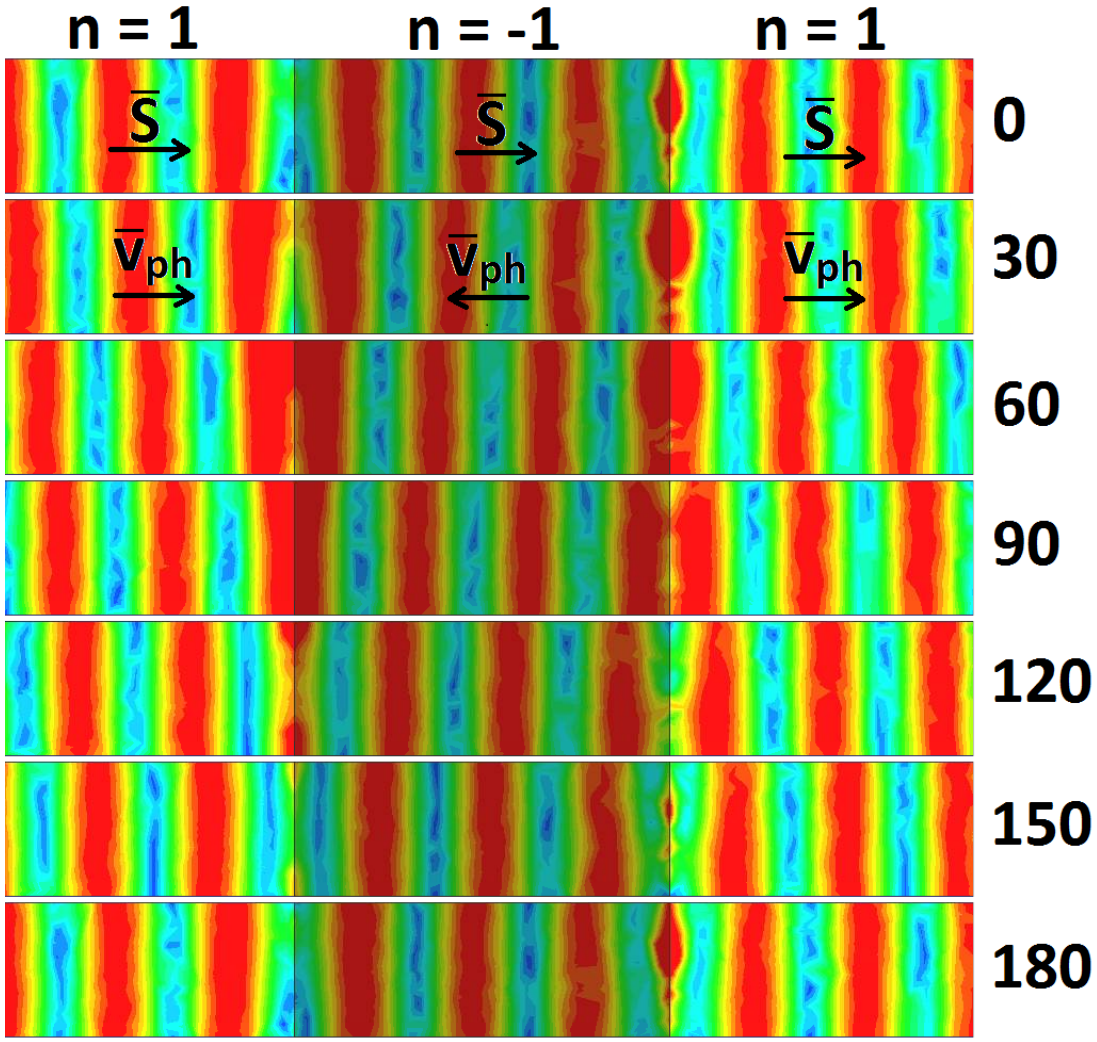

Figure 20: Effect of a chunk of $n = -1$ material on v_{ph}.

medium and the normal to the plane of incidence. The direction of propagation is given by the Poynting vector. By definition, positive θ_t is located on the opposite side of the normal from the incident wave. There is also a reflected wave, at angle $\theta_r = \theta_i$ on the opposite side of the normal from the incident wave. This is visually depicted in Fig. 21, where $\vec{S}_i$, $\vec{S}_r$, and $\vec{S}_t$ are the time-averaged Poynting vectors of the incident wave, the reflected wave, and the transmitted wave, respectively. The

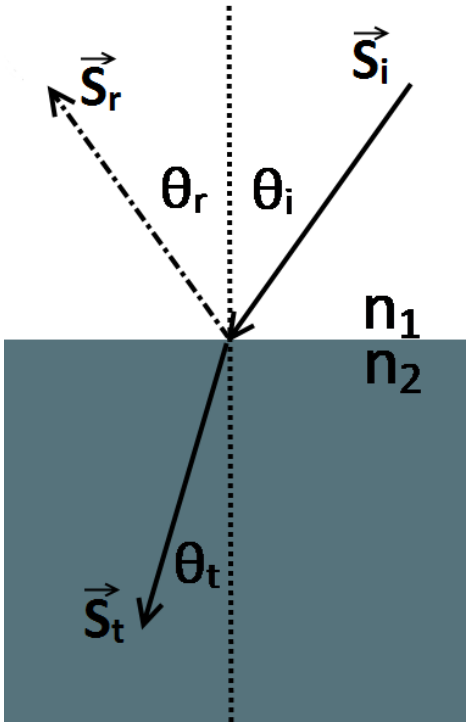

Figure 21: Snell's law diagram for transmission and reflection of a ray of light at a dielectric interface.

range of θ_i is $[0°, 90°)$, because of the way that θ_i is defined. The range of $\sin(\theta_i)$, then, is $[0, 1)$, and the range of θ_t for $n_1, n_2 > 0$ or $n_1, n_2 < 0$, is $[0°, 90°]$. In order to bend light past the normal, into the range $\theta_t = [-90°, 0°)$, transmission must be from a left-handed material ($n < 0$) into a right-handed material ($n > 0$), or vice versa.

Figure 22 demonstrates this phenomenon. Figure 22 (a) shows a plane wave propagating in a vacuum, where $\theta_i = 45°$, incident upon a $n = 1 : n = 2$ boundary. The magnitude of $\vec{E}$ is plotted as a color gradient, and the direction of $\vec{S}_{av}$ is plotted as a grid of black arrows. Based on Eq. (15), the transmitted wave should have $\theta_t = 20.7°$. Though the exact numerical analysis is lacking in the figure, it is clear that the direction of propagation in the second medium has bent toward the normal, when compared to the direction of propagation in the first medium. Figure 22

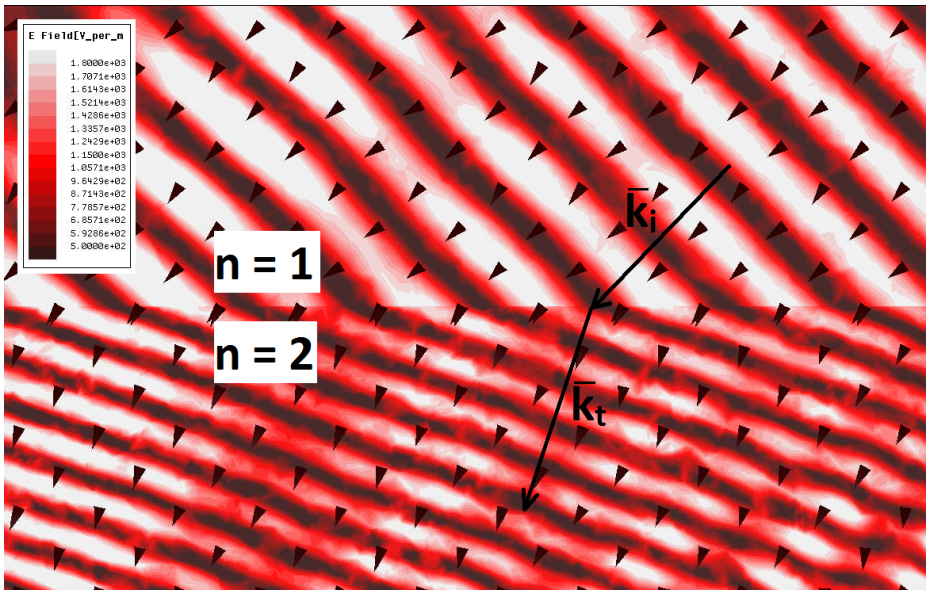

(a)

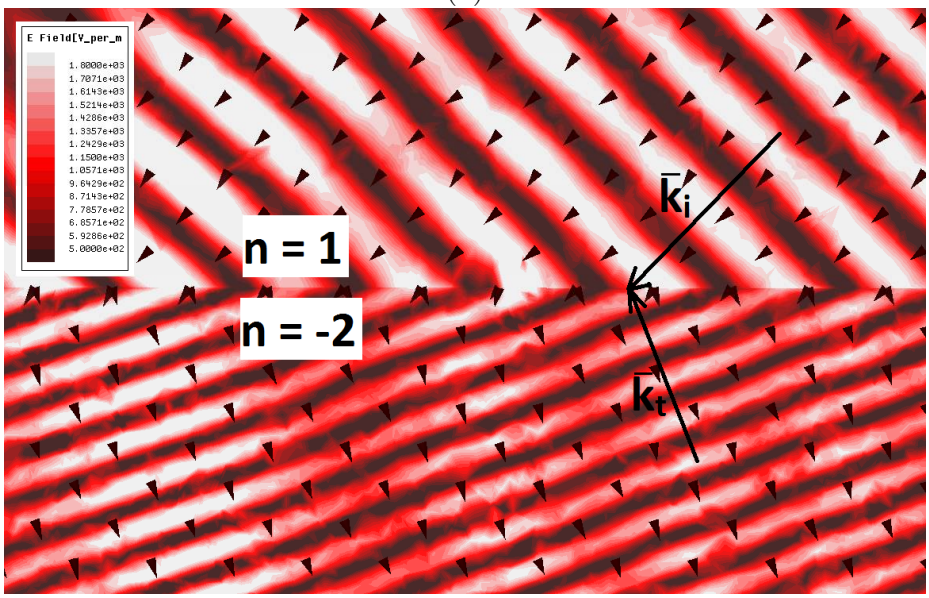

(b)

Figure 22: (a) A plane wave incident upon a $n = 1 : 2$ boundary. (b) A plane wave incident upon a $n = 1 : -2$ boundary. The time-averaged Poynting vector is given by the grid of small black arrows

(b) shows a plane wave propagating in a vacuum, where $\theta_i = 45°$, incident upon a $n = 1 : n = -2$ boundary. Again, the magnitude of $\vec{E}$ is plotted as a color gradient and the direction of $\vec{S}_{av}$ is plotted as a grid of black arrows. From (15), we expect the transmitted wave to propagate at an angle of $\theta_t = -20.7°$, at the same magnitude

as the previous figure, but on the opposite side of the normal. It is clearly shown in Fig. 22 (b) that transmission from a $n > 0$ material to a $n < 0$ material caused the direction of propagation to bend past the normal, into the $\theta_t < 0$ region. It is also noted that the $\vec{k}$ vector in the second medium points opposite to propagation,

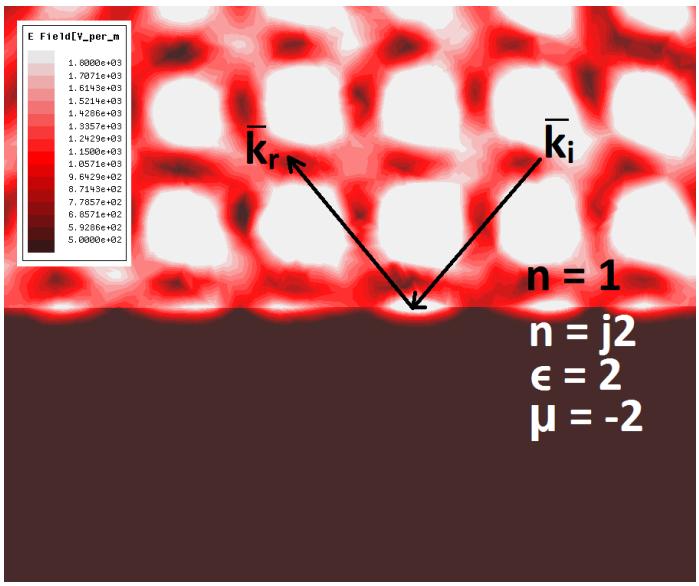

(a)

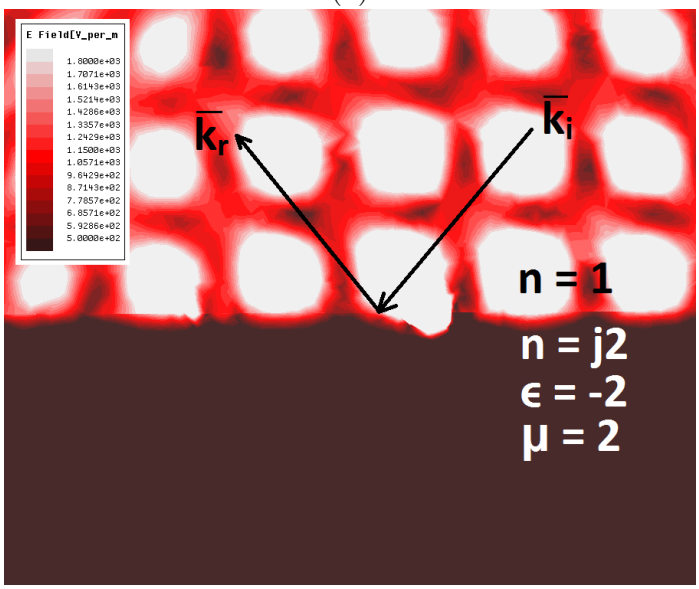

(b)

Figure 23: (a) A plane wave incident upon a $n = 1 : j2$ boundary, where $\mu_r = -2$ and $\epsilon_r = 2$ (Quadrant II). (b) A plane wave incident upon a $n = 1 : j2$ boundary, where $\mu_r = 2$ and $\epsilon_r = -2$ (Quadrant IV).

as predicted.

Figure 23 shows the behavior of a wave traveling in a vacuum incident upon a single-negative medium. Figure 23 (a) shows a wave with $\theta_i = 45°$ incident upon a medium with $\mu_r = -2$, $\epsilon_r = 2$, so that $n = j2$. Figure 23 (b) shows a wave with $\theta_i = 45°$ incident upon a medium with $\mu_r = 2$, $\epsilon_r = -2$, so that $n = -j2$. These are quadrant II and quadrant IV materials, which do not support wave propagation. As can be seen, in both cases the wave quickly decays upon incidence with the imaginary-index material, and ultimately reflects back into the first medium, creating the interference pattern shown.

Double-negative materials are shown to enable heretofore impossible manipulation of electromagnetic fields. Many practical applications for such materials have been proposed, such as the electrically small antennas mentioned earlier [67, 72], perfect flat lenses [73], electromagnetic cloaking [74, 75], and wideband artificial magnetic conductors [76], as well as more speculative applications, such as time reversal [77] and history editing [78].

Since no known double-negative materials exist in nature to allow realization of these propositions, the development of metamaterials to achieve negative permittivity and negative permeability has become a topic of extensive research. Several resonant structures have been proposed that exhibit negative parameters. One such structure is the split ring resonator (SRR), which exhibits negative permeability at frequencies slightly above resonance [8]. This structure is composed of a pair of circular metallic strips with gaps, as shown in Fig. 24 (a). In [8], an array of these structures with a lattice constant of 10 mm is shown to produce negative permeability at around

(a) (b)

Figure 24: (a) A split ring resonator. (b) A capacitively loaded strip.

13.5 GHz. It happens that at this frequency, the unit cell is not electrically small; in fact, it is approximately half a wavelength. Another is the capacitively loaded strip (CLS), which exhibits negative permittivity at frequencies slightly above resonance [9]. This structure is composed of a straight metallic strip terminated on either end with one of two capacitive parallel strips, as shown in Fig. 24 (b). A simulation of these CLS unit cells with a lattice constant of 5.33 mm was shown to begin resonating at round 8.5 GHz, where the unit cell size was approximately $\lambda_0/6$. A double-negative metamaterial was first measured in 2000, using SRRs and copper wire strips [10]. A second double-negative metamaterial composed of SRRs and resonant electric LC structures was presented in [79].

Since, as with antennas, metamaterials have behavior that is closely tied to their resonance, fractal geometries can be used to create multiband performance in metamaterials, and also help to shift the resonant frequency down without increasing the unit cell size.

Figure 25 shows a two-dimensional fractal expansion of the original CLS unit cell.

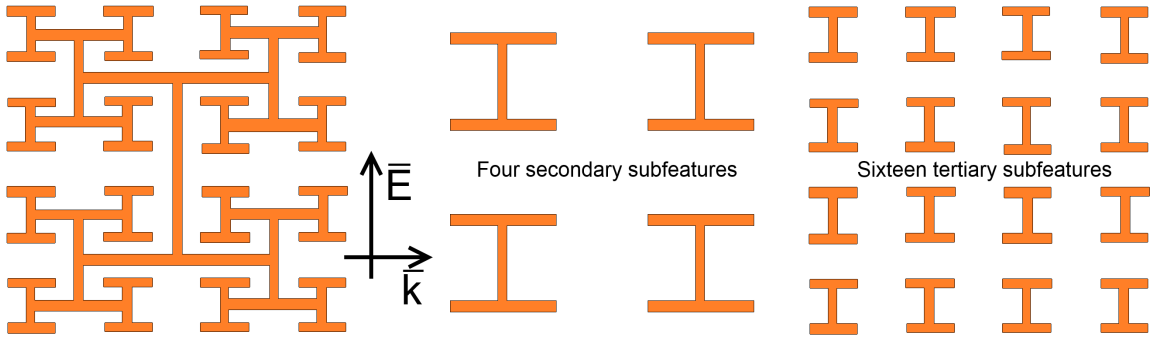

(a) (b) (c)

Figure 25: (a) A fractal negative-epsilon metamaterial with a CLS basis, with (b) its four secondary subfeatures and (c) its sixteen tertiary subfeatures, like that presented in [80, 81]

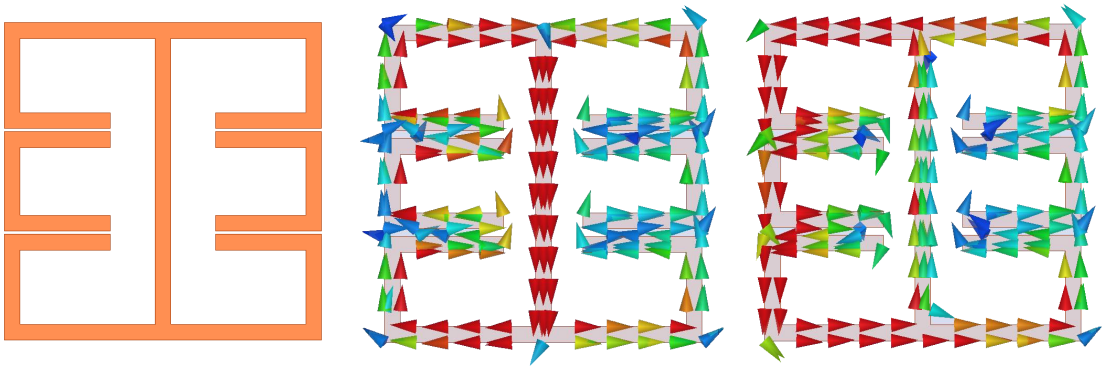

(a) (b) (c)

Figure 26: (a) A second fractal expansion of a CLS, from [82] and Chapter 4 of [47]. (b) The currents on the structure at its negative permittivity resonance. (c) the currents on the structure at its negative permeability resonance.

This metamaterial unit cell, which was first presented in [80] and later expanded upon in [81], consists of three scaled versions of the CLS units. The structure was simulated in an infinite parallel plate waveguide, which carried a TEM wave oriented as indicated in the figure, and its reflection and transmission parameters were measured. In [80, 83], the structure was shown to have high reflectance, corresponding to a single-negative behavior (see Fig. 19), at three very clear resonant frequencies, occurring at approximately 0.5 GHz, 4.2 GHz, and 13.1 GHz. The unit cell size is

approximately 32 mm, and the electrical size of the unit cell at the three resonant frequencies is approximately $\lambda_0/19$, $\lambda_0/2.3$, and $\lambda_0/0.7$, respectively. The currents on the structure are shown at 4.2 GHz, and are clearly concentrated in the four secondary subfeatures. Similarly, the currents at 13.1 GHz are concentrated in the sixteen tertiary subfeatures. This response takes advantage of the self-similarity of fractals, as was seen earlier in the Sierpinski gasket antenna from Fig. 6.

Figure 26 (a) shows a second CLS-inspired fractal metamaterial unit cell, originally published in [82], and later expounded upon in greater detail in Chapter 4 of [47]. An interesting trait of this design is that it incorporates both the 'I' shape of the CLS structure and two loops as in the SSR. Accordingly, this structure was shown to have a negative permittivity response over a bandwidth of 29.5% in a region where the electrical size of the unit cell is approximately $\lambda_0/10$, and a negative permeability response over a bandwidth of 17.5 in a region where the electrical size of the unit cell

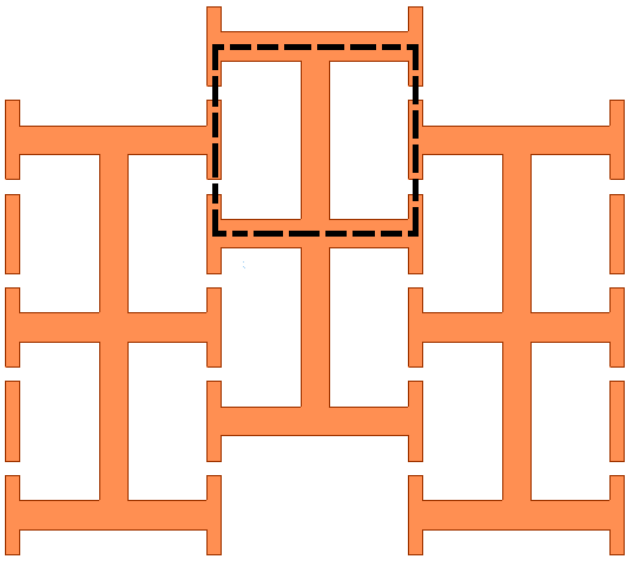

Figure 27: An interlocking grid fractal structure, originally presented in Chapter 4 of [47], with the unit cell of the structure outlined in dashed black.

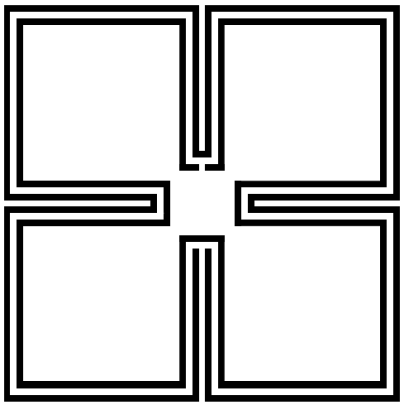

Figure 28: Sierpinski fractal for SRR, like that presented in [84].

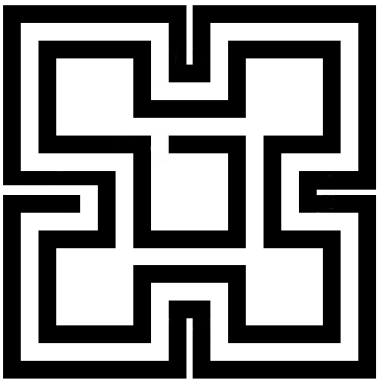

Figure 29: Hilbert fractal-based spiral resonator for negative permeability, like that presented in [85].

is approximately $\lambda_0/7$. In [84], a two dimensional fractal expansion of the SRR unit cell is presented, using a Sierpinski curve. This unit cell is shown in Fig. 28. Instead of utilizing the self-similarity characteristic, this design capitalizes on the space-filling attribute of the fractal. The resonance of this structure is shown to shift down in frequency by 35% from a traditional SRR that uses the same space. The electrical size of this unit cell at resonance was reported to be approximately $\lambda_0/16$.

Palandoken *et al.* have also presented two two-dimensional unit cell designs based on the Hilbert fractal curve. One design, shown in Fig. 29, was shown in [85] to

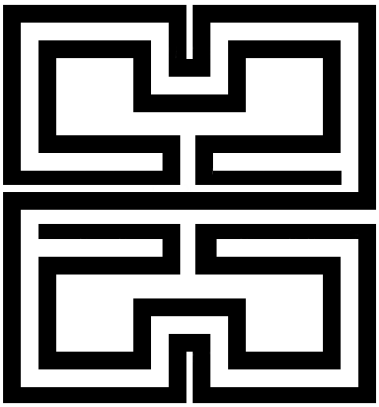

Figure 30: Hilbert fractal-based resonator for negative permittivity, like that presented in [86].

produce negative permeability at around 1.52 GHz. The unit cell size is 5 mm, which translates to an electrical size of $\lambda_0/39$. The second design, shown in Fig. 30, was shown in [86] to produce negative permittivity at around 2.75 GHz, which, for the 5 mm unit cell, corresponds to an electrical size of $\lambda_0/22$.

Two-dimensional spiral negative-permeability unit cells are also presented in [87].

Again, the obvious progression from a two-dimensional structure is to a three-dimensional structure. Two-dimensional metamaterial unit cells are highly anisotropic and do not take advantage of the third dimension for space-filling. The development of three-dimensional metamaterial unit cells is expected to enable increased electrical miniaturization of the unit cells, as well as reduced anisotropy.

2.5 Metamaterial-Loaded Horn Antennas

One of the many applications of electromagnetic metamaterials is antenna loading, where incorporation of a metamaterial structure into an antenna geometry is used to reduce the resonant frequency [66–70], to broaden or increase the number of resonant frequencies [88–93], or to improve the radiation characteristics of an antenna [94–97].

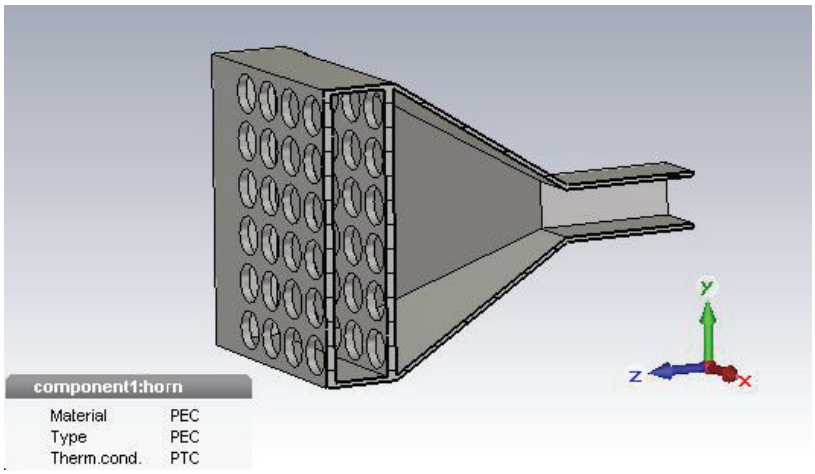

Figure 31: A metamaterial-loaded horn antenna with improved gain characteristics, from [98].

One example of metamaterial loading being used to improve the radiation characteristics of a horn antenna is presented in [98]. An epsilon-near-zero metamaterial was designed, consisting of a square lattice of circular holes through a conductive plane. Two sheets of this metamaterial were placed in the tapering mouth of a rectangular horn antenna, at an orientation normal to the direction of propagation, as shown in Fig. 31. The effect of this loading was shown to be a 3 dB increase in the gain of the antenna. The image is taken from [98].

Another radiation characteristic - polarization - was manipulated by Simmons in [99]. Here, circular polarization was obtained from a rectangular waveguide in two steps. First, the rectangular waveguide was transitioned geometrically into a square waveguide set at at 45° angle to the first waveguide. This resulted in a transmitted wave that was polarized linearly along the diagonal of the square waveguide. This linearly polarized wave along the diagonal can be thought of as two in-phase, equal-amplitude linearly polarized waves along the two square edges of the waveguide. A

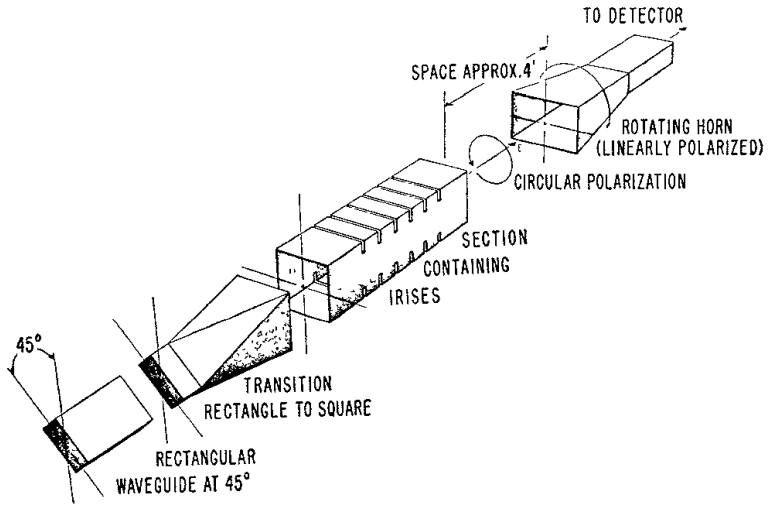

Figure 32: A horn antenna followed by a metamaterial-loaded waveguide section to induce circular polarization in the transmitted wave, from [99]

metamaterial-loaded section of square waveguide was next in the sequence. These metamaterials consisted of periodic rectangular "irises", which had a capacitive effect along one orientation of the square, and an inductive effect along the other orientation. This system is shown in Fig. 32. The discrepancy in the reactance experienced by the two wave orientations was used to induce phase differentiation, which was utilized to produce a circularly polarized wave at the radiating end of the waveguide section. Simmons reports ellipticity of polarization less than 3 dB and VSWR better than 1.5 over the frequency range 7.35 GHz to 10.3 GHz. The image is taken from [99].

Polarization was also the primary focus of the work presented in [100], where a dual-layered two-dimensionally periodic chiral metamaterial slab was placed over the end of an otherwise unaltered E-plane flared rectangular-waveguide horn antenna, as shown in 33 (a). Images are taken from [100].

The metamaterial unit cell used in this case consisted of two circular arcs placed

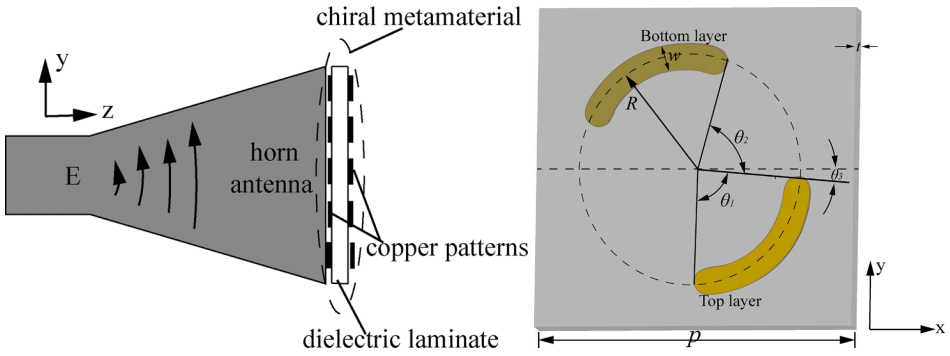

Figure 33: (a) A horn antenna with chiral metamaterial slab over radiating slot, and (b) the unit cell of the chiral metamaterial, taken from [100]

on opposite sides of a dielectric slab, as shown in Fig. 33 (b). Its use was reported to produce a left-hand circularly polarized wave at 12.45 GHz, with an axial ratio of 1.05 dB and better than -10 dB return loss, and also a right-hand circularly polarized wave at 14.35 GHz, with an axial ratio of 0.95 dB and better than -10 dB return loss. It was also reported that the gain of the antenna was decreased from its unloaded value by approximately 0.6 dB at each pertinent frequency.

CHAPTER 3: SPHERICAL SPIRAL METAMATERIAL UNIT CELL FOR NEGATIVE PERMEABILITY AND NEGATIVE PERMITTIVITY

This chapter introduces a three-dimensional spherical spiral expansion of the split ring resonator commonly used to achieve negative permeability. The spherical spiral unit cell is shown to produce negative permeability over a much wider bandwidth than the traditional split ring resonators, and also to be capable of producing wideband negative permittivity or double-negative response, depending on the orientation of the unit cell with respect to the incident electric field. A theoretical discussion of the mechanism by which these varying material parameters are produced is included.

As was mentioned in Chapter 2, one of the earliest negative-permeability unit cells was the split ring resonator (SRR), which was presented by John Pendry in 1999. These structures were simple to fabricate, and were capable of producing negative permeability. However, their performance was constrained to very narrow frequency bands, and relatively high frequencies, where the unit cells were only marginally electrically small [8]. In 2004, Baena *et al* showed that spiral resonators were capable of producing the same response as split ring resonators, but at much lower frequencies, reducing the electrical size of the unit cell [87]. Each of these two structures - the split ring resonator and the spiral resonator - can be used to achieve a negative permeability response. However, in order to achieve negative index of refraction, they must be combined with a negative permittivity structure that has been carefully

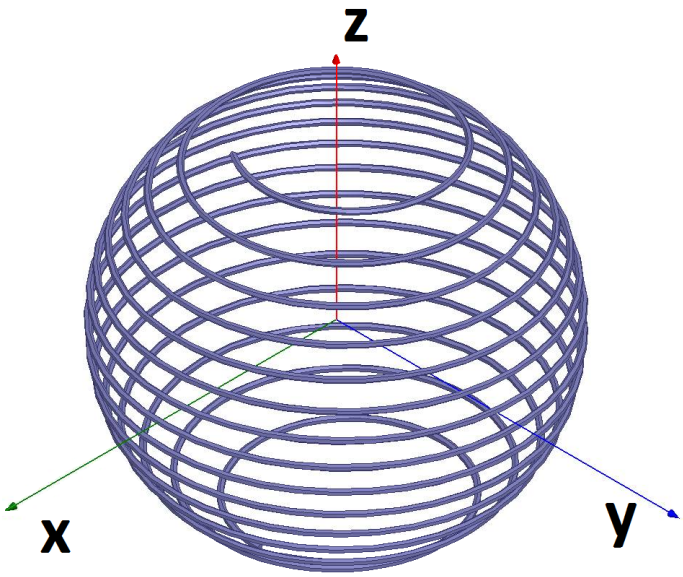

Figure 34: The spherical spiral unit cell in the "reference orientation".

tuned to resonate at the same frequency, as demonstrated by Smith *et al* in [101].

In [102], Pendry showed that three-dimensional rod-shaped metamaterials were capable of producing both negative permeability and negative permittivity with a single structure, through coupling of the electric and magnetic responses. The spherical spiral unit cell presented herein attempts to combine the simplicity of the spiral resonator with the three-dimensionality of Pendry's rods in a rotationally symmetric unit cell that is capable of producing wideband negative permeability, negative permittivity, or double-negative behavior, while maintaining a unit cell size that is extremely electrically small. Preliminary results from this line of investigation were previously published in [103].

3.1 Theoretical Discussion

The spherical spiral unit cell under investigation here is formed as a left-handed helix with respect to the z-axis, as shown in Fig. 34. It has a vertical pitch of 1.3

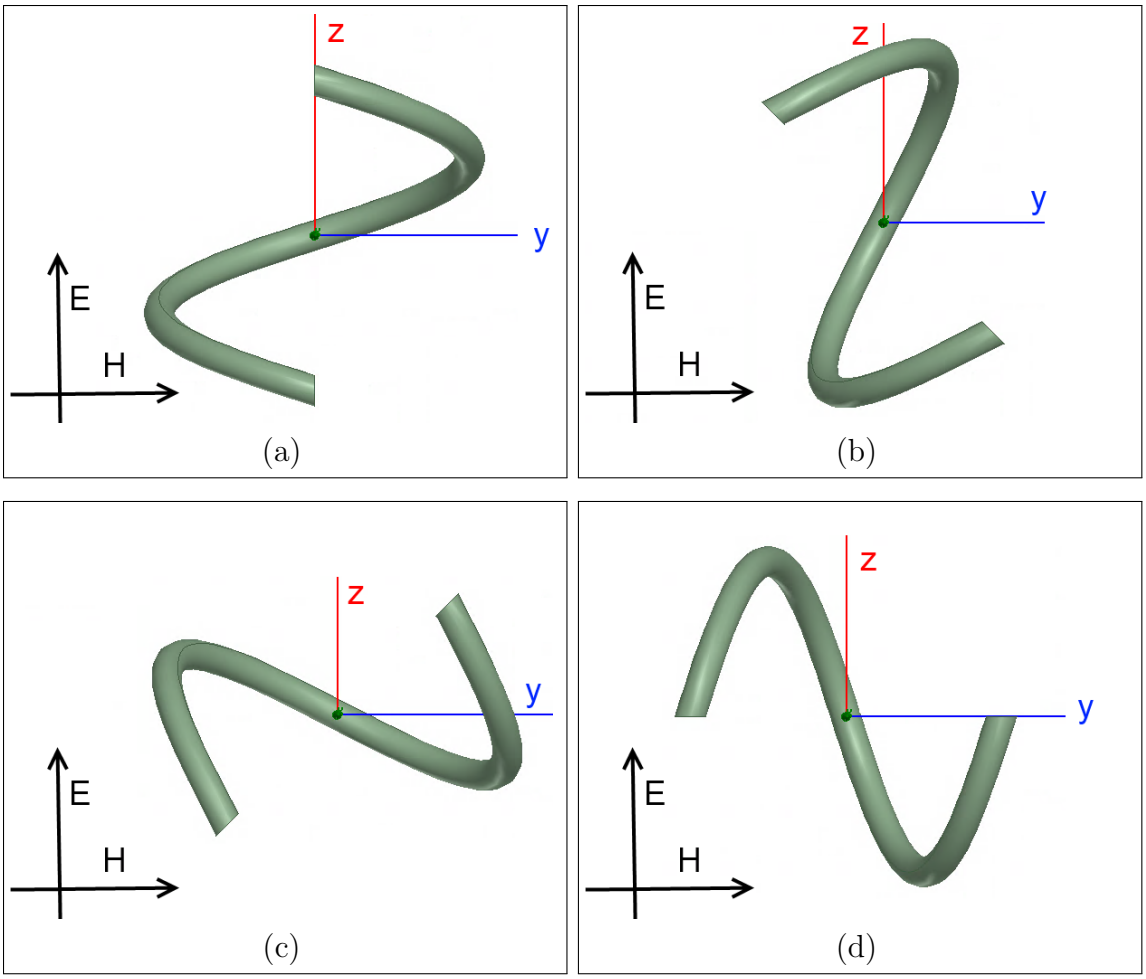

Figure 35: A single conductive loop at (a) 0° of rotation, minimizing magnetic response. (b) +45° of rotation, causing increased permeability. (c) -45° of rotation, causing decreased permeability. (d) ±90° of rotation, causing decreased permeability.

mm per turn, a wire diameter of 0.3 mm, and the radius of the helix is contoured to a sphere with radius 10.15 mm. To explore the mechanism by which the orientation of this unit cell affects its effective material parameters, we will begin by conceptually considering the simplified case of a single helical loop in four special cases:

Case 1: Excitation by TEM wave traveling in the $-\hat{x}$ direction and $\vec{E}$ pointing in $+\hat{z}$, with loop in the reference orientation, as for the spheres shown in Fig. 34.

This configuration is shown in Fig. 35 (a). In this case, the electric field aligns with the vertical component of the loop, which at every point around its circumference results in an upward directed current. The sphere in this orientation, then, appears as an LC resonator with the inductance of the wire and capacitance between the loops, and results in an electric response like that presented in [9] for the capacitively loaded strip (CLS). The advantage of the sphere in this orientation is that it fits a long length of wire into an electrically small volume, and thus resonates at a much lower frequency than a similarly-sized traditional CLS. The loops are orthogonal to the magnetic field, so the magnetic response in this case is minimal.

Case 2: Excitation by TEM wave traveling in the $-\hat{x}$ direction and $\vec{E}$ pointing in $+\hat{z}$, with loop turned by some positive angle θ around the x-axis where $0° < \theta < 90°$. This configuration is shown in Fig. 35 (b). In this case, the portions of the loop on the $-\hat{x}$ side of the unit cell are more vertical than the portions on the $+\hat{x}$ side. This means that the electric field will interact more strongly with the $-\hat{x}$ side of the loop. For electric field pointing upward, this will result in a net upward current, which will push a magnetic field down and toward $+\hat{y}$, in alignment with the incident magnetic field. This will result in an effective increase in permeability.

Case 3: Excitation by TEM wave traveling in the $-\hat{x}$ direction and $\vec{E}$ pointing in $+\hat{z}$, with loop turned by some negative angle $-\theta$ around the x-axis, where $-90° < -\theta < 0$. This configuration is shown in Fig. 35 (c). In this case, the portions of the loop on the $+\hat{x}$ side of the unit cell are more vertical than the portions

on the $-\hat{x}$ side. This means that the electric field will interact more strongly with the $+\hat{x}$ side of the loop. For electric field pointing upward, this will result in a net upward current, which will push a magnetic field down and toward $-\hat{y}$, in opposition to the incident magnetic field. This will result in an effective decrease in permeability.

Case 4: Excitation by TEM wave traveling in the $-\hat{x}$ direction and $\vec{E}$ pointing in $+\hat{z}$, with loop turned by an angle θ around the x-axis, where $\theta = \pm 90°$. This configuration is shown in Fig. 35 (d). As the angle of θ approaches $\pm 90°$, the electric field interaction with the loop decreases dramatically, because the currents induced on the $+\hat{x}$ and $-\hat{x}$ sides of the loop cancel one another. The magnetic field interaction, however, increases, because the loop becomes aligned with the incident magnetic field. For an upward-pointing $\vec{E}$, the incident magnetic field is left-to-right, which induces a right-to-left magnetic response, resulting in an effective decrease in permeability.

3.2 Simulation of Spherical Spiral Metamaterial

Ansys HFSS was used to simulate three of the spherical spiral unit cells in an ideal parallel plate waveguide with dimensions $266 \times 22 \times 22$ mm, where the two sides of the box normal to $\hat{z}$ were defined as perfect electric conductor (PEC), the two sides of the box normal to $\hat{y}$ were defined as perfect magnetic conductor (PMC), and the two sides of the box normal to $\hat{x}$ were waveports, as shown in Fig. 36. This orientation of the unit cells in the waveguide, with the axis of the helices aligned with the electric field, will be termed the "reference orientation" of the unit cells. Each waveport was deembedded by 100 mm, leaving an effective length of 66 mm, and an

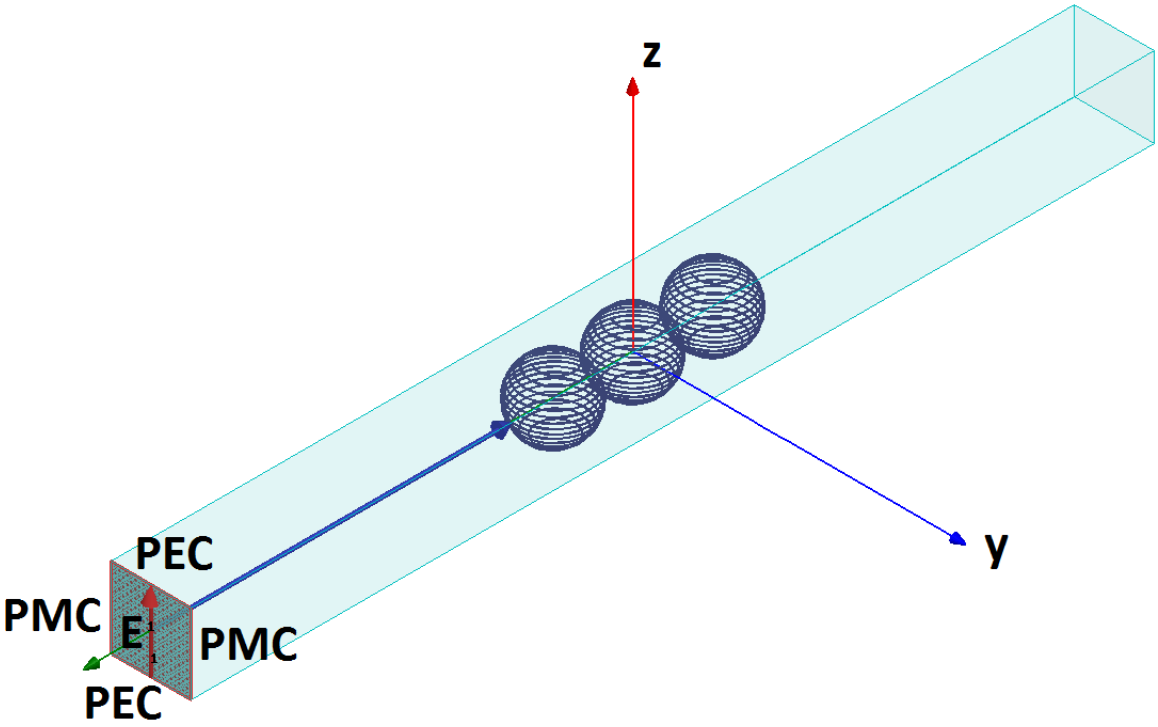

Figure 36: Three spherical spiral unit cells in the reference orientation in an infinite parallel plate waveguide.

effective lattice constant of 22 mm. The S-parameters resulting from this simulation were used to calculate the effective material parameters of the unit cells, using the methods described in [104] and [105], both of which returned comparable results.

The material parameters resulting from this simulation are shown in Fig. 37 (a), where the real part of permittivity is shown in solid red, and the real part of permeability is shown in dashed magenta. As can be seen, this simulation showed a region of negative permittivity from 154 to 232 MHz, which is a bandwidth of 40.4%.

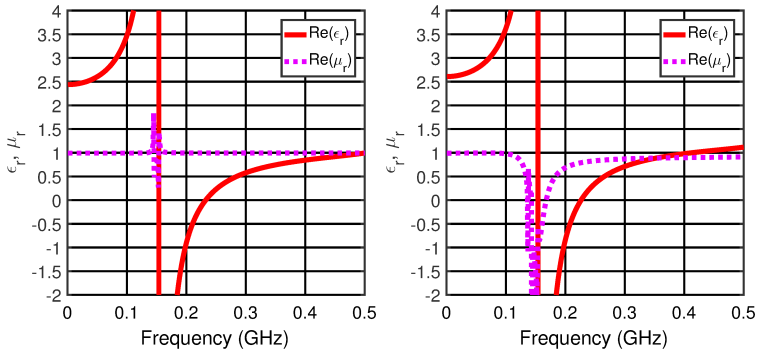

(a) Rotation = 0°

(b) Rotation = -22.5°

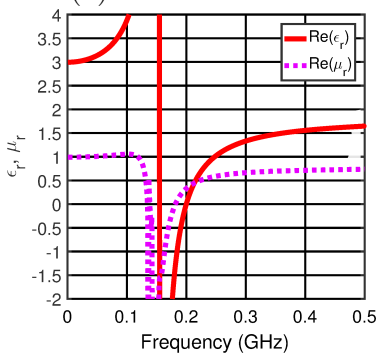

(c) Rotation = -45°

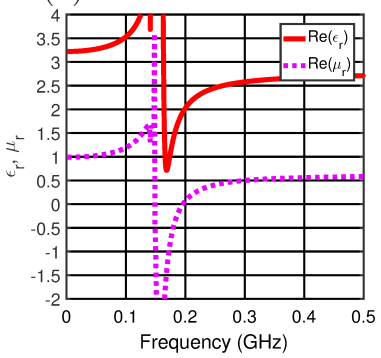

(d) Rotation = -67.5°

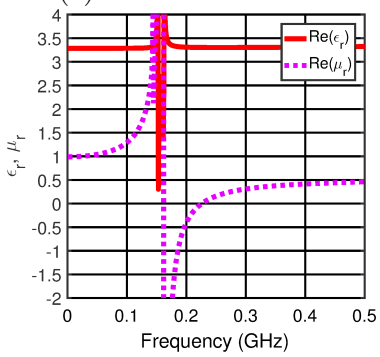

(e) Rotation = ±90°

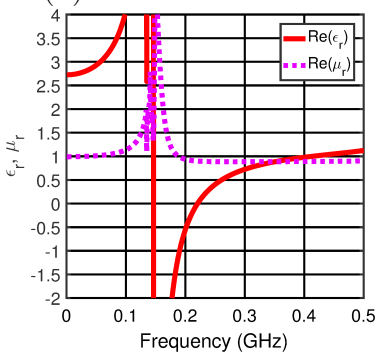

(f) Rotation = +22.5°

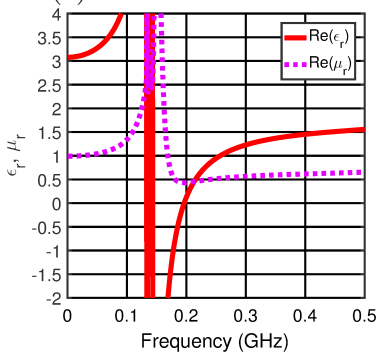

(g) Rotation = +45°

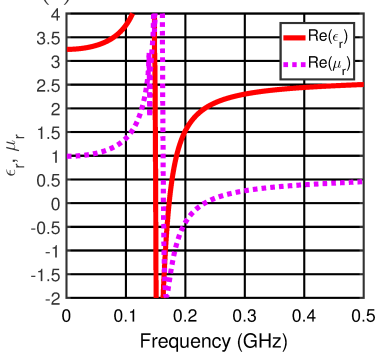

(h) Rotation = +67.5°

Figure 37: Simulated material parameters for three unit cells turned around the x-axis from the reference orientation by (a) 0° (b) -22.5° (c) -45° (d) -67.5° (e) ±90° (f) +22.5° (g) +45° (h) +67.5° The real and part of permittivity is shown in solid red, and the real part of permeability is shown in dotted magenta.

Table 1: Tabulated extracted material parameters resulting from simulation of spherical spiral unit cells at various rotation angles around the x-axis

Rotation Angle	Range of $\epsilon_r < 0$ (MHz)	Range of $\mu_r < 0$ (MHz)	Range of $\mu_r < 0$, $\epsilon_r < 0$ (MHz)
0°	154-232 (40.4%)	NA	NA
-22.5°	154-227 (38.3%)	143-168 (16.0%)	154-168 (8.7%)
-45°	155-199 (24.9%)	139-181 (26.3%)	155-181 (15.5%)
-67.5°	NA	149-196 (27.2%)	NA
± 90°	NA	164-226 (31.7%)	NA
+22.5°	146-220 (40.4%)	NA	NA
+45°	143-196 (31.2%)	NA	NA
+67.5°	150-173 (14.2%)	163-233 (35.4%)	163-173 (5.9%)

Seven additional simulations were performed, to show the effect of rotating the unit cells around the x-axis. The results from these simulations are shown in Fig. 37. As can be seen, the trend for increasingly negative rotation angles is that the strength of the negative permittivity response seen in Fig. 37 (a) diminishes, and a negative permeability response emerges in its place. At a 45° angle of rotation, the simulation results in Fig. 37 (c) show a region of negative permittivity from 155 to 199 MHz, and a region of negative permeability from 139 to 181 MHz. These two regions overlap from 155 to 181 MHz, which is a double-negative bandwidth of 15.5%. When the unit cell is turned by a complete ±90° from the reference orientation, the extracted parameters show a region of negative permeability from 164 to 226 MHz, a bandwidth of 31.7%. Figs. 37 (f), 37 (g), and 37 (h) show the effect of rotating the unit cells in the positive direction around the x-axis. As shown, small angles

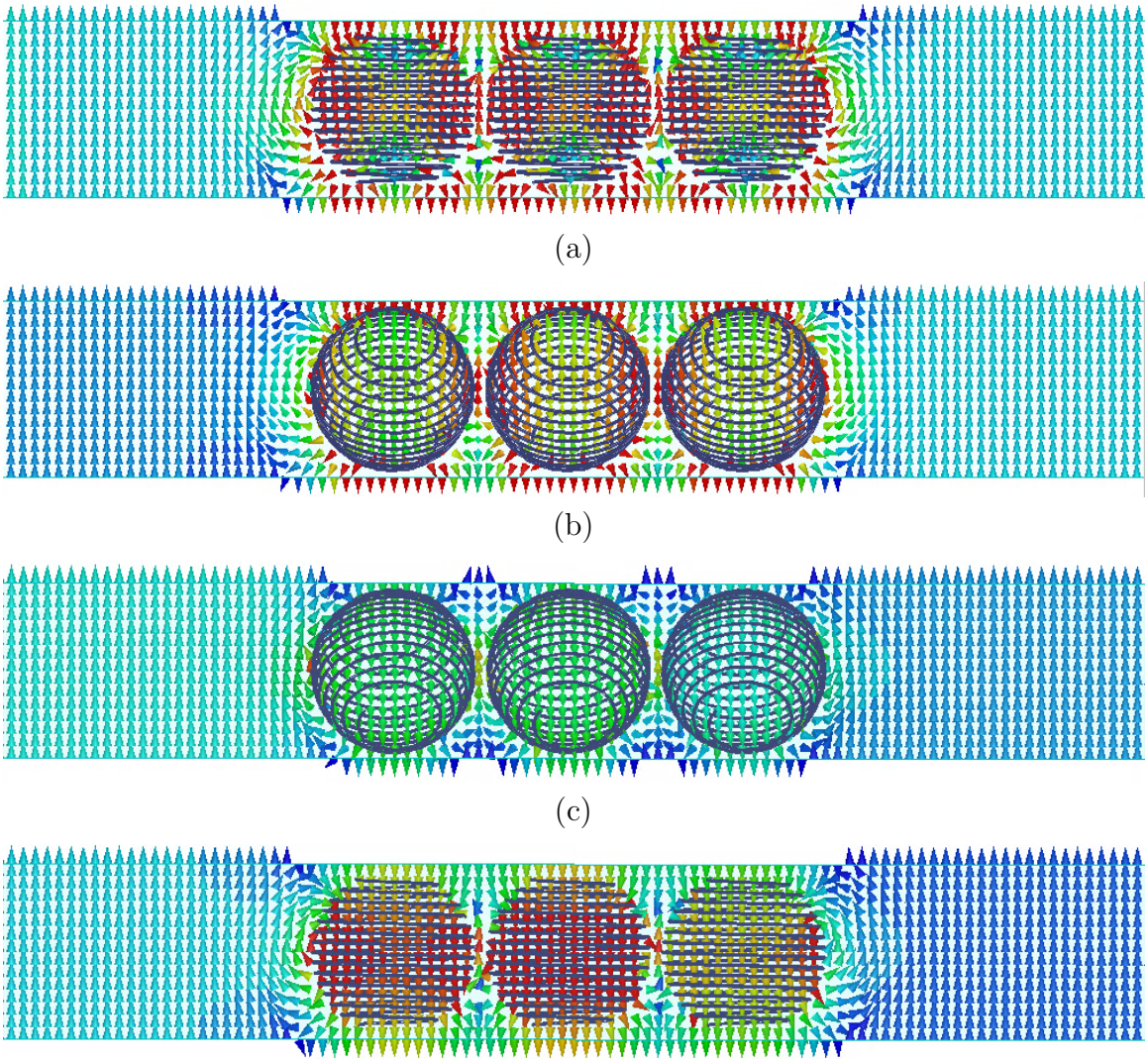

Figure 38: Fields in the guide for 175 MHz excitation from the left (a) Electric field at 0° rotation, viewed from $+\hat{y}$. (b) Electric field at $-45°$ rotation, viewed from $+\hat{y}$. (c) Magnetic field at $-45°$ rotation, viewed from $+\hat{z}$. (d) Magnetic field at 90° rotation, viewed from $+\hat{z}$.

of positive rotation tended to result in positive magnetic susceptibility, rather than the negative magnetic susceptibility shown in the previous simulation. The results of these eight simulations are summarized in Table 1.

To ensure accuracy of the extracted values, we investigate the fields in the guide at the frequencies of negative parameter values. Fig. 38 (a) shows the electric field in

the waveguide at 175 MHz for the case where the rotation angle was 0°, viewed from the positive $\hat{y}$ direction. This snapshot shows the incoming electric field from the left pointing upward, and the electric field in the region of the unit cells pointing downward. This confirms the extracted negative permittivity at this frequency. Similarly, Fig. 38 (b) shows the electric field in the waveguide at 175 MHz for the case where the rotation angle was $-45°$, and confirms the negative permittivity extraction. Figs. 38 (c) and 38 (d) show the magnetic field in the waveguide at 175 MHz for the cases where the rotation angle was $-45°$ and 90°, respectively. These magnetic fields are viewed from the positive $\hat{z}$ direction. In both these cases, the field reversal in the region of the unit cells confirms the negative permeability extraction.

3.3 Measurement of Spherical Spiral Metamaterial

Fabrication of these unit cells was made simple through the use of a Makerbot Replicator 2X 3D printer. Spherical forms were printed of ABS plastic, with ridges to guide wire wrapping. Fig. 39 (a) shows three such plastic forms in the process of being 3D printed, and Fig. 39 (b) shows the finished forms. These forms were printed with a 10% fill, so that they would be mostly hollow and not significantly affect the measurements. Each spherical form was then wrapped with 20 gauge copper magnet wire, secured with glue, as shown in Fig. 39 (c).

A test fixture was built using 1/16" copper clad FR-4 circuit board. Either end of the fixture was fed with a 20 mm length of 50 Ω microstrip. As shown in Fig. 41, each microstrip section was followed by a 100 mm long transition section which increased linearly in both width and height to match to the waveguide section, which was 200

mm long, 100 mm wide, and 22 mm high. Thru-Reflect-Line (TRL) calibration was used to calibrate out all of this test fixture except a 66 mm section in the center. Since this structure has a finite width, some fringing will occur along the edges, reducing the effect of any material placed inside the waveguide. To illustrate this, a simulation was conducted of the test fixture with a chunk of dielectric under the waveguide where

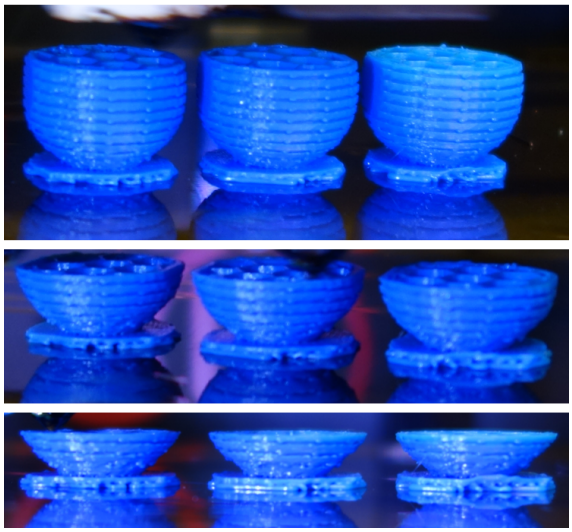

(a)

(b)

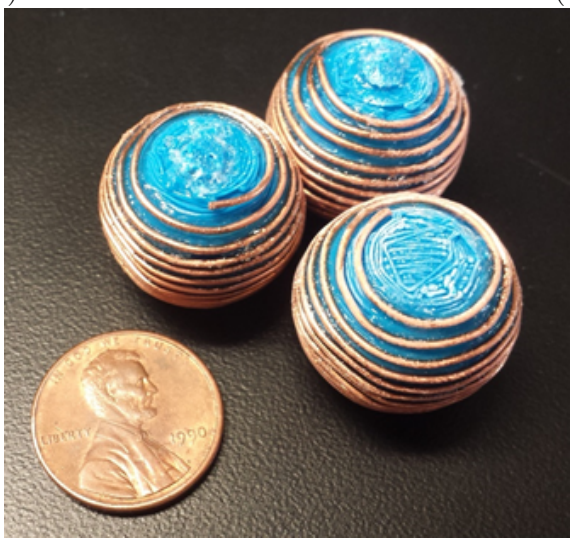

(c)

Figure 39: (a) Three ABS forms in the process of being printed. (b) Three completed ABS forms. (c) ABS forms wrapped with 20 gauge magnet wire.

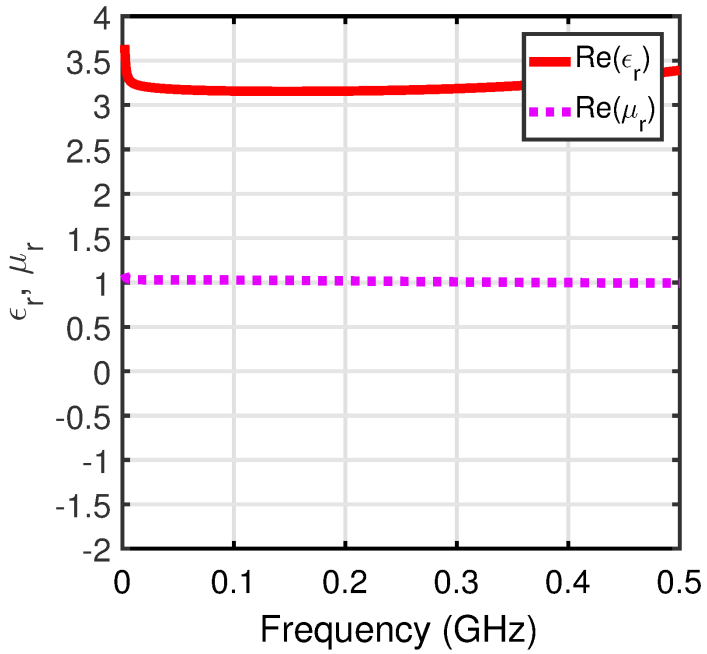

Figure 40: Extracted material parameters for simulation of chunk of dielectric $\epsilon_r = 4.4$ in the test fixture.

$\epsilon_r = 4.4$. The extracted parameters resulting from this simulation are shown in Fig. 40. As shown, the extracted dielectric constant is approximately 3.2, which is 73% of the actual value. This weakening of the response, here demonstrated in simulation, will also be apparent in the following measurements.

The fabricated test fixture is shown in Fig. 42 (a). This fixture was used to measure the row of three unit cells in the reference orientation, centered in the waveguide section of the fixture. The results from this measurement are shown in Fig. 43 (a). The measured response is shown to be much weaker than the simulated response, resulting in a much narrower bandwidth of performance. The graph shows measured negative permeability from 146 to 159 MHz, which is a bandwidth of 8.5%. Two factors are responsible for this weakening of the response. Firstly, as discussed earlier, some of the electric fields fringe around the sides of the fixture without being affected

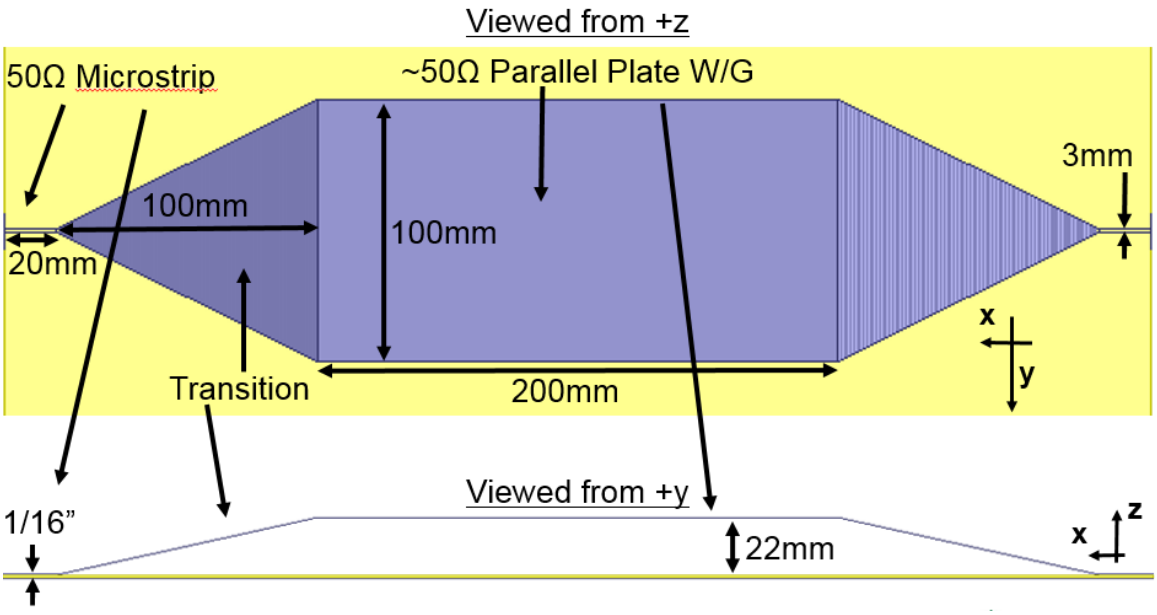

Figure 41: HFSS model of a parallel plate waveguide section fed by microstrip.

by the unit cells. This does not occur in the simulation, because of the perfect magnetic conductor boundaries. Secondly, the measurement is of one row of unit cells in 100 mm of waveguide width, whereas the simulation was of one row of unit cells in 22 mm of waveguide width. This second point may be alleviated by increasing the number of unit cells under the waveguide. Therefore a second measurement was conducted with three evenly spaced rows of unit cells under the waveguide, as shown in Fig. 42 (b). This resulted in the material parameter graph shown in Fig. 43 (b). As shown, increasing the fill factor in this way increased the strength of the response, and therefore the bandwidth. This second measurement shows negative permittivity from 153 to 187 MHz, a bandwidth of 20%. Though this measurement still has a narrower bandwidth than the simulated case, because of fringing, a comparison of Figs. 37 (a) and 43 (b) shows very good correlation between simulated and measured

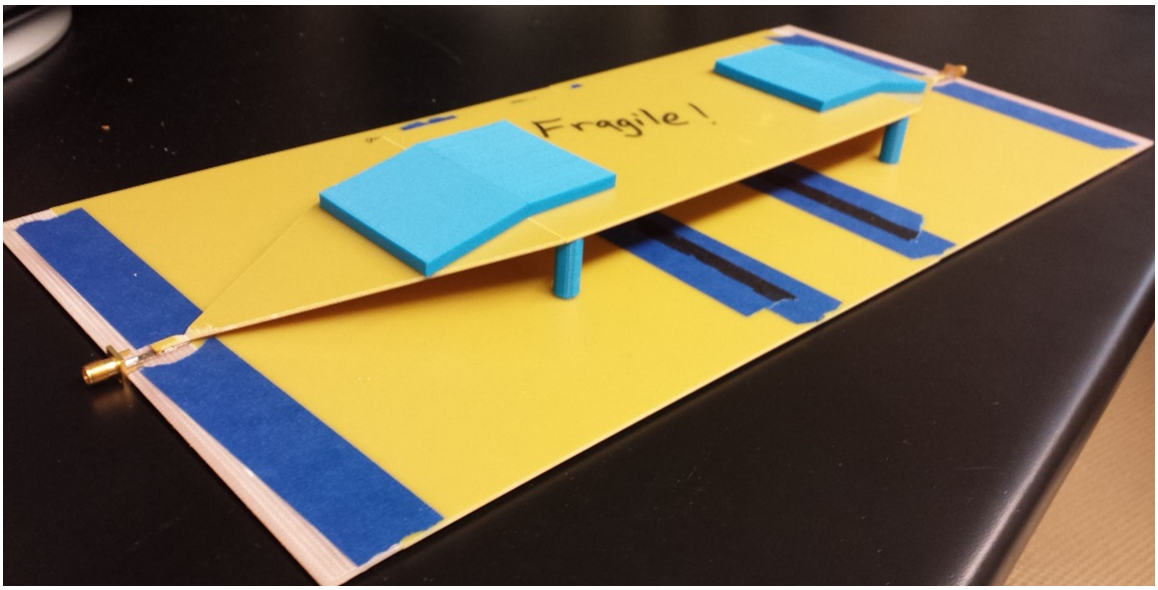

(a)

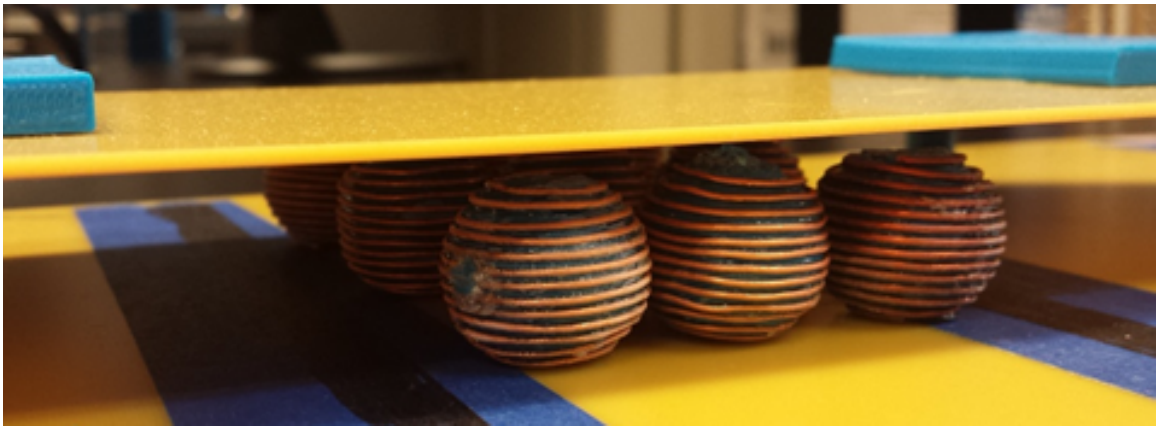

(b)

Figure 42: (a) Fabricated parallel plate waveguide section fed by microstrip. (b) Nine unit cells under the waveguide.

results.

A measurement was also made of the three unit cells rotated by -90° from the reference position. The results from this simulation are shown in Fig. 43 (c). This measurement shows negative permeability from 161 to 169 MHz, which is a bandwidth of 4.8%. As in the previous case, the measured results are much narrower bandwidth than the simulated results. Also as before, a second measurement including three

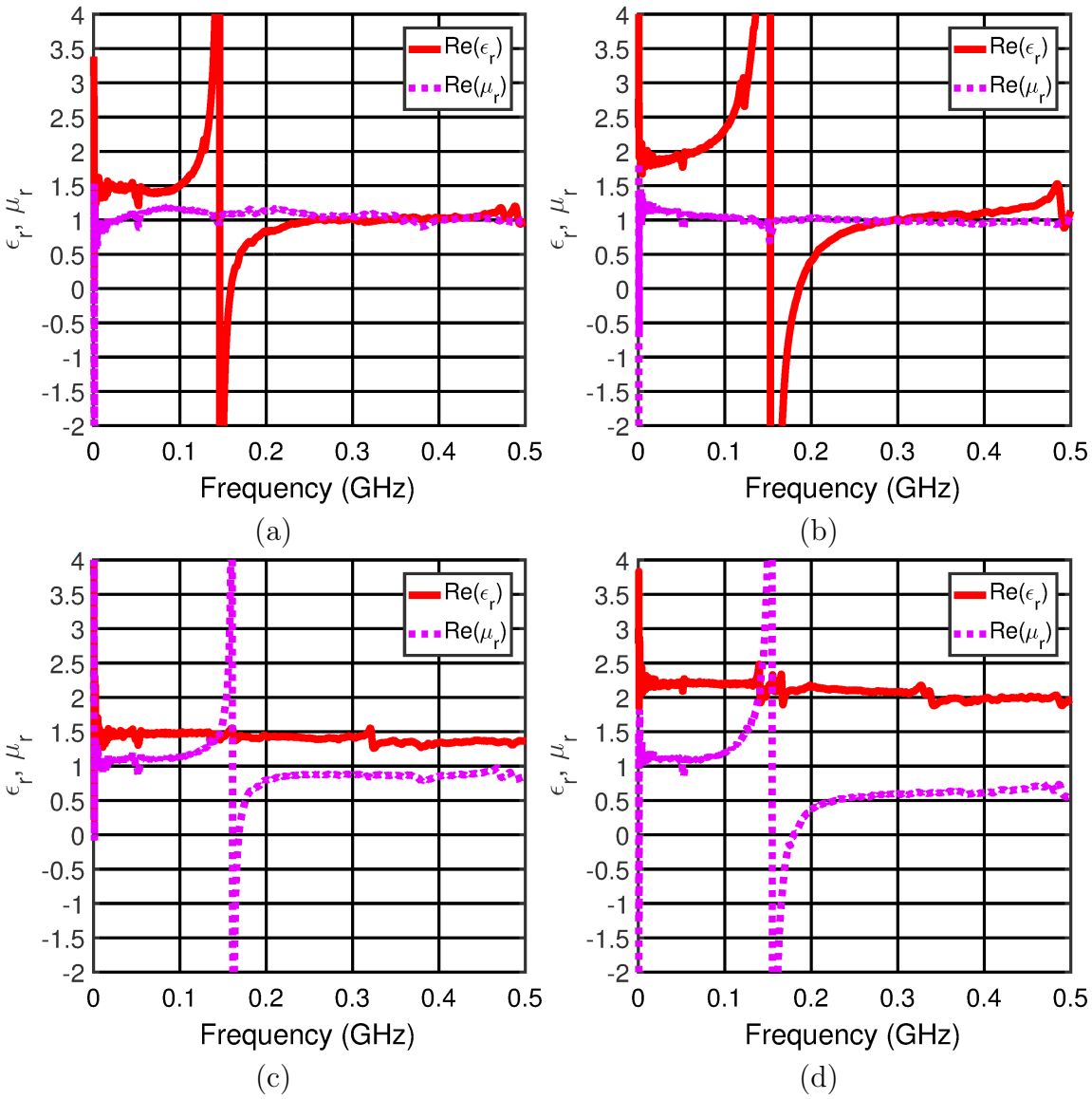

Figure 43: Measured material parameters for (a) three unit cells in the reference orientation. (b) nine unit cells in the reference orientation. (c) three unit cells turned by -90° from the reference orientation. (d) nine unit cells turned by -90° from the reference orientation.

rows of unit cells was conducted. The results from this measurement of nine unit cells is shown in Fig. 43 (d). As before, increasing the number of unit cells is shown to increase the strength of the response, and therefore the bandwidth. This time, negative permeability is measured from 154 to 182 MHz, a bandwidth of 16.7%. Again, though fringing causes this response to still be weaker than in simulation, a

comparison of Figs. 37 (b) and 43 (d) shows very good correlation between simulated and measured results.

Fig. 44 shows the results from two additional simulated and measured configurations. Fig. 44 (a) shows the extracted parameters for a simulation of four rows of three unit cells, where the first and third rows are in the reference orientation and the second and fourth rows are rotated by 90° from the reference orientation. Fig. 44 (c) shows the corresponding measured parameters. This measurement shows a region of negative permittivity from 147 to 160 MHz, a bandwidth of 8.4%, and a region of negative permeability from 155 to 173 MHz, a bandwidth of 11%. Each of these responses is narrower than in the respective individual cases (i.e the 0° and 90° rotation cases), which is due to the relatively low fill factor (approximately 50% for each orientation). Fig. 44 (c) shows the extracted parameters for a simulation of four rows of three unit cells, where half the unit cells are in the reference orientation and half the unit cells are rotated by 90°, and the reference and rotated cells are arranged in a checkerboard pattern. Fig. 44 (d) shows the corresponding measured parameters. This measurement shows a region of negative permittivity from to 137 to 145 MHz and a region of negative permeability from 137 to 142 MHz, as well as from 143 to 146 MHz. It had previously been shown that double-negative behavior could be achieved through adjusting the orientation of the unit cells (Fig. 37). These two measurements show that double-negative behavior can also be achieved through combining negative-permittivity-oriented cells at 0° of rotation and negative-permeability-oriented cells at 90° of rotation.

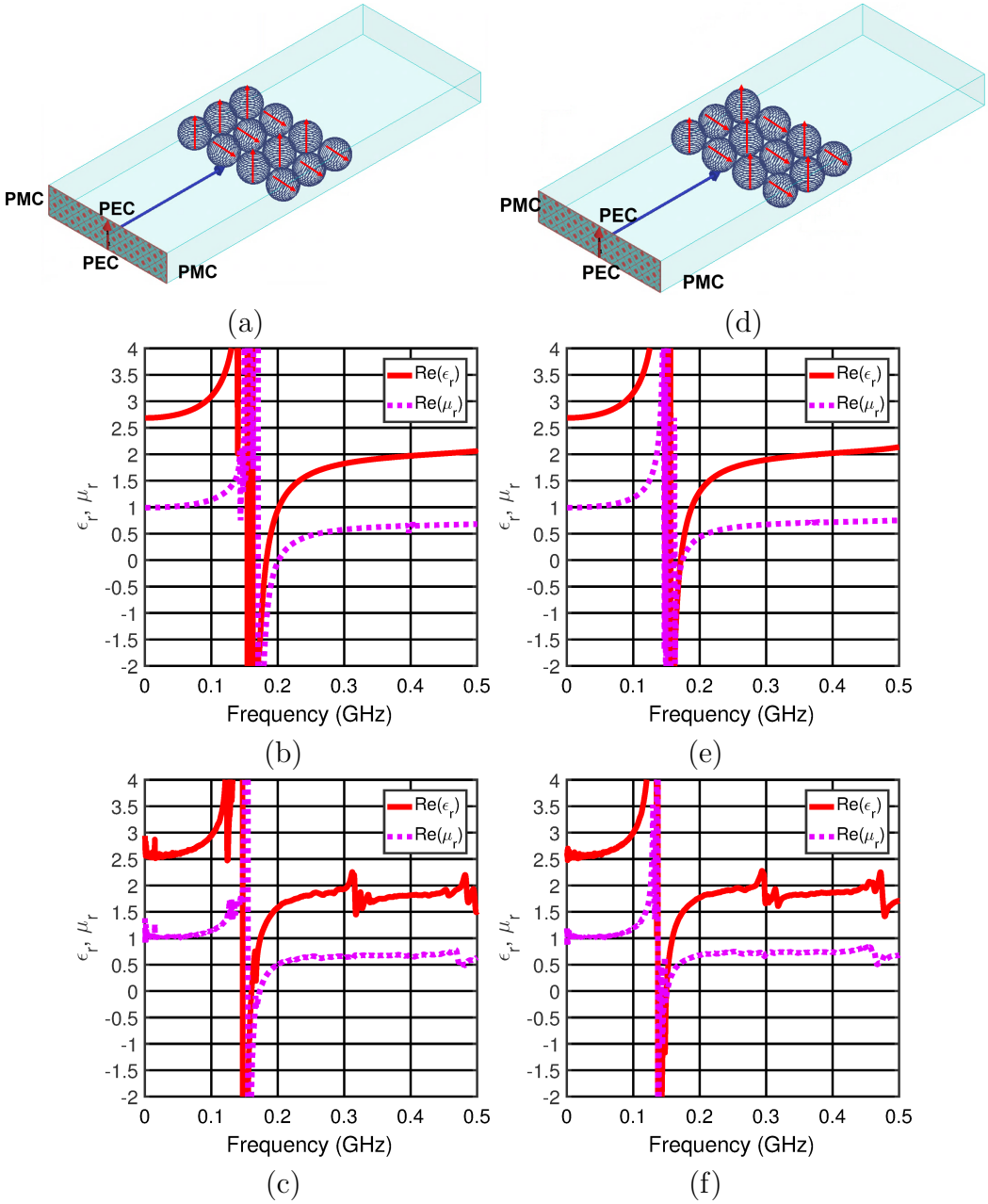

Figure 44: (a) HFSS simulation of four rows of three unit cells, where the first and third rows are in the reference orientation, and the second and fourth rows are turned by 90° from the reference orientation. (b) Material parameters resulting from simulation of configuration shown in (a). (c) Material parameters resulting from measurement of unit cells arranged as in (a), in the finite parallel plate waveguide test fixture. (d) HFSS simulation of four rows of three unit cells, where half the unit cells are in the reference orientation and half the unit cells are rotated by 90°, and the reference and rotated cells are arranged in a checkerboard pattern. (e) Material parameters resulting from simulation of configuration shown in (d). (f) Material parameters extracted from measurement of unit cells arranged as in (d), in the finite parallel plate waveguide test fixture.

3.4 Chapter Summary

A spherical spiral metamaterial unit cell was introduced, combining the simplicity of the traditional planar spiral resonators with three-dimensionality to achieve a double-negative response. The unit cell was shown in both simulation and measurement to be capable of producing negative permeability, negative permittivity, or both, solely by changing the orientation of the unit cells with respect to the incident electric field. It was also shown in two different measurements that a combination of variously oriented unit cells could be used to produce an aggregate result. Specifically, it was shown that negative permittivity cells and negative permeability cells could be used in combination to produce a measured double-negative response. All these simulated and measured responses occur at frequencies where the unit cell is smaller than $\lambda_\circ/60$.

CHAPTER 4: A MULTIBAND RINGED RECTANGULAR PATCH ANTENNA

Multiband antennas help to maximize space efficiency by enabling multiple applications to utilize a single device. This is especially useful in environments where space or resources are limited, such as on crowded radio towers or in military communication applications. Electrical miniaturization can be used to further enhance this spatial consolidation.

Microstrip patch antennas, like that shown in Fig. 45 (a), are attractive because they are low-profile and easy to fabricate. However, they typically operate over a single narrow band of frequencies where the length of the patch is approximately half a wavelength, as shown in Fig. 45 (b). In the dominant resonant mode, broadside radiation is formed, originating from concentrated electric fields along the two shorter ends of the patch [106]; this radiation pattern is shown in Fig. 45 (c). This paper introduces a ringed rectangular patch antenna with four distinct resonant frequencies, each of which occurs at a lower frequency than the electrical size of the patch would ordinarily support. This ringed rectangular patch antenna maintains the low profile and ease of fabrication common to traditional patch antennas, while incorporating fractal-inspired geometric modifications to achieve a self-similarity-induced multiplicity of resonances, as noted in [21,28,55–57,59,60], among others. The fractal-inspired modification consists of five gaps of width 0.6 mm, which are introduced around the edges of the patch as shown in Fig. 46. These have been carefully designed so that

the current distribution and radiation pattern of the resulting fractal patch antenna approximately match those of a traditional patch at each of the four resonant frequencies.

Simulation of several small variations of this geometry is used to demonstrate design adaptability. The first four of these variations show the effect of removing a portion of the patch geometry, such as the center rectangle or a single ring from the perimeter of the antenna. The following two variations show the result of lengthening all or one of the rings. The final two variations show the effect of deviating from the rectangular overall shape, to better utilize the space in the center of the antenna.

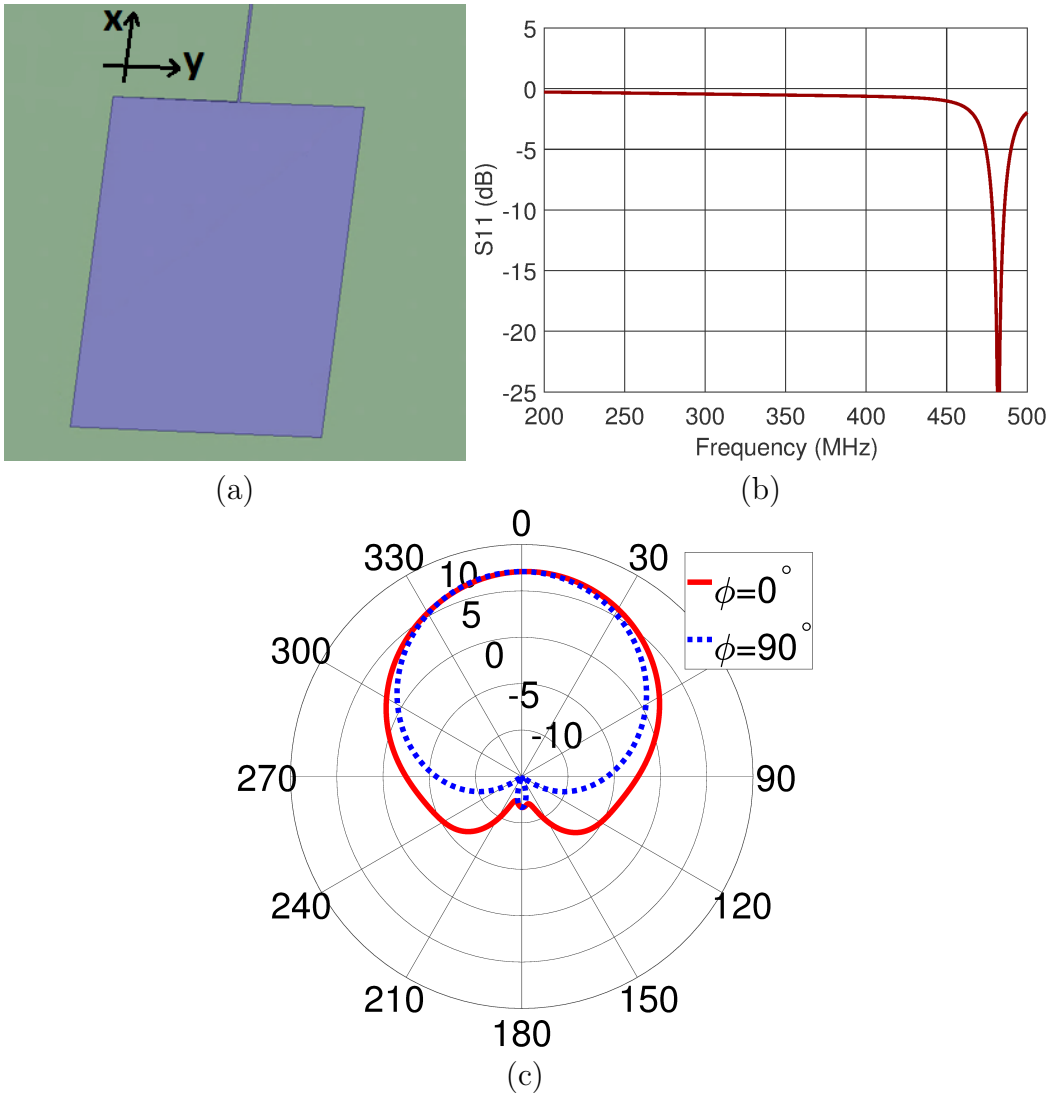

Figure 45: (a) A traditional rectangular patch antenna with length 147.9 mm and width 90.4 mm. (b) The return loss of the traditional rectangular patch antenna, as simulated in HFSS. (c) The directivity of the traditional rectangular patch antenna, plotted on the $\phi = 0°$ (solid red) and $\phi = 90°$ (dotted blue) planes.

4.1 Ringed Rectangular Patch Antenna

The rectangular ringed patch was simulated in HFSS, with a radiating element having a total length of 147.9 mm, and a total width of 90.4 mm. An FR-4 substrate of 1.5 mm thickness and $\epsilon_r = 4.4$ was used to separate the radiating element from an infinite ground plane. As shown in Fig. 46, this patch was modified from the

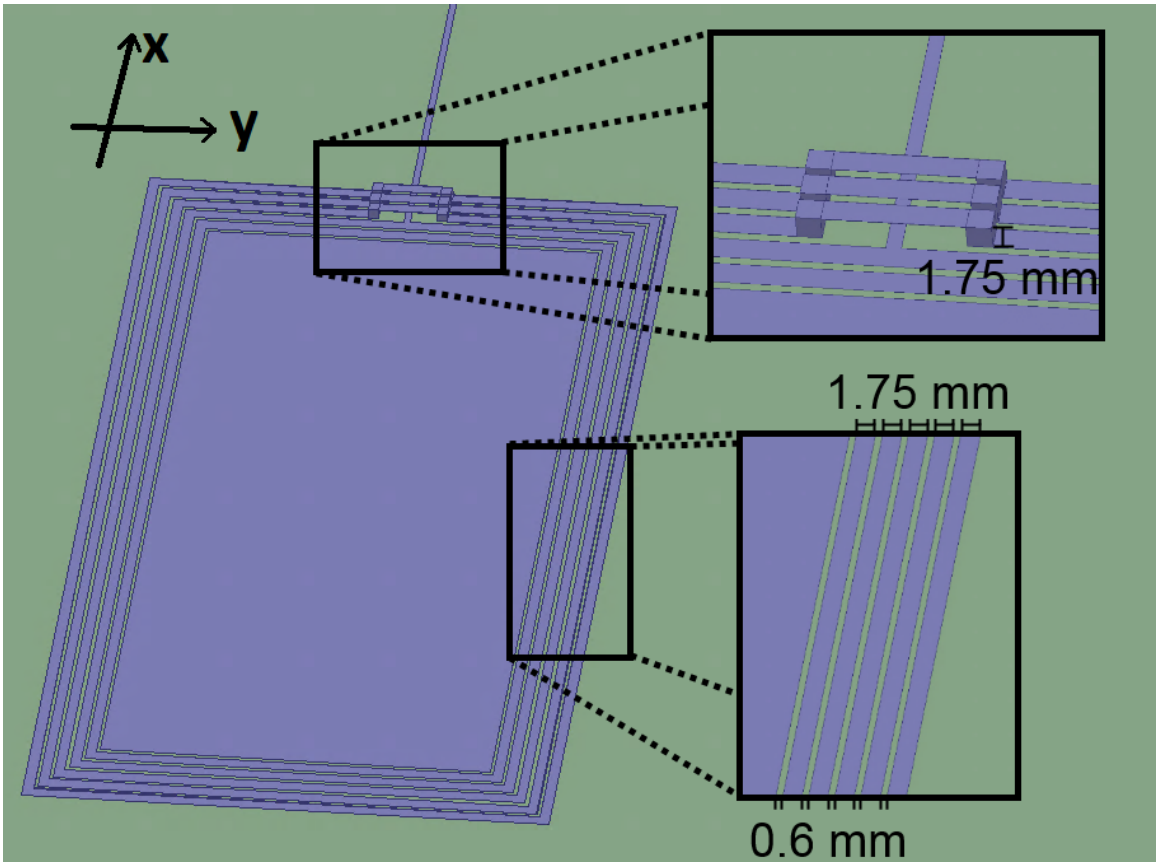

Figure 46: The ringed rectangular patch antenna.

traditional rectangular patch antenna geometry by introduction of five gaps, each having width 0.6 mm, at 1.75 mm intervals around the perimeter of the rectangular radiating element.

The feed structure for this antenna is also shown in Fig. 46. As can be seen, a section of the patch is raised from the plane of the substrate surface by 1.75 mm to allow the microstrip feed to pass under the first three metal rings, making the feed connection at the fourth ring. This microstrip line has a width of 1.06 mm, and a characteristic impedance of approximately 85 Ω.

Fig. 48 shows the magnitude of the return loss in dB for the simulation of the

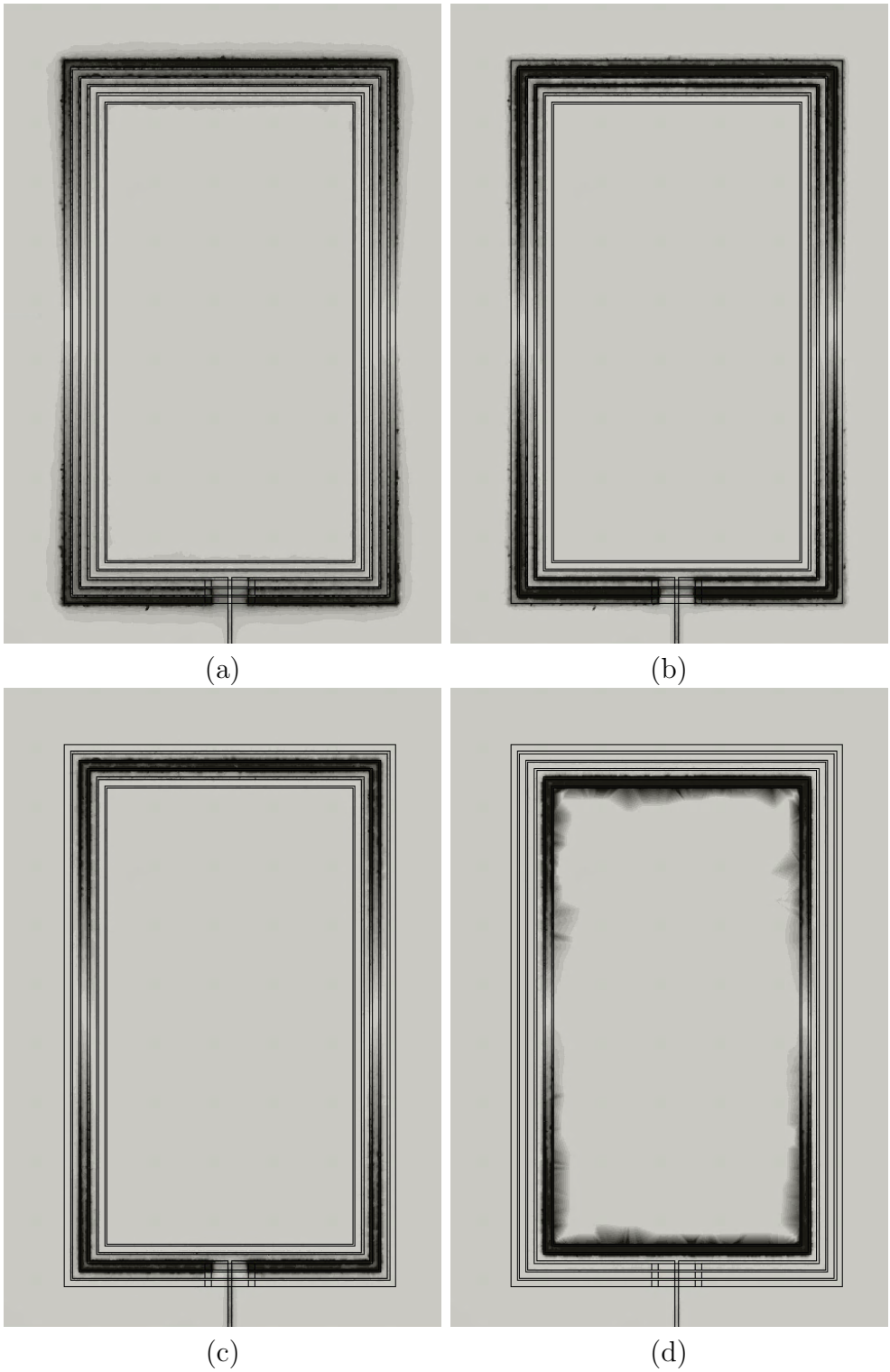

Figure 47: Magnitude of the electric field on the upper surface of the substrate from the simulation of the ringed rectangular patch antenna at (a) 353 MHz, (b) 389.5 MHz, (c) 412.5 MHz, and (d) 446 MHz.

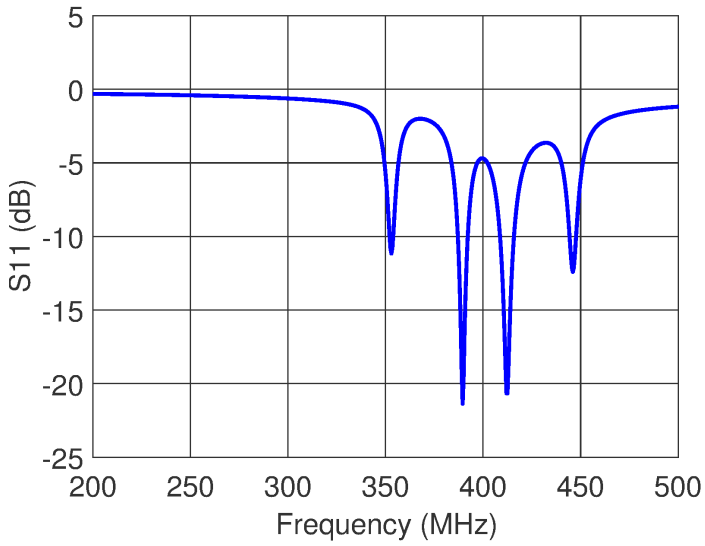

Figure 48: Return loss in dB for the ringed rectangular patch antenna.

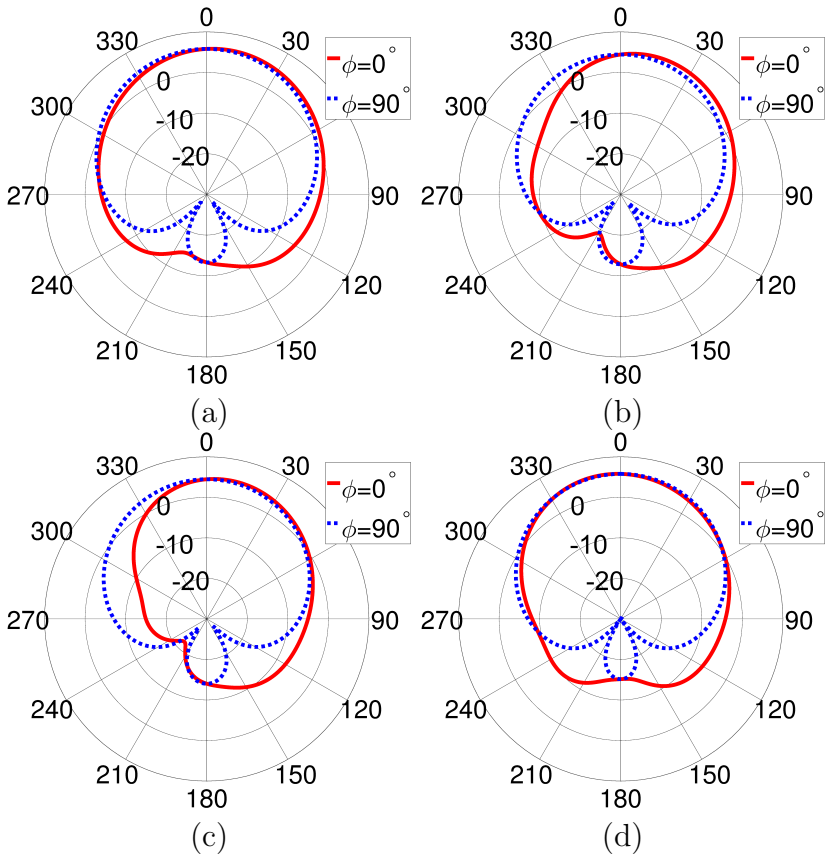

Figure 49: Directivity on the $\phi = 0°$ and $\phi = 90°$ planes of the ringed rectangular patch antenna, simulated at (a) 353 MHz, (b) 389.5 MHz, (c) 412.5 MHz, and (d) 446 MHz, shown in dB.

rectangular ringed patch antenna from 200 MHz to 500 MHz. This simulation shows four resonant frequencies, at 353 MHz, 389.5 MHz, 412.5 MHz, and 446 MHz. To observe the mechanism for these four resonances, Fig. 47 shows the magnitude of the electric field on the upper surface of the FR-4 substrate at each of the resonant frequencies of the patch.

At the lowest frequency of resonance, in Fig. 47 (a), we can observe that the highest field concentration is located under the outermost conductive ring, at the two radiating slots of the antenna. This is what we would ordinarily expect from a microstrip patch antenna operating in its dominant mode. Fig. 47 (b) shows the field concentration on the surface of the substrate at the second frequency of resonance. Here we see that the electric field is most highly concentrated under the second-outermost conductive ring, and in the first and second gaps. This indicates that a smaller subsection of the radiating element has become active at this higher frequency. This is a common characteristic of fractal antennas, as has been demonstrated previously in [21, 28]. Similarly, at the third resonance, in Fig. 47 (c), the fields are concentrated under the third and fourth gaps, and at the fourth resonance, shown in Fig. 47 (d), high field concentration is observed under the fifth and final ring, and under the fourth and fifth gaps.

The far field radiation pattern of the antenna at each resonant frequency is shown in Fig. 49, where the directivity on the $\phi = 0^\circ$ plane is plotted in solid red, and the directivity on the $\phi = 90^\circ$ plane is plotted in dotted blue. The directivity of the antenna directly above the patch is shown to be 5.80 dB at 353 MHz, 4.43 dB at 389.5 MHz, 4.45 dB at 412.5 MHz, and 5.78 dB at 446 MHz. In every case, the shape

of the radiation pattern closely matches that of a traditional patch antenna.

4.2 Variations on the Rectangular Ringed Patch Antenna

In order to demonstrate design adaptability, several variations on the basic ringed patch antenna geometry were investigated. Four of these variations involve removing portions of the antenna geometry, two involve changing dimensions, and two involve adaptations to the originally rectangular overall shape of the patch.

4.2.1 Removing Various Patch Elements

The first of the variant patch geometries is shown in Fig. 50 (a). In this variation, the solid metal rectangle was removed from the center of the ringed patch. All other parameters were held constant. Fig. 50 (b) shows the magnitude of the return loss resulting from this simulation in solid red, along with the magnitude of the return loss from the complete ringed patch in dashed blue, for comparison. As shown, the effect on the return loss of removing the inner patch is minimal. The frequency of the highest resonance is the only feature that is significantly affected, likely because it is at this resonance that the fields shown in Fig. 47 were concentrated nearest the inner patch. The four resonant frequencies observed from this simulation are 353 MHz, 389.5 MHz, 413.5 MHz, and 437 MHz. Fig. 50 (c) shows the radiation pattern at 353 MHz, with the solid red trace indicating the directivity on the $\phi = 0°$ plane and the dotted blue trace indicating the directivity on the $\phi = 90°$ plane. The directivity at $\theta = 0°$ in this case is shown to be 5.92 dB. Similarly, Fig. 50 (d), (e), and (f) show the radiation patterns simulated at the other three resonant frequencies. These simulations show the directivity of the antenna at $\theta = 0°$ to be 4.04 dB at 389.5 MHz,

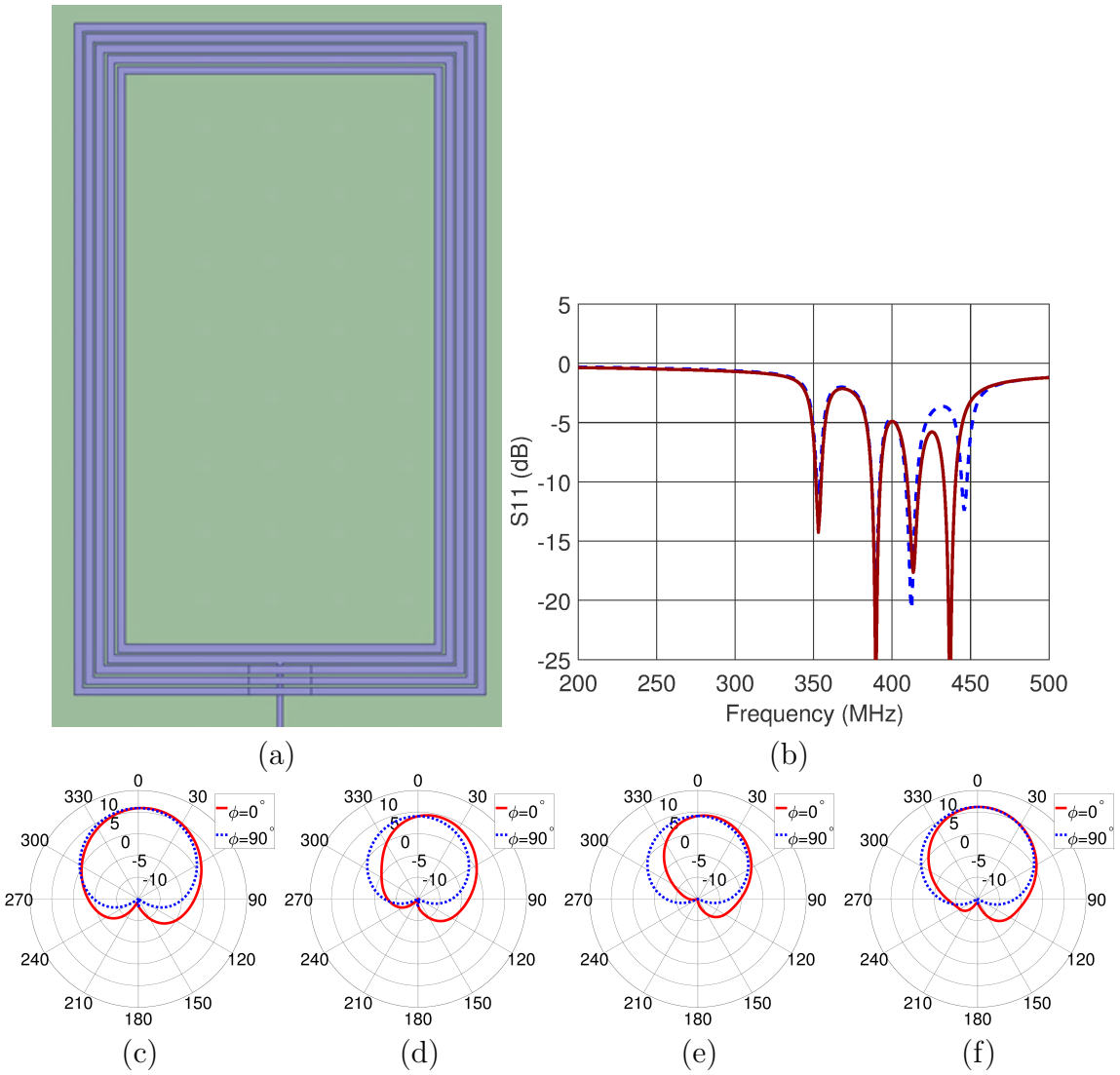

Figure 50: (a) The ringed patch with the inner patch removed, and (b) its return loss, shown in solid red. The return loss of the original ringed patch is shown in dashed blue, for comparison. The simulated directivity of the radiated field is shown at (c) 353 MHz, (d) 389.5 MHz, (e) 413.5 MHz, and (f) 437 MHz, with the directivity on the $\phi = 0°$ plane shown in solid red and the directivity on the $\phi = 90°$ plane shown in dotted blue.

4.10 dB at 413.5 MHz, and 6.19 dB at 437 MHz.

The second geometry variation to be explored was to remove both the inner patch and the innermost ring. Again, all other parameters were held constant. The new antenna resulting from this adjustment is shown in Fig. 51 (a). The return loss

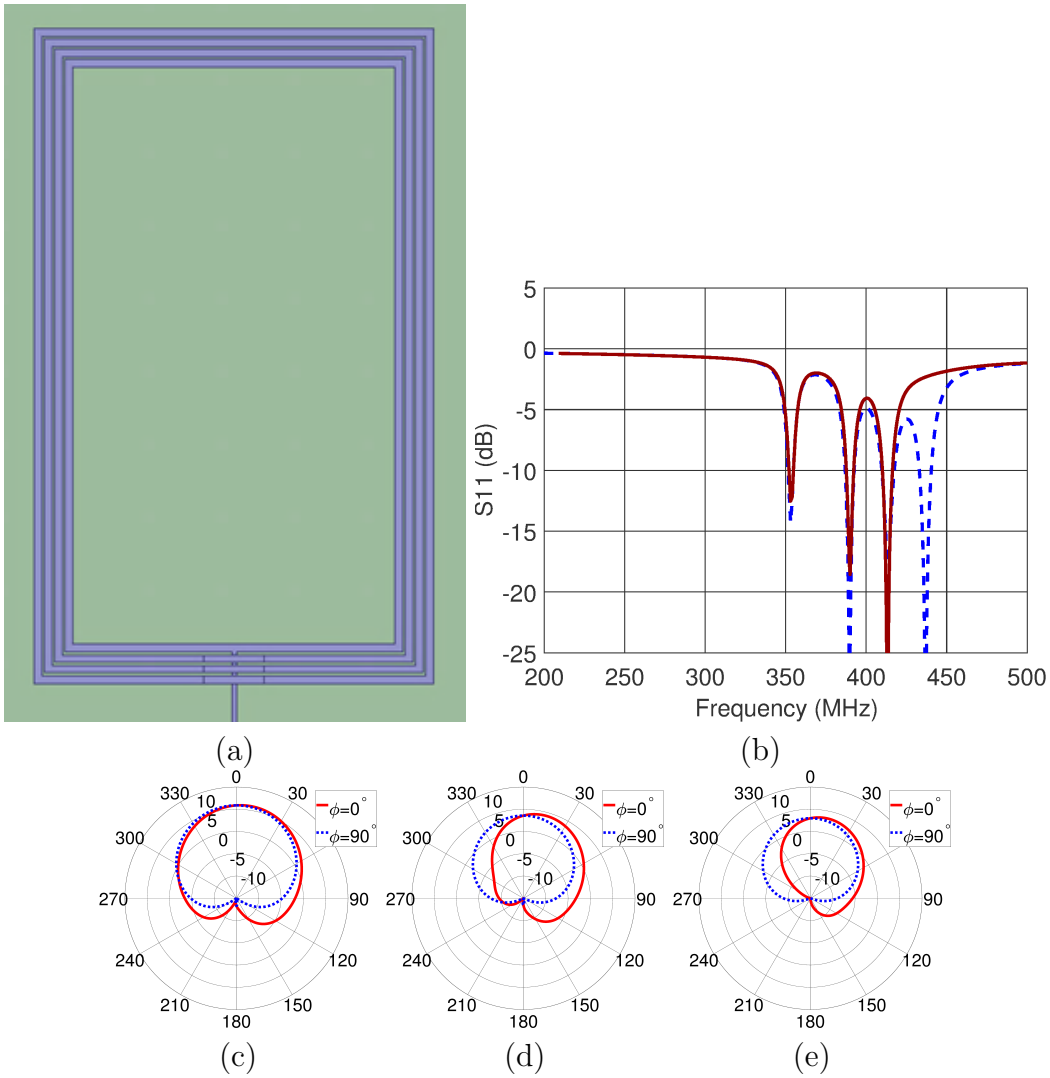

Figure 51: (a) The ringed patch with the innermost ring and patch removed, and (b) its return loss, shown in solid red. The return loss of the ringed patch without the center patch (as shown in Fig. 50) is shown in dashed blue, for comparison. The simulated directivity of the radiated field is shown at (c) 353 MHz, (d) 390 MHz, and (e) 413 MHz, with the directivity on the $\phi = 0°$ plane shown in solid red and the directivity on the $\phi = 90°$ plane shown in dotted blue.

resulting from this simulation is shown in Fig. 51 (b), in solid red. The return loss of the simulation of the five rings without the center patch (from Fig. 50) is also shown, in dashed blue. The only difference between these two simulations is the removal of the outermost ring. As can be seen from this graph, the result of removing the both the inner patch and the innermost ring is to completely eliminate the highest-frequency

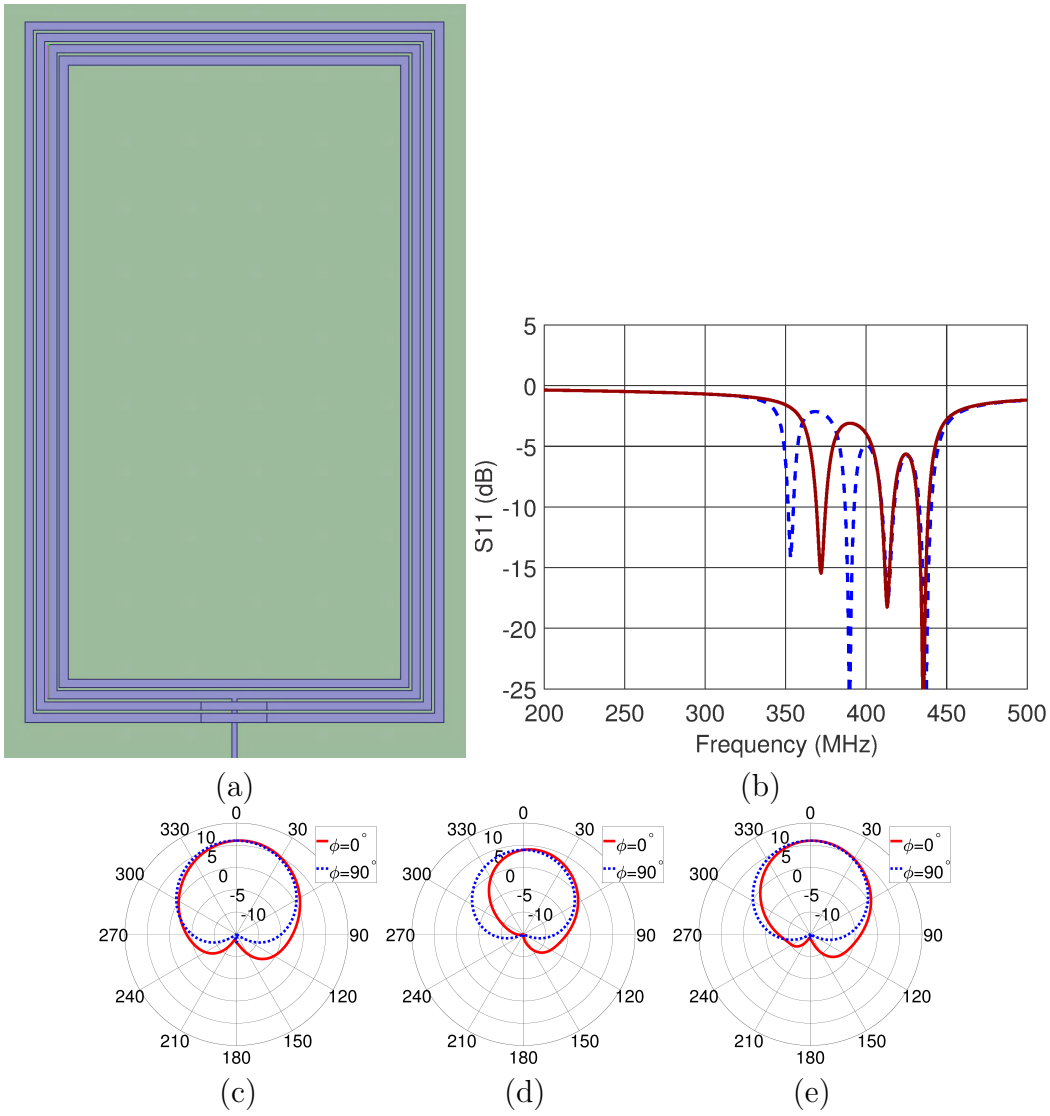

Figure 52: (a) The ringed patch with the outermost ring and patch removed, and (b) its return loss, shown in solid red. The return loss of the ringed patch without the center patch (as shown in Fig. 50) is shown in dashed blue, for comparison. The simulated directivity of the radiated field is shown at (c) 372 MHz, (d) 413 MHz, and (e) 435.5 MHz, with the directivity on the $\phi = 0°$ plane shown in solid red and the directivity on the $\phi = 90°$ plane shown in dotted blue.

resonance. The other three resonant frequencies remain approximately as they were, at 353 MHz, 390 MHz, and 413 MHz. This is consistent with the high interaction of the fifth ring with the field under the ring observed at the fourth resonance in Fig. 47. The directivities resulting from this simulation at each of the resonant frequencies

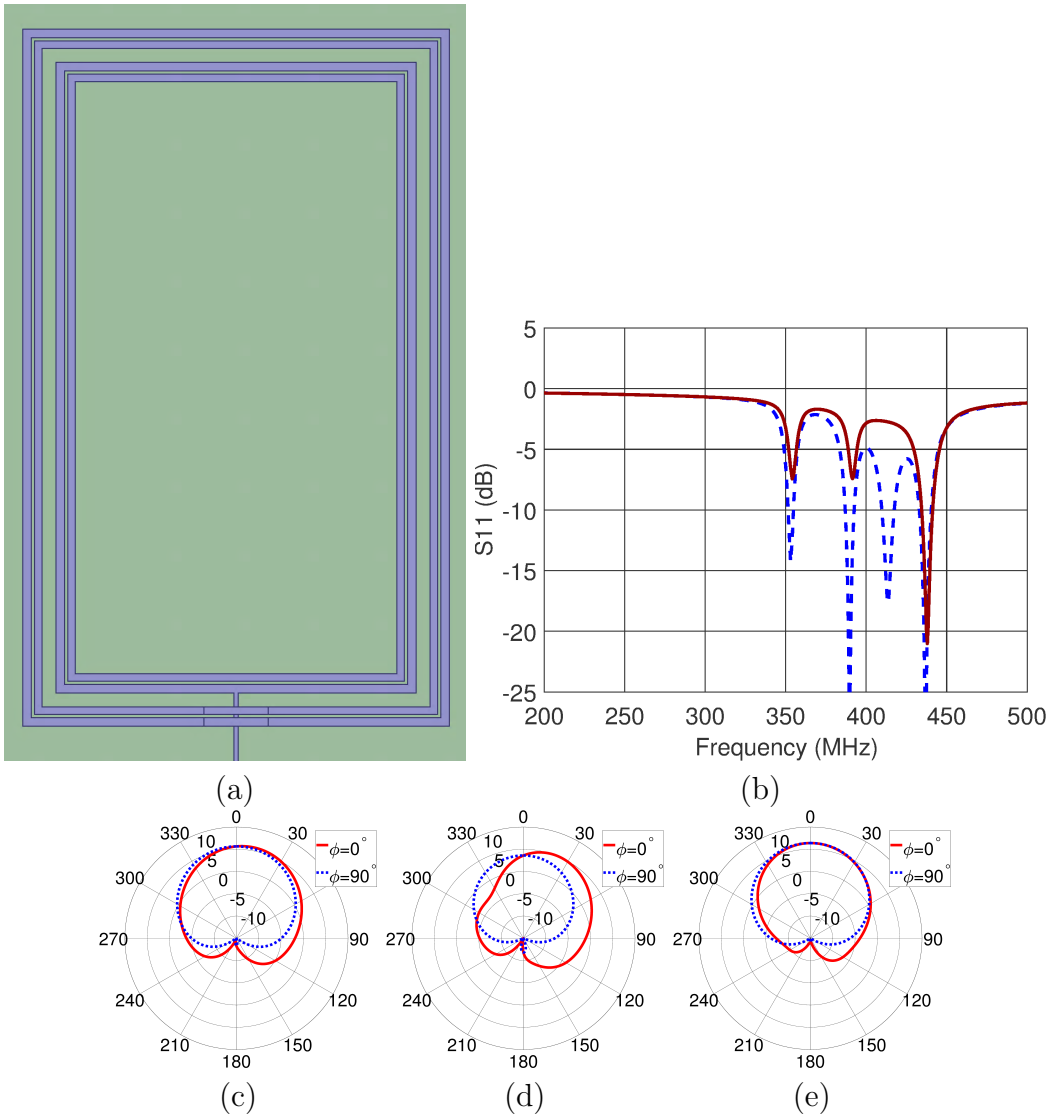

Figure 53: The ringed patch with the center patch and third ring removed, and its return loss, shown in solid red. The return loss of the five rings without the center patch, as shown in Fig. 50, is shown in dashed blue for comparison. The directivity of the antenna at (c) 354 MHz, (d) 391.5 MHz, and (e) 438 MHz is also shown, in dB, for the $\phi = 0°$ plane (shown in solid red) and the $\phi = 90°$ plane (shown in dotted blue).

are shown in Fig. 51 (c), (d), and (e). The directivity observed at $\theta = 0°$ is 5.87 dB at 353 MHz, 3.57 dB at 390 MHz, and 2.98 dB at 413 MHz.

A third geometry variation removed the center patch and outermost ring, as shown in Fig. 52 (a). Fig. 52 (b) shows the return loss resulting from this simulation in

solid red, along with the return loss from the simulation of the five rings without the center patch in dashed blue, for comparison. Again, the only difference between these two simulations is the removal of the outermost ring. As shown, the effect of this difference in geometry is firstly to eliminate the lowest frequency resonance, which is consistent with the high field concentration under the outermost ring at the lowest frequency of resonance, as shown in Fig. 47 (a). The removal of the outermost ring also caused the second-lowest resonance to shift down in frequency, likely because of the reduction in capacitance associated with coupling between the fourth and fifth rings.

In a fourth geometry variation, the center patch and third ring were removed from the complete ringed patch. This geometry is shown in Fig. 53 (a). The return loss observed in this simulation is shown in Fig. 53 (b) in solid red, with the return loss for the five rings without the center patch shown in dashed blue, for comparison. In this graph we see that removal of the third ring completely eliminates the third resonance. This result is consistent with the high field concentration under the third ring shown in Fig. 47 (c). The first and second resonances are also shown to shift slightly in frequency, and become decidedly weaker than in the case of the complete ringed rectangle. This can be attributed to the fact that the removal of the third ring decreased coupling between the directly-driven portion of the patch (the second ring) and the fourth and fifth rings, where the currents are concentrated for the first and second resonances. The three new resonant frequencies are 354 MHz, 391.5 MHz, and 438 MHz. The radiation pattern at each of these frequencies is shown in Fig. 53 (c), (d), and (e). The directivities at $\theta = 0^\circ$ are shown to be 5.64 dB, 3.60 dB,

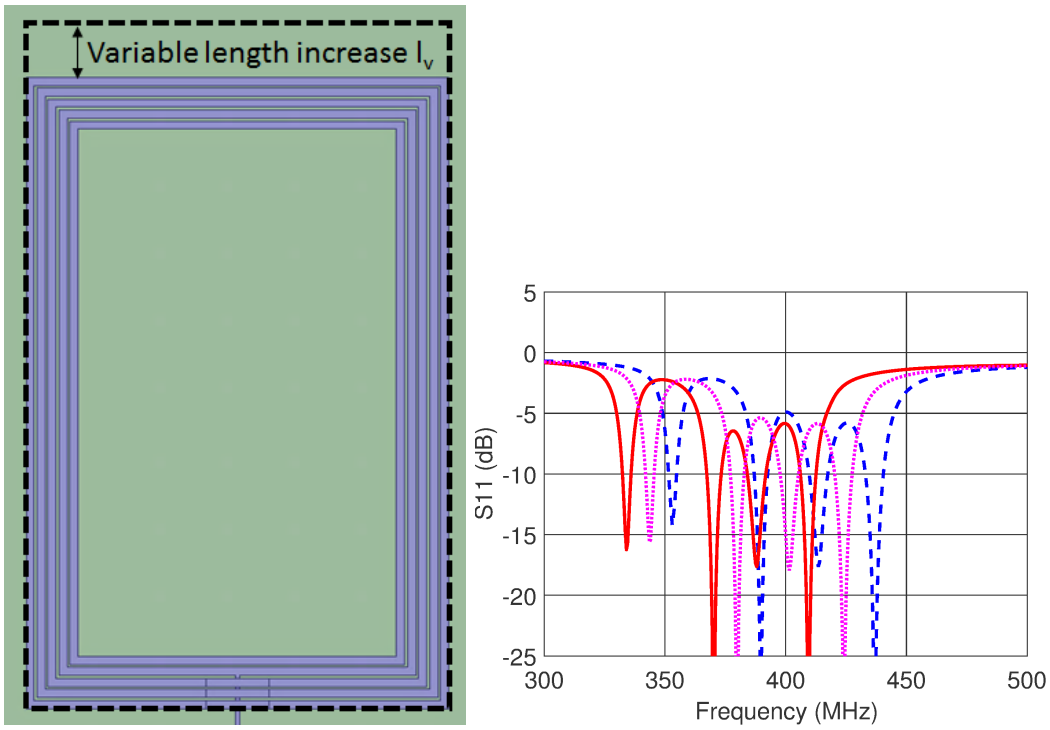

(a) (b)

Figure 54: The ringed rectangular patch antenna with the center patch removed, and total length increased by 12 mm (shown in solid red), 6 mm (shown in dotted magenta), and 0 mm (shown in dashed blue).

and 6.39 dB at the three resonances, listed from lowest frequency to highest.

These four simulations demonstrate two things. Firstly, they show that the center patch of the antenna has very little effect on the return loss and radiation pattern. Secondly, they show that the number of resonances is closely tied to the number of rings, though each ring cannot be separately correlated to a specific resonance (since there are five rings and only four resonances).

4.2.2 Length Variations

Next, the effect of removing the inner patch and increasing the overall length of the patch, as shown in Fig. 54 (a), was investigated. The return loss for this simulation

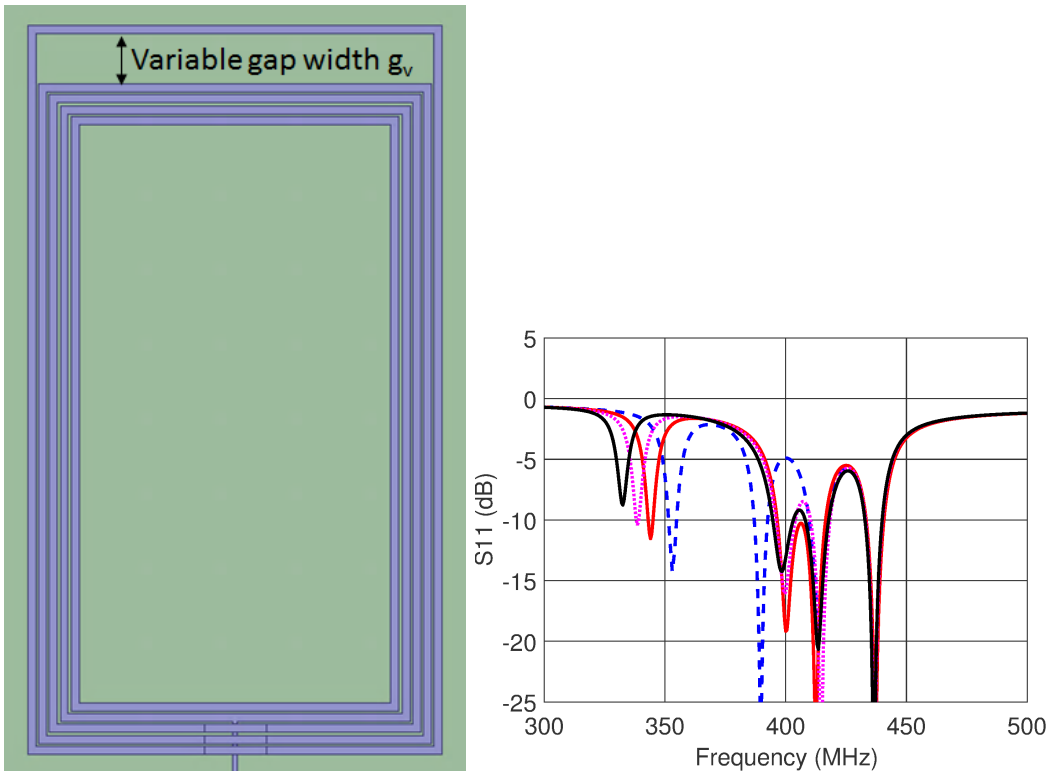

(a) (b)

Figure 55: The ringed patch with the outermost gap at the far end of the antenna from the feed increased. The return loss from this simulation is shown for four gap values: 3 mm (shown in solid red), 7 mm (shown in dotted magenta), and 11 mm (shown in solid black). The return loss for the original gap length of 0.6 mm is also shown, in dashed blue.

is shown in Fig. 54 (b). The solid red trace corresponds to the patch with its length increased by 12 mm; the dotted magenta trace corresponds to a 6 mm length increase, and the dashed blue trace is for the original patch length of 147.9 mm. As would be expected from a traditional patch, the effect of increased length is to shift all resonances to lower frequencies.

The effect of varying the length of the outermost ring by increasing the space between the fourth and fifth rings on the far end of the patch from the feed, as indicated in Fig. 55 (a), was also explored. The graph shown in Fig. 55 (b) shows

the return loss resulting from this set of simulations. The solid black trace shows |S11| for the case where the variable gap width g_v was increased to 11 mm. The dotted magenta trace corresponds $g_v = 7$ mm, the solid red trace to $g_v = 3$ mm, and the dashed blue trace to the original gap of 0.6 mm. As one would predict, the effect of increasing the length of the outermost ring is primarily to shift the lowest resonant frequency to lower frequencies. A less pronounced effect also observed, where increasing g_v increases the frequency of the second-lowest resonance. This is likely due to reduced capacitance between the fourth and fifth rings at the end furthest from the feed.

These two simulations demonstrate that increasing the length of the rectangle can be used to shift the resonant frequencies of the antenna. However, this involves increasing the physical size of the antenna. Since it appears that the length of the rings is the primary factor in determining resonant frequency, the following section will present a means of reducing the frequencies of operation without increasing the physical size of the antenna.

4.2.3 Variations on Antenna Shape

All the antenna variations presented thus far have maintained the overall rectangular antenna configuration. However, since it has been shown that removing the center rectangular patch had very little effect on the antenna response, the space can perhaps be better utilized using a different configuration.

Fig 56 (a) shows an example of another possible shape. In this case, the two long sides of the antenna have been altered so that the innermost ring overlaps itself in the

center. Fig. 56 (b) shows the return loss resulting from this simulation in solid red. The return loss from the case of the ringed rectangular patch without the center patch is also shown in dashed blue, for comparison. As shown, the increase in ring length introduced by this slight change in geometry resulted in a reduction in frequency of all

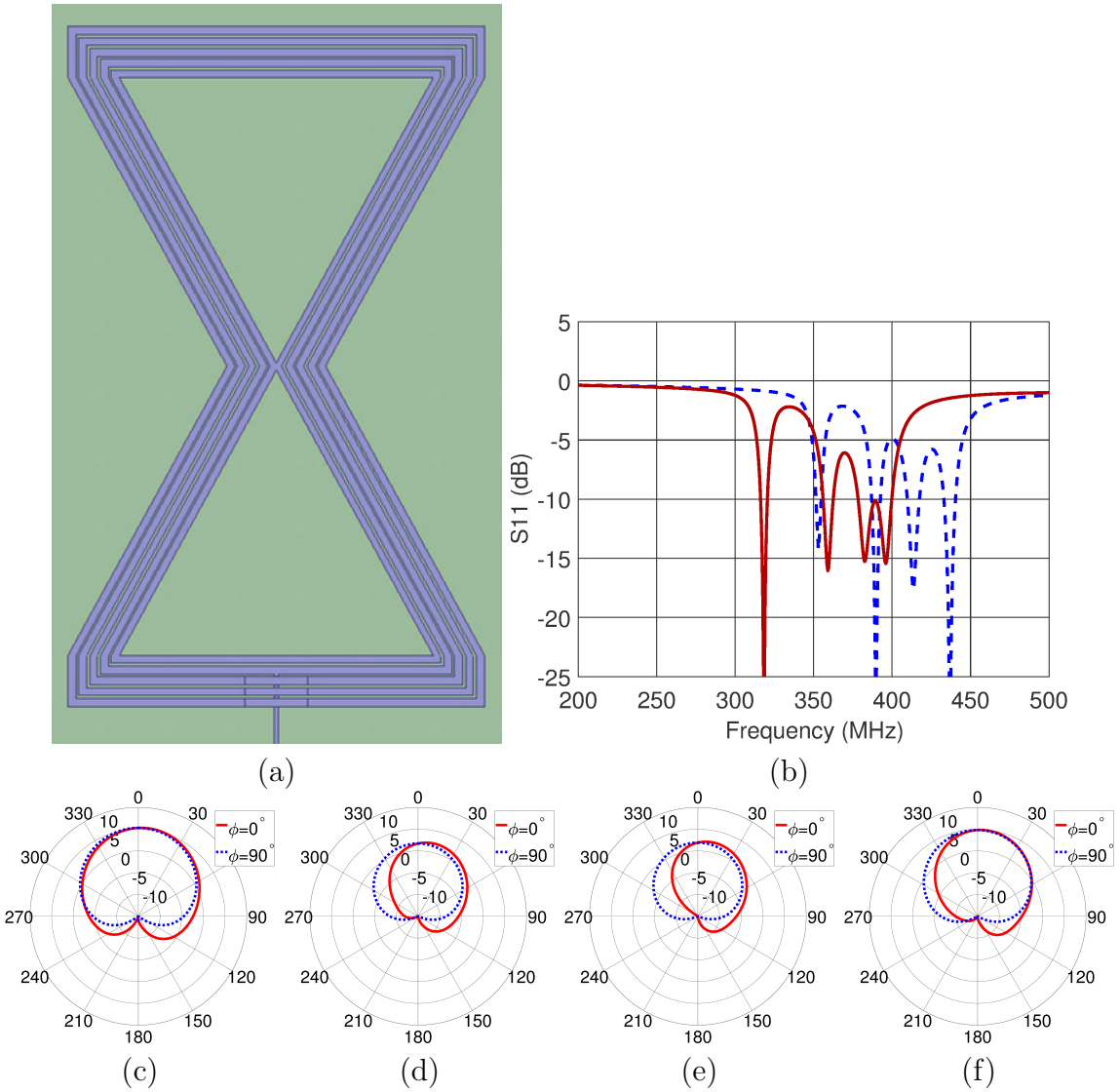

Figure 56: (a) A ringed bowtie patch antenna (b) the return loss obtained from its simulation, plotted in solid red, and the return loss for the ringed rectangular patch antenna with the center patch removed, plotted in dashed blue. The directivity of the antenna is also shown on the $\phi = 0$ (solid red) and $\phi = 90$ (dotted blue) planes, at (c) 318.5 MHz, (d) 359 MHz, (e) 382.5 MHz, and (f) 396 MHz.

four resonances. The lowest frequency of operation, which in the original rectangular patch antenna simulation was 353 MHz, is here shown to be 318.5 MHz. Similarly, the second resonance shifted from 389.5 MHz to 359 MHz. The third resonance shifted from 412.5 MHz to 382.5 MHz, and the fourth and highest-frequency resonance shifted from 446 MHz to 396 MHz. The directivity is shown for each resonant frequency, with a broadside directivity of 5.28 dB at 318.5 MHz shown in Fig. 56 (c), 1.71 dB at 359 MHz shown in Fig. 56 (d), 1.90 dB at 382.5 MHz shown in Fig. 56 (e), and 4.80 dB at 396 MHz shown in Fig. 56 (f).

Another possible geometry variation is shown in Fig. 57 (a). A 50 mm section in the center of each side of this rectangle was shifted inward by 30 mm, in a manner reminiscent of a Koch fractal. The return loss associated with this simulation is shown in Fig. 57 (b). As shown, the effect of this variation is to significantly reduce all four of the resonant frequencies of the antenna. The four new frequencies are 237.5 MHz, 257 MHz, 267.5 MHz, and 275 MHz. The directivity in dB for each of these frequencies is shown in Fig. 57 (c-f), where the directivity at $\theta = 0^\circ$ is shown to be 5.00 dB at 237.5 MHz, 0.06 dB at 257 MHz, 0.76 dB at 267.5 MHz, and 2.82 dB at 275 MHz. The dramatic reduction in directivity compared to previous simulations is probably due to the fact that the antenna is quite electrically small at these frequencies - the length of the antenna at 237.5 MHz is $\lambda_0/8.54$.

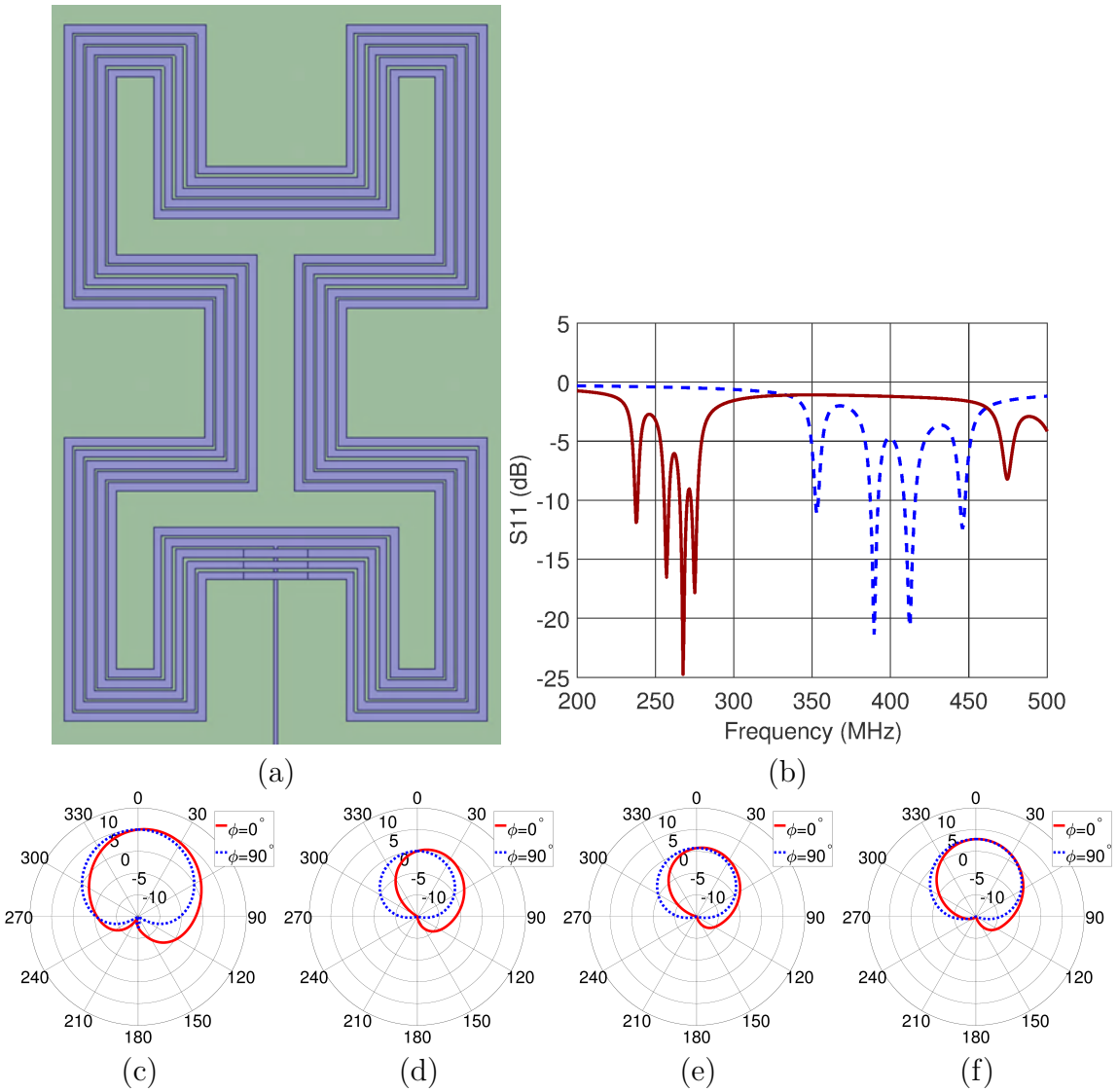

Figure 57: A fractal ringed patch antenna and its return loss. The return loss of the original ringed patch is shown in dashed blue, for comparison. The directivity of the antenna is also shown on the $\phi = 0$ (solid red) and $\phi = 90$ (dotted blue) planes, at (c) 237.5 MHz, (d) 257 MHz, (e) 267.5 MHz, and (f) 275 MHz.

4.3 Fabrication and Measurement of Ringed Patch Antenna

The ringed rectangular patch antenna was milled out on a 1/16" FR-4 printed circuit board. Thru, reflect, and line standards were also fabricated, to allow calibration to approximately 10 mm from the patch. The calibration also included an edge-mount SMA connector transition to a 50 Ω cable. The raised portions of the three outer

rings were accomplished using jumpers of insulated wire, soldered on either side of the feed line. The fabricated antenna is shown in Fig. 58 (a). The measured return loss from this antenna, after calibration, is shown in Fig. 58 (b) in solid red. The simulated return loss is also plotted, in dashed blue. As shown, the fabricated resonances were higher in frequency than the simulated resonances. The four resonances shown in Fig. 58 (b) occur at 363.6 MHz, 416.3 MHz, 454.9 MHz, and 481.1 MHz. The frequency shift is likely due to variation in the FR-4 dielectric constant from the $\epsilon_r = 4.4$ that was assumed in simulation.

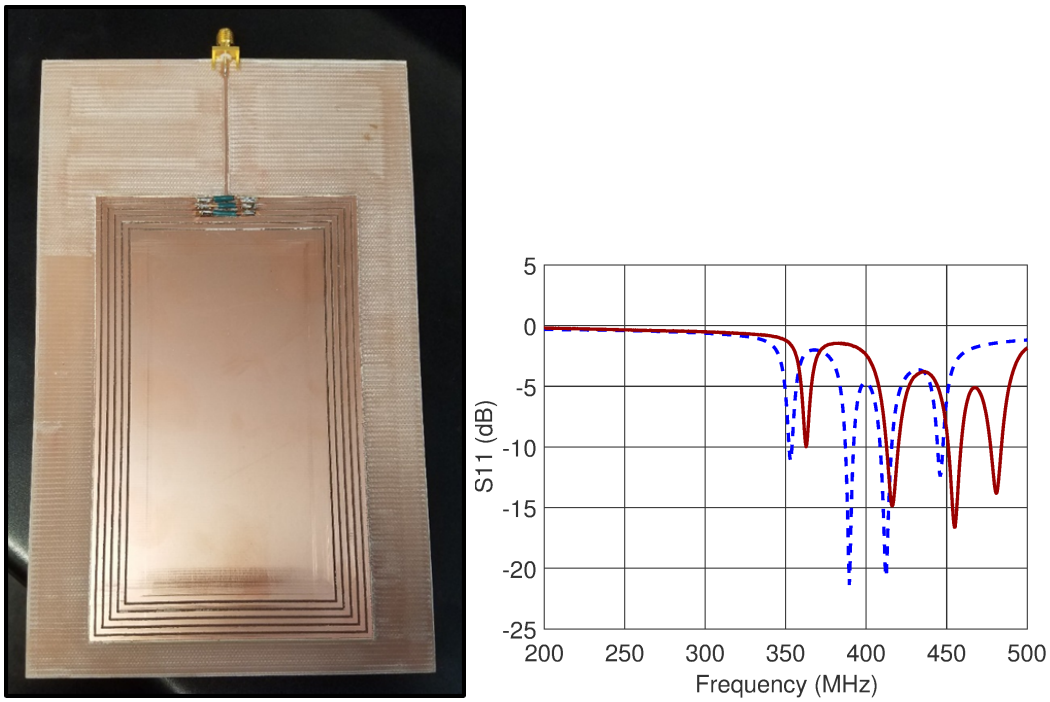

(a) (b)

Figure 58: The fabricated ringed rectangular patch antenna and its measured return loss, shown in solid red. The return loss from the simulation of this antenna is also shown, in dashed blue.

4.4 Chapter Summary

A ringed rectangular patch antenna was presented, and was shown to possess four frequencies of operation. Each of these four frequencies was below the natural resonance of the patch antenna. The fields in the vicinity of the patch and the far field radiation pattern of the ringed rectangular patch antenna were presented at each of the four resonant frequencies, and shown to qualitatively match those of a traditional microstrip patch antenna. The measured return loss of the fabricated antenna was presented, and was consistent with simulated results, except for a shift in frequencies. Four variants of the antenna were presented involving removing various elements of the geometry. The first of these removed the center patch of the antenna, which was shown to have very little effect on the return loss and radiation pattern. The second removed the center patch and the first ring, which resulted in elimination of the highest-frequency resonance. The third removed the center patch and the fifth ring, which resulted in elimination of the lowest-frequency resonance and a shift of the second-lowest-frequency resonance to lower frequencies. The fourth simulation removed the center patch and the third ring, which was shown to result in elimination of the second-highest resonance. Next, two variants of the antenna involving lengthening various rings was presented. It was demonstrated that increasing the length of all rings together shifted all the resonant frequencies down together, while increasing the length of only the outermost ring shifted only the lowest-frequency resonance, and, to a lesser extent, the second-lowest-frequency resonance. Finally, two variations on the overall rectangular shape of the antenna were explored. The first of these involved

pulling in the two long sides of the antenna so that they met in the center of the patch. The effect of this adjustment was to shift the resonant frequencies down slightly from the unperturbed antenna. The second variation involved pulling in a 50 mm long center section of each of the four sides of the antenna by 30 mm. This significantly reduced all four resonant frequencies, but also dramatically reduced the directivity seen at those four resonances. In conclusion, this ringed rectangular antenna has been shown to have multiband behavior with controllable frequencies of operation. The antenna is electrically small, and has a radiation pattern approximately matching that of a traditional patch antenna.

CHAPTER 5: A CIRCULARLY-POLARIZED HORN ANTENNA WITH TUNABLE HANDEDNESS USING CHIRAL METAMATERIAL LOADING

Horn antennas have high directivity and are easy to feed using rectangular waveguides. However, they are limited in their application by the fact that they typically are capable of handling only linearly polarized waves. Metamaterial loading has shown promise in helping to overcome this limitation, as discussed in Chapter 2. However, previously published results often involve greatly increasing the size of the antenna [99] and also present fixed handedness for each frequency of operation [100]. This chapter will present a modified horn antenna that utilizes a unique chiral metamaterial, located inside the mouth of the horn, to achieve circular polarization with minimal added bulk. Unlike previous designs, this work offers a range of frequencies over which the polarization of the radiated wave may be adapted to the application at hand through simple reorientation of the loading metamaterial unit cells.

5.1 Geometry and Simulation of Metamaterial-Loaded Antenna

This circularly polarized horn antenna utilizes a two-step process to achieve circularly polarized radiation. The first step is to transition the electric field fed into the antenna from the rectangular waveguide into a square-cross-section horn, in which the electric field is directed along the diagonal of the square waveguide. This step is achieved through modification of the traditional horn antenna geometry. The second step is to introduce a 90° phase difference between two orthogonal components of

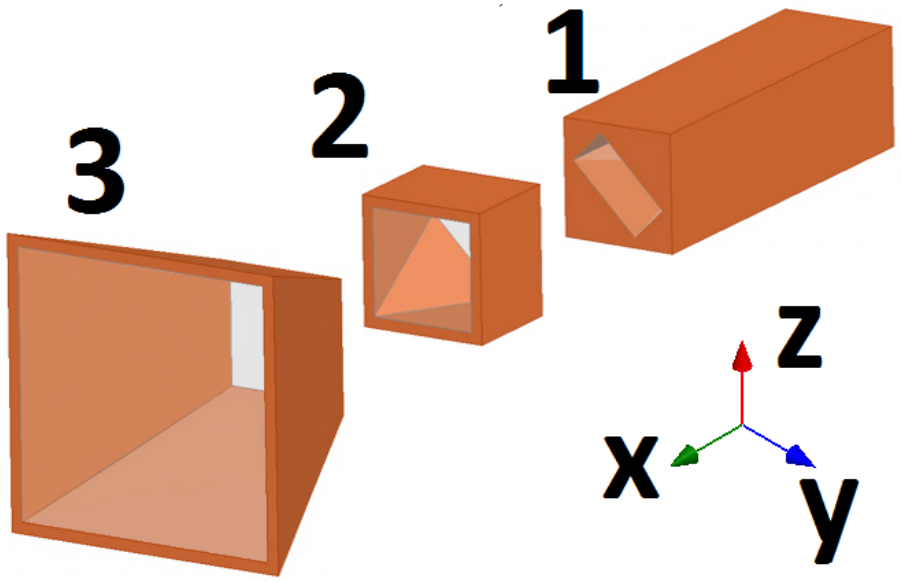

Figure 59: The modified horn antenna, with Part 1: the rectangular waveguide segment, Part 2: the rectangular-to-square waveguide transition segment, and Part 3: the square flared horn segment.

the electric field. This step is achieved through metamaterial loading located in the mouth of the horn.

A typical horn antenna consists of two elements - a rectangular waveguide section, and a flared horn section. In order to achieve the desired electric field orientation in the flare section, the modified horn antenna adds a third section in the center, as shown in Fig. 59. This "transition section" between the waveguide and the horn flare linearly transitions the waveguide cross-section from the WR-187 rectangle of the first segment to a square cross-section offset from the rectangle by 45° around the direction of propagation, as shown in Fig. 59. This technique for electric field re-orientation was originally presented in [99]. The length of this transition section is 50 mm. This is followed by a square-cross-section flared horn having initial width and height equal to 49.3 mm, and final width and height equal to 120 mm. The flare has

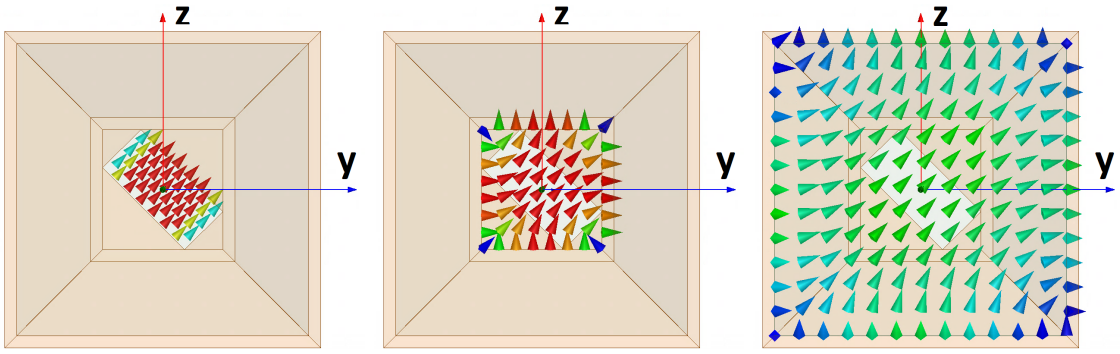

(a) (b) (b)

Figure 60: The electric field in the antenna, given 3.26 GHz excitation, taken on a plane normal to the x-axis (a) at the beginning of the rectangular waveguide section (segment 1), (b) just after the transition section, at the beginning of the square horn flare (between segments 2 and 3), and (c) at the radiating aperture of the horn flare (at the end of segment 3).

an x-dimension of 100 mm. Conceptually speaking, the goal of this added transition section is to split the electric field into two equal-magnitude, in-phase linear modes, directed along the sides of the square.

The electric field in the guide on three significant planes along the length of the unloaded antenna, viewed from the +x direction and given a 3.26 GHz excitation, are shown in Fig. 60. Figure 60 (a) shows the vector E-field at the beginning of the waveguide. This figure shows the expected field configuration for the TE_{10} mode, where the electric field is oriented parallel to the shorter sides of the rectangular waveguide. Figure 60 (b) shows the vector E-field just after the transition section (at the junction of sections 2 and 3). This figure demonstrates that the orientation of the field is largely preserved through the transition segment, though the shape of the guiding structure transitioned from rectangular to square. Figure 60 (c) shows the vector E-field at the radiating aperture of the flared horn. This figure shows that the electric field maintains the diagonal orientation to the end of the horn.

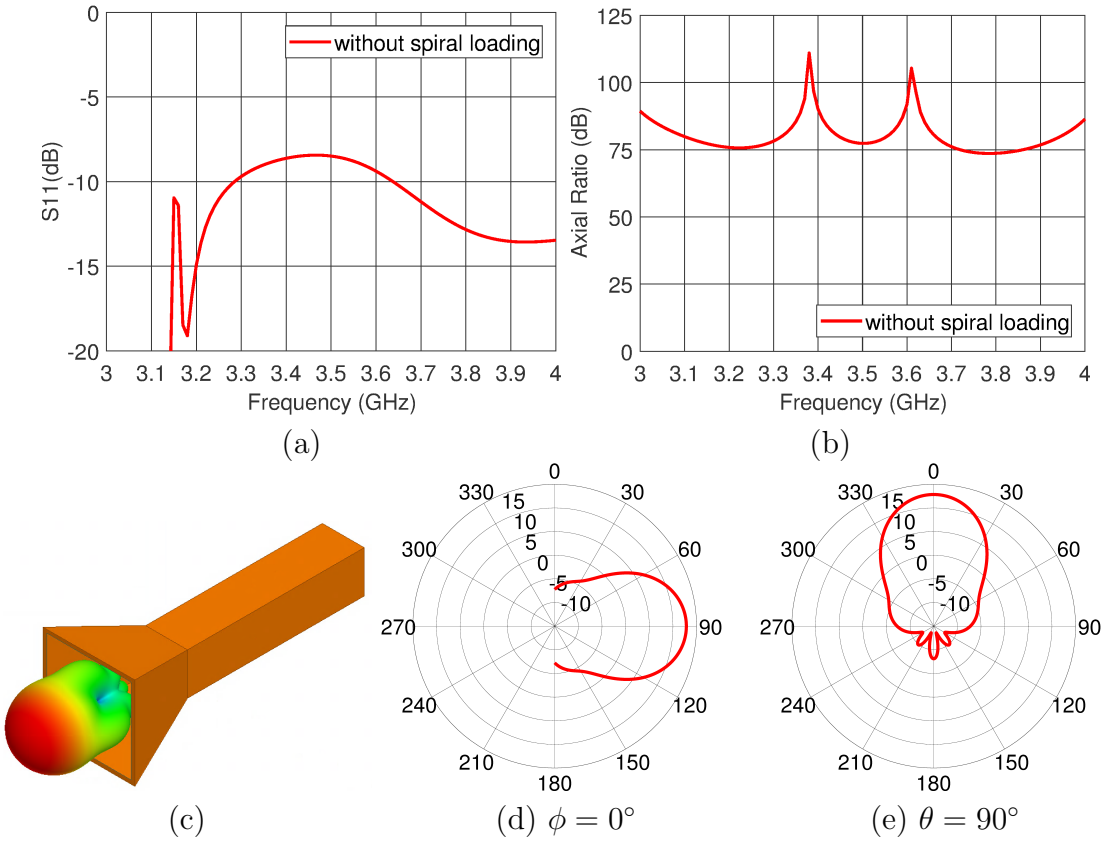

Figure 61: (a) Broadside |S11| in dB, (b) Broadside axial ratio in dB, and (c) 3D polar gain plot for the modified horn antenna in the absence of metamaterial loading, (d) Gain on the $\phi = 0°$ plane, and (e) Gain on the $\theta = 90°$ plane at 3.26 GHz.

Figure 61 (a) shows the magnitude of return loss and Fig. 61 (b) the axial ratio for the modified horn antenna in the absence of metamaterial loading. As shown, the return loss is not optimized for this unloaded antenna; the match is only good from cutoff at 3.15 GHz to 3.29 GHz, and above 3.64 GHz. At 3.26 GHz, |S11| is observed to be -10.68 dB. The axial ratio shown in Fig. 61 (b) is upwards of 70 dB across the presented spectrum, and at 3.26 GHz is reported as 76.17 dB. This indicates a very clean linear polarization for the radiated wave across the relevant frequency band. Thus, in the absence of metamaterial loading, these simulation results demonstrate that the horn antenna radiates a linearly polarized wave, with

the electric field oriented along the diagonal of the square horn. The 3D gain plot of this antenna at 3.26 GHz is shown in Fig. 61 (c), and shows a maximum gain of 12.8 dB at $\phi = 0°$, $\theta = 90°$.

The next step in achieving circular polarization is to introduce a phase differential between the z-directed and y-directed components of this linearly polarized electric field. The metamaterial unit cells used to achieve this phase differential are based on the spherical spirals presented in Chapter 3, but are cylindrical, rather than spherical. They are each formed as a three-turn left-handed spiral with respect to $+\vec{z}$, as shown in Fig. 62. They have a radius of 23 mm, a height of 14.4 mm, and are formed of wire having a radius of 0.5 mm. Four of these unit cells were arranged in the mouth of the horn, as shown in Fig. 63. They were centered at (-20 mm, ±25.3 mm, ±23.5 mm), with respect to the center of the antenna aperture. The unit cells shown in Figs. 63 (a) and 63 (b) are in what we will call "orientation A". Polarization adaptability is achieved by rotating each metamaterial on its own x-axis by 90°, as shown in Fig. 63 (c). This orientation we will call "orientation B".

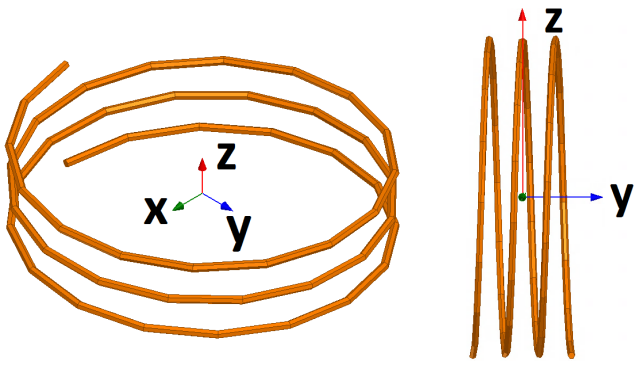

(a) (b)

Figure 62: A single unit of the metamaterial used to load the circularly polarized horn antenna (a) in Orientation A, and (b) in Orientation B.

Figure 64 shows the return loss and broadside axial ratio resulting from the simulation of the metamaterial-loaded horn antenna in HFSS. In each of these cases, the value for the unit cells in orientation A is plotted in solid red, and the value for the unit cells in orientation B is plotted in dashed black. Fig. 64 (a) shows |S11| in dB for each of these simulations. Again, the waveguide cutoff can be observed in this plot at 3.15 GHz. This plot also shows that the antenna is matched for both orientations of the unit cells from 3.25 GHz to 3.35 GHz, and also from 3.68 GHz to 3.93 GHz. Figure 64 (b) shows the axial ratio for the two orientations in dB, measured exactly

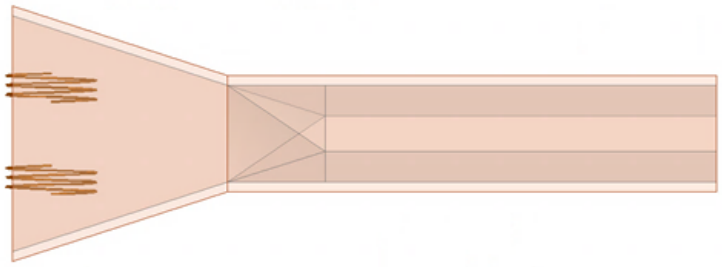

(a) Orientation A, viewed from +y

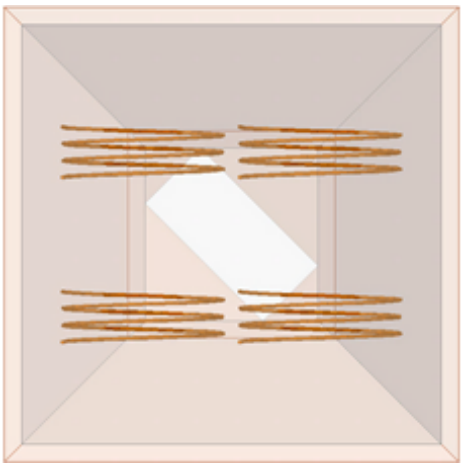

(b) Orientation A, viewed from +x

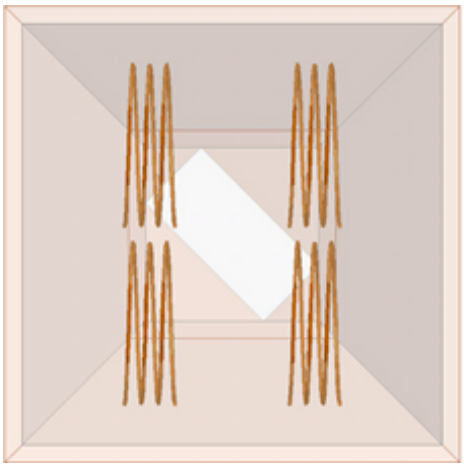

(c) Orientation B, viewed from +x

Figure 63: The modified horn antenna with metamaterial loading (a) viewed from the +y direction, with unit cells in orientation A, (b) viewed from the +x direction, with unit cells in orientation B, and (c) viewed from the +x direction, with unit cells in orientation B.

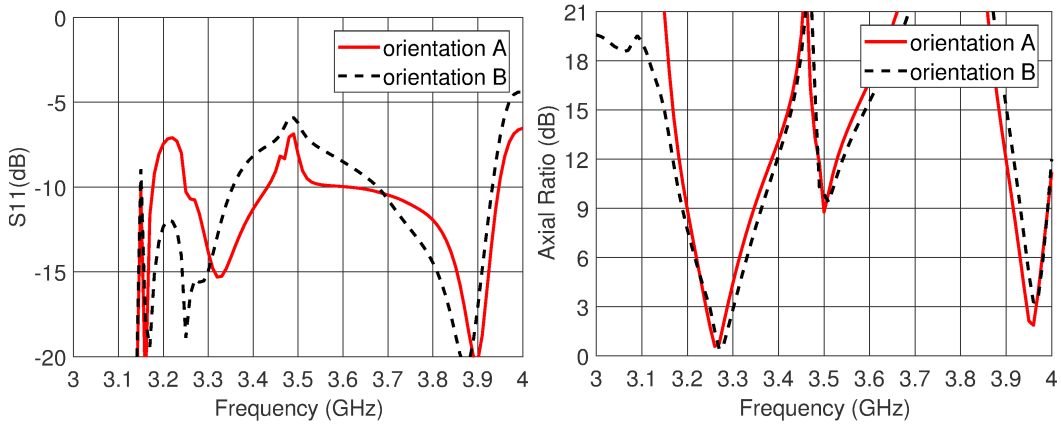

(a) (b)

Figure 64: (a) |S11| in dB, (b) Axial ratio in dB, taken at $\phi = 0°$, $\theta = 90°$. In each plot, the case where the unit cells are in orientation A is plotted in solid red, and the case where the unit cells are turned to orientation B is shown in dashed black.

broadside from the horn, at $\theta = 90°$, $\phi = 0°$. Axial ratio is under 3 dB, indicating that the radiated wave is circularly polarized, from 3.25 GHz to 3.29 GHz for both simulations. A minimum axial ratio is observed for both orientations at 3.26 GHz, where loading with the unit cells in orientation A results in an axial ratio of 0.56 dB and loading with the unit cells in orientation B results in an axial ratio of 1.50 dB.

The far field radiation pattern at 3.26 GHz is shown in Fig. 65. Figure 65 (a) shows the gain of the left-hand circularly polarized (LHCP) wave in solid red and the gain of the right-hand circularly polarized (RHCP) wave in dotted blue, for a sweep of θ where ϕ is held constant at 0°, and where the metamaterial unit cells are in orientation A. The radiation in this case is clearly RHCP, and has a gain of 11.4 dB at broadside, while the cross-polarization has a gain of -18.4 dB. Figure 65 (b) shows exactly the same plot for the case where the unit cells are in orientation B. In this case, the radiation is clearly LHCP, with broadside gain of the LHCP wave at 11.5 dB, while the gain of the right-hand circularly polarized component is -9.8 dB. Figures

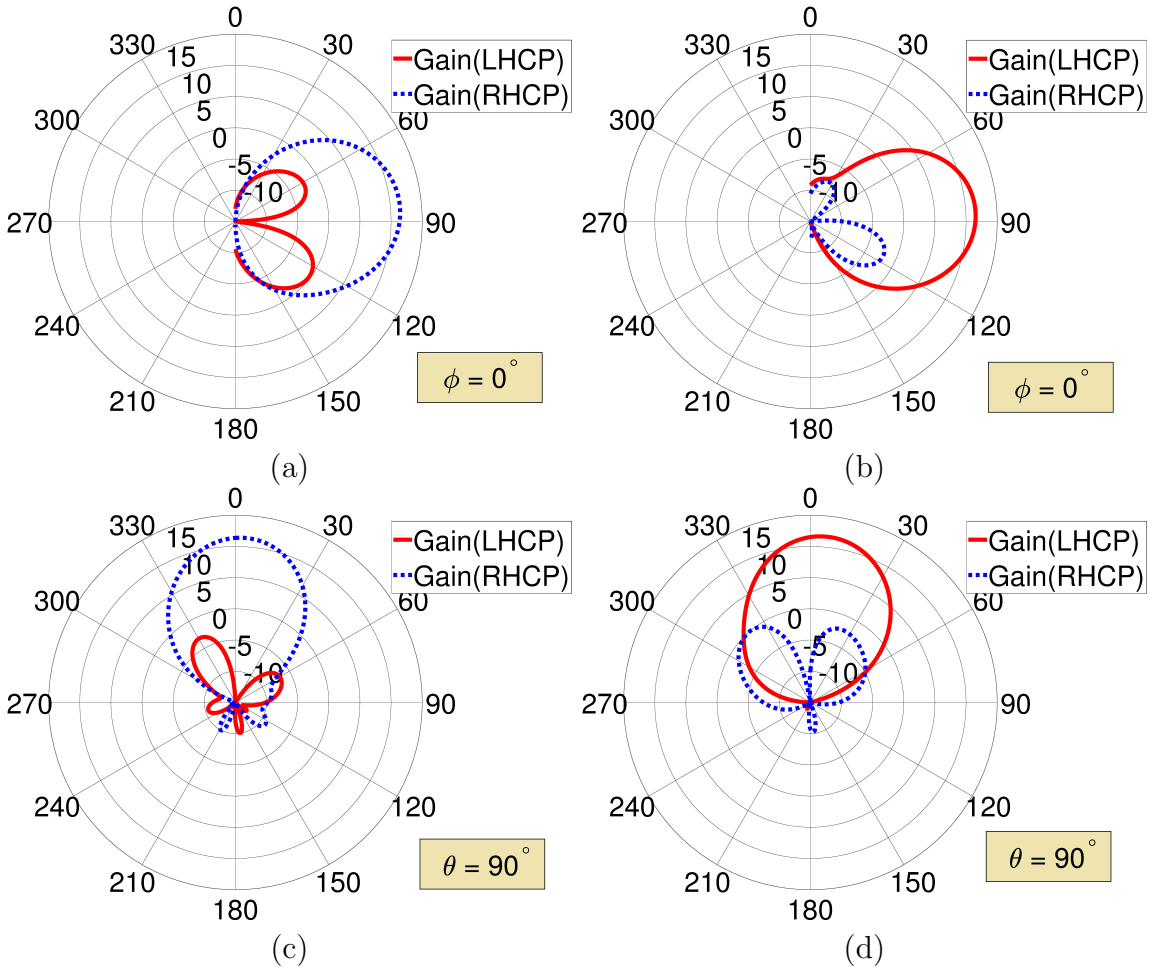

Figure 65: Gain at 3.26 GHz of the RHCP wave component, shown in dotted blue, and of the LHCP wave component, shown in solid red, for the case where (a) the unit cells are in orientation A, with $\phi = 0°$. (b) the unit cells are in orientation B, with $\phi = 0°$. (c) the unit cells are in orientation A, with $\theta = 90°$. (d) the unit cells are in orientation B, with $\theta = 90°$.

65 (c) and 65 (d) show the corresponding sweeps of θ for ϕ held constant at 90°.

Finally, the 3D polar plots of the total gain for this spiral-loaded antenna for each of the two orientations is shown in Fig. 66. For orientation A, the total broadside gain is 11.7 dB, and for orientation B, the total broadside gain is 11.8 dB.

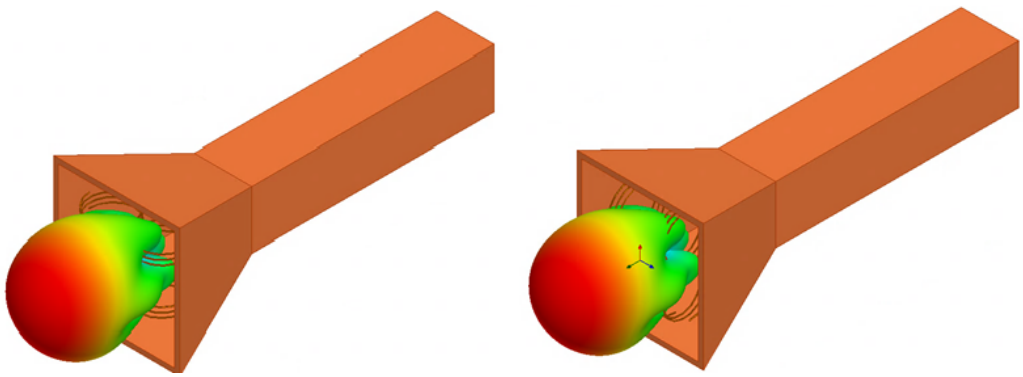

(a) (b)

Figure 66: 3D polar gain plot for the modified metamaterial-loaded horn antenna with the loading unit cells (a) in orientation A and (b) in orientation B.

5.2 Fabrication Considerations

To build this antenna, three unique components must be addressed - fabrication of the modified horn with the transition section, fabrication of the metamaterial unit cells, and appropriate positioning of said unit cells in the mouth of the horn. One possible technique for fabricating the waveguide length, transition section, and flared horn is to cut out and fold appropriately dimensioned pieces of sheet copper, then solder them together. The specifications for such two-dimensional cut-and-fold pieces are shown in Fig. 67. Two of each of these pieces would be required to fabricate a complete modified horn. In this design, every interior line indicates a fold, and the exterior lines indicate the shape to be cut out. When assembled, the yellow polygons would be sides of the flared horn, the blue polygons sides of the transition section, and the purple polygons sides of the rectangular waveguide section. The greyed-out tabs on the exterior sides of each piece are to be used for establishing secure structural and electrical connections at the edges of the horn and at the feed point of the antenna.

For fabrication of the metamaterial unit cells and positioning of the unit cells

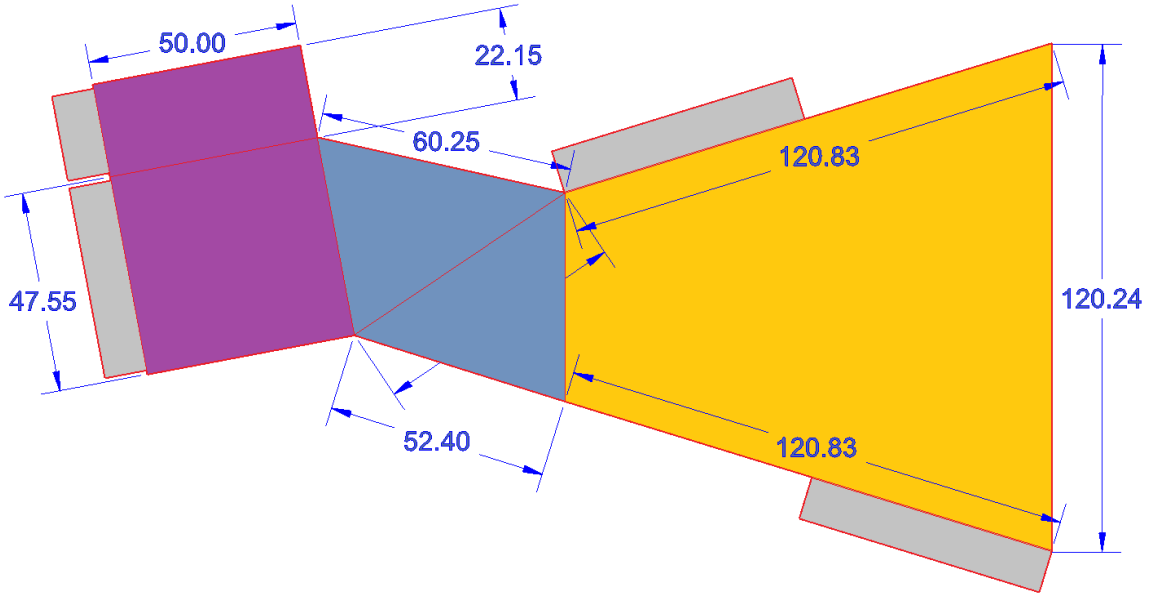

(a)

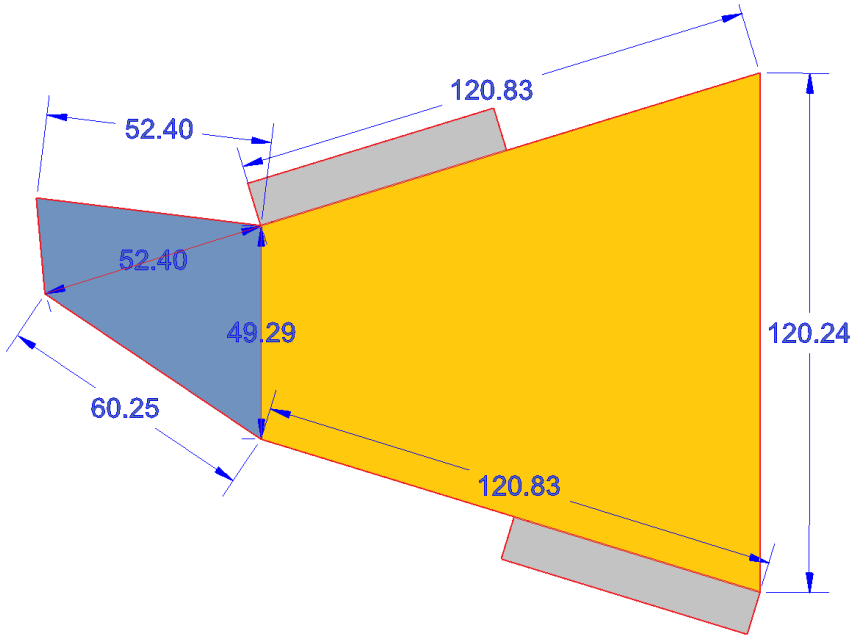

(b)

Figure 67: Two-dimensional sheets that could be used to fabricate the modified horn antenna. The flared horn sides are shown in yellow, the transition section sides in blue, and the rectangular waveguide sides in purple. A complete kit would require two of each of these pieces.

in the mouth of the modified horn antenna, a 3D printed support structure may be considered. A proposed 3D printable structure composed of hollow dielectric cylinders

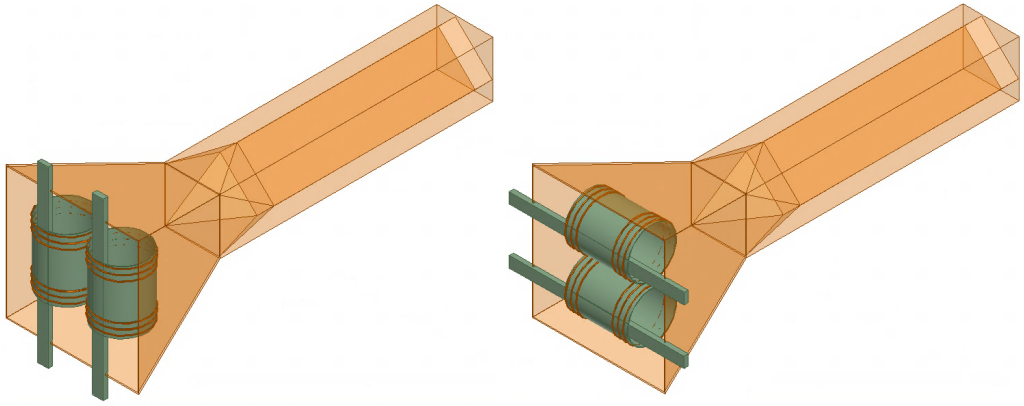

(a) (b)

Figure 68: The metamaterial-loaded horn antenna with 3D-printable supports (a) in orientation A and (b) in orientation B.

for metamaterial support and dielectric posts for positioning is shown in Fig. 68. The effect of adding these dielectric supports was investigated through simulation in HFSS, where the thickness of the hollow cylinders was set to 0.5 mm, the posts were designed to be 10 mm wide and 4 mm thick, and the dielectric constant of the support material was set to $\epsilon_r = 3$.

Preliminary simulations showed that this dielectric loading shifted the operative bandwidth to significantly lower frequencies than the unloaded case. In order to

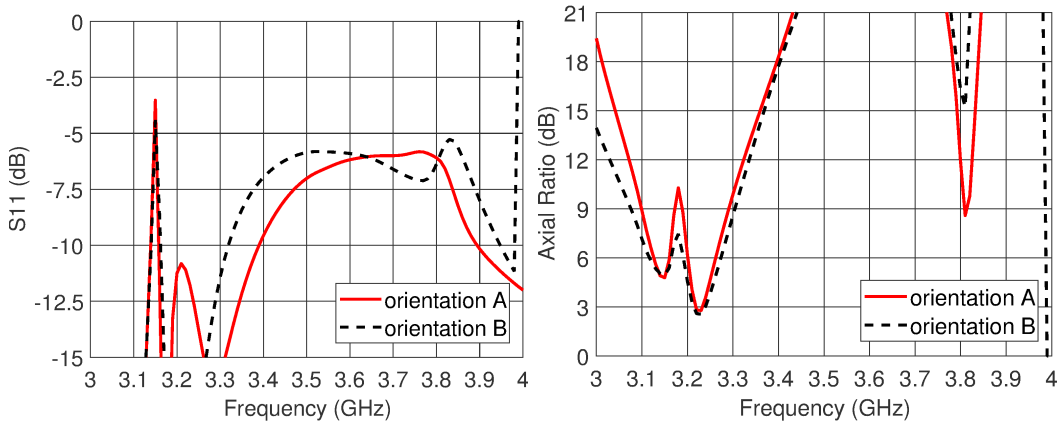

(a) (b)

Figure 69: The (a) return loss and (b) axial ratio for the metamaterial-loaded horn antenna with 3D-printable supports (a) in orientation A and (b) in orientation B.

maintain operation above the cutoff frequency of the waveguide, the number of spiral turns in each metamaterial unit cell was adjusted from 3 to 2.9. The return loss and axial ratio resulting from this simulation are shown in Fig. 69. For the simulation of the unit cells in orientation A, a return loss of -11.77 dB and axial ratio of 2.78 dB is reported at 3.23 GHz. The corresponding simulation of the unit cells in orientation B reports a return loss of -18.4 dB and an axial ratio of 2.55 dB at the same frequency.

The far field radiation pattern at 3.23 GHz for the case of the metamaterial-loaded

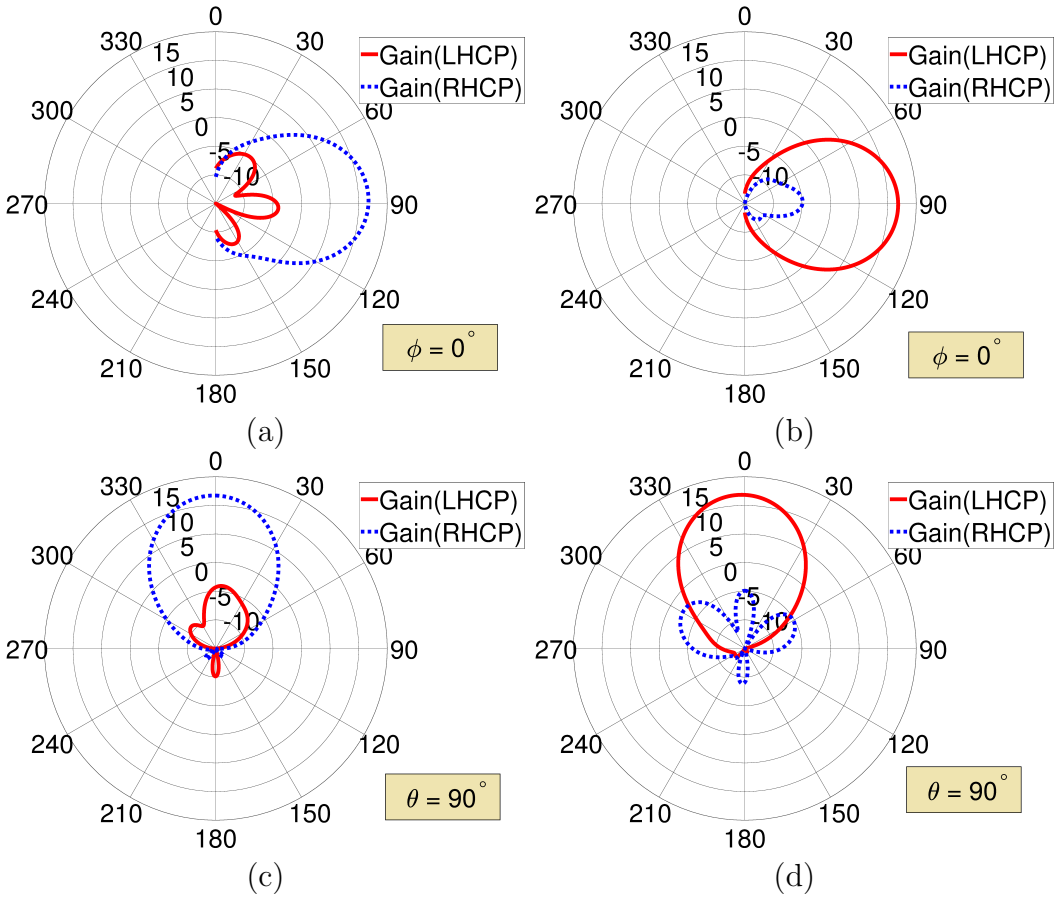

Figure 70: Gain at 3.23 GHz of the RHCP wave component, shown in dotted blue, and of the LHCP wave component, shown in solid red, for the case where (a) the unit cells are in orientation A, with $\phi = 0°$. (b) the unit cells are in orientation B, with $\phi = 0°$. (c) the unit cells are in orientation A, with $\theta = 90°$. (d) the unit cells are in orientation B, with $\theta = 90°$.

modified horn antenna with dielectric supports is shown in Fig. 70. Figure 70 (a) shows the gain of the LHCP wave in solid red and the gain of the RHCP wave in dotted blue, for a sweep of θ where ϕ is held constant at 0°, and where the metamaterial unit cells are in orientation A. As previously, the radiation in this case is shown to be RHCP, and has a gain of 11.7 dB at broadside, while the cross-polarization has a gain of −4.2 dB. Figure 70 (b) shows exactly the same plot for the case where the unit cells are in orientation B. In this case, the radiation is clearly LHCP, with broadside gain of the LHCP wave at 11.8 dB, while the gain of the right-hand circularly polarized component is −4.9 dB. Figures 70 (c) and 70 (d) show the corresponding sweeps of θ for ϕ held constant at 90°.

5.3 Chapter Summary

This chapter presented a rectangular waveguide horn antenna that utilizes chiral metamaterial loading to enable circularly polarized radiation. The handedness of the polarization over the range 3.25 GHz to 3.29 GHz is shown to be tunable from left-handed circular to right-handed circular by adjusting the orientation of the loading unit cells. In this frequency range, the gain of the co-polarized radiation is better than 11 dB for both the left-handed and right-handed configurations. The gain of the cross-polarized component of the radiated wave is more than 20 dB below the co-polarized gain in both cases.

The challenge of building this antenna was discussed in detail. Two-dimensional sheets that could be folded to form the modified horn antenna and 3D-printable dielectric supports for wire-wrapping and metamaterial positioning were presented.

The effect of the added dielectric was explored through simulation, and mitigated through minor adjustment of the unit cells. The return loss, axial ratio, and radiation pattern of the antenna including this dielectric loading were reported, and showed only minor performance degradation from the unloaded case.

CHAPTER 6: CONCLUSION

This dissertation began with a brief introduction to electromagnetic theory, covering wave generation and propagation, as well as wave material interaction. That was followed with a discussion of fractal geometries and their generation techniques. The use of fractals in antenna design was presented next, with relevant publications for fractal monopole antennas, fractal dipole antennas, and fractal patch antennas. Electromagnetic metamaterials were introduced, with a discussion of the history of and motivation for negative-material-parameter metamaterial engineering. Several unique properties of double-negative materials were demonstrated, including negative index of refraction, negative phase velocity, and the reversal of Snell's law. The use of fractals in electromagnetic metamaterial design was reviewed using relevant publications from the open literature. Finally, several publications utilizing metamaterial loading to enhance the radiation characteristics of horn antennas were presented.

The novel work presented in this dissertation began in Chapter 3, with the spherical spiral metamaterial unit cell. This unit cell, developed as a three-dimensional fractal expansion of the traditional split ring resonator, was shown in simulation to be capable of producing broadband negative permittivity over a bandwidth of 40.4% when oriented with the axis of the spiral aligned with the incident electric field. Negative permeability over a bandwidth of 35.4% was achievable by rotating the unit cells by 90° with respect to the incident electric field, and double-negative behavior

was observed over a bandwidth of 15.5% for the unit cells rotated by 45° with respect to the incident electric field. The mechanism by which these different responses were induced was discussed. Several of these unit cells were fabricated by wrapping wire around a rigid 3D-printed structure formed of ABS plastic, and measured in a finite parallel plate waveguide test structure designed and fabricated for that purpose. The measurements confirmed the broadband response for both the negative permeability and the negative permittivity cases. Sets of twelve unit cells in various combinations of orientations enabled measurement of a double-negative response. The contribution to the general body of knowledge that is presented in this chapter may be summarized as follows:

- **This chapter demonstrated through both simulation and measurement that the novel unit cells presented herein were capable of producing broadband negative permeability, negative permittivity, or negative index of refraction, through simple reorientation of the unit cells with respect to the incident electric field.**

Chapter 4 presented a patch antenna that was developed as a fractal expansion of the traditional rectangular microstrip patch. The traditional antenna geometry was modified through introduction of five gaps around the perimeter of the rectangle, creating five capacitively-coupled concentric rings. The feed of the antenna was designed using a microstrip transmission line that passed under the outer three rings to connect to the fourth ring. The effect of this modification was to induce four frequencies of resonance, rather than the ordinary single resonant frequency. All four of these

resonances were shown to occur at lower frequencies than that of the traditional patch antenna. Further, all four resonances were shown to have radiation patterns that were consistent both with one another and with that of a traditional patch antenna. Several additional simulations were performed to explore the effects of minor geometric modification on the number of resonances and their frequencies. This chapter demonstrated a simple technique for producing multiband behavior from a rectangular patch antenna, where each resonance supported a similar current pattern and produced a similar radiation pattern to a traditional rectangular patch antenna. Tunability of resonant frequencies and number of resonances through minor geometric modification was also demonstrated. The contribution to the general body of knowledge that is presented in this chapter may be summarized as follows:

- **This chapter demonstrated that multiple resonances could be induced in a rectangular patch antenna through introduction of concentric gaps around its perimeter. It also showed that the number of resonances, as well as their frequencies, could be tuned through simple geometric modification of the patch topology, all while maintaining the single-lobe broadside directivity pattern of a traditional rectangular patch antenna.**

Chapter 5 presented a modified WR-187 rectangular-waveguide-fed horn antenna that utilized spiral metamaterial loading in the mouth of the horn to achieve circular polarization. The handedness of the radiated wave was shown to be adaptable through reorientation of the metamaterial unit cells. For both orientations, this antenna

exhibited better than 2 dB axial ratio at the operative frequency of 3.26 GHz. In the first orientation, the gain of the left-hand circularly polarized wave was shown to be 11.4 dB at broadside, while the broadside cross-polarized gain was -18.4 dB. Similarly, for the second orientation, the broadside gain of the right-hand circularly polarized wave was shown to be 11.5 dB, while the broadside cross-polarized gain was -9.8 dB. The contribution to the general body of knowledge that is presented in this chapter may be summarized as follows:

- **This chapter demonstrated a rectangular-waveguide-fed antenna that produced circularly polarized radiation, and also showed that the handedness of the radiated wave was tunable through reorientation of the loading unit cells.**

REFERENCES

[1] Dwight L. Jaggard. Fractal electrodynamics. In H. N. Kritikos and D. L. Jaggard, editors, *Recent Advances in Electromagnetic Theory*, chapter 6, pages 183–224. Springer-Verlag, New York, 1990.

[2] David M. Pozar. *Microwave Engineering*. John Wiley & Sons, Inc., Hoboken, New Jersey, 4th edition, 2012.

[3] Constantine A. Balanis. *Antenna Theory*. John Wiley & Sons, Inc., Hoboken, New Jersey, 3rd edition, 2005.

[4] Sophocles J. Orfanidis. Electromagnetic waves and antennas. `http://www.ece.rutgers.edu/~orfanidi/ewa/ewa-2up.pdf`, 1999. Online; accessed 1-Nov-2016.

[5] Constantine A. Balanis. *Advanced Engineering Electromagnetics*. John Wiley & Sons, Inc., Hoboken, New Jersey, 2nd edition, 2012.

[6] V. G. Veselago. The Electrodynamics of Substances with Simultaneously Negative Values of ϵ and μ. *Soviet Physics Uspekhi*, 10:509, January 1968.

[7] J. B. Pendry. Negative refraction makes a perfect lens. *Phys. Rev. Lett.*, 85:3966–3969, Oct 2000.

[8] J.B. Pendry, A.J. Holden, D.J. Robbins, and W.J. Stewart. Magnetism from conductors and enhanced nonlinear phenomena. *Microwave Theory and Techniques, IEEE Transactions on*, 47(11):2075–2084, Nov. 1999.

[9] R. W. Ziolkowski. Design, fabrication, and testing of double negative metamaterials. *IEEE Transactions on Antennas and Propagation*, 51(7):1516–1529, July 2003.

[10] D. R. Smith, Willie J. Padilla, D. C. Vier, S. C. Nemat-Nasser, and S. Schultz. Composite medium with simultaneously negative permeability and permittivity. *Phys. Rev. Lett.*, 84:4184–4187, May 2000.

[11] R. A. Shelby, D. R. Smith, and S. Schultz. Experimental verification of a negative index of refraction. *Science*, 292(5514):77–79, 2001.

[12] R. DuHamel and F. Ore. Logarithmically periodic antenna designs. In *1958 IRE International Convention Record*, volume 6, pages 139–151, March 1958.

[13] D. Isbell. Log periodic dipole arrays. *IRE Transactions on Antennas and Propagation*, 8(3):260–267, May 1960.

[14] Benoit B. Mandelbrot. *The Fractal Geometry of Nature*. W. H. Freeman and Company, New York, 3rd edition, 1983.

[15] Lewis F. Richardson. The problem of contiguity. In Oliver M. Ashford, H. Charnock, P. G. Drazin, J. C. R. Hunt, P. Smoker, and Ian Sutherland, editors, *Collected Papers of Lewis Fry Richardson*, volume 2, pages 577–627. Cambridge University Press, Cambridge, UK, 1993. reprinted here from: *General Systems: Yearbook of the Society for General Systems Research*, volume VI, pages 140-187. Ann Arbor, MI, 1961.

[16] Benoit Mandelbrot. How long is the coast of Britain? statistical self-similarity and fractional dimension. *Science*, 156(3775):636–638, 1967.

[17] Wikimedia Commons. File:fractal broccoli.jpg — wikimedia commons, the free media repository. `https://commons.wikimedia.org/w/index.php?title=File:Fractal_Broccoli.jpg&oldid=177110818`, 2015. Online; accessed 26-September-2017.

[18] Wikimedia Commons. File:fern frond trichomes.jpg — wikimedia commons, the free media repository. `https://commons.wikimedia.org/w/index.php?title=File:Fern_Frond_Trichomes.jpg&oldid=142319756`, 2014. Online; accessed 26-September-2017.

[19] Helge von Koch. On a continuous curve without tangents constructible from elementary geometry. In Gerald A. Edgar, editor, *Classics on Fractals*, chapter 3, pages 25–45. Addison-Wesley Publishing Company, Boston, MA, 1993. translated from the French by Ilan Vardi.

[20] J. P. Gianvittorio and Y. Rahmat-Samii. Fractal antennas: a novel antenna miniaturization technique, and applications. *IEEE Antennas and Propagation Magazine*, 44(1):20–36, Feb 2002.

[21] C. Puente, J. Romeu, R. Pous, X. Garcia, and F. Benitez. Fractal multiband antenna based on the Sierpinski gasket. *Electronics Letters*, 32(1):1–2, Jan 1996.

[22] Carles Puente-Baliarda, Jordi Romeu, Rafael Pous, and Angel Cardama. On the behavior of the Sierpinski multiband fractal antenna. *IEEE Transactions on Antennas and Propagation*, 46(4):517–524, April 1998.

[23] C. Puente, J. Romeu, R. Bartoleme, and R. Pous. Perturbation of the Sierpinski antenna to allocate operating bands. *Electronics Letters*, 32(24):2186–2188, Nov 1996.

[24] S. R. Best. On the significance of self-similar fractal geometry in determining the multiband behavior of the Sierpinski gasket antenna. *IEEE Antennas and Wireless Propagation Letters*, 1(1):22–25, 2002.

[25] Junho Yeo and R. Mittra. Modified Sierpinski gasket patch antenna for multiband applications. In *Antennas and Propagation Society International Symposium, 2001. IEEE*, volume 3, pages 134–137 vol.3, July 2001.

[26] J. Romeu and J. Soler. Generalized Sierpinski fractal multiband antenna. *IEEE Transactions on Antennas and Propagation*, 49(8):1237–1239, Aug 2001.

[27] S. R. Best. Operating band comparison of the perturbed Sierpinski and modified Parany Gasket antennas. *IEEE Antennas and Wireless Propagation Letters*, 1(1):35–38, 2002.

[28] M. Naser-Moghadasi, R. A. Sadeghzadeh, T. Aribi, T. Sedghi, and B. S. Virdee. UWB monopole microstrip antenna using fractal tree unit-cells. *Microwave and Optical Technology Letters*, 54(10):2366–2370, October 2012.

[29] Javad Pourahmadazar, Changiz Ghobadi, and Javad Nourinia. Novel modified pythagorean tree fractal monopole antennas for UWB applications. *IEEE Antennas and Wireless Propagation Letters*, 10:484–487, May 2011.

[30] C. Puente, J. Romeu, R. Pous, J. Ramis, and A. Hijazo. Small but long Koch fractal monopole. *Electronics Letters*, 34(1):9–10, Jan 1998.

[31] C. P. Baliarda, J. Romeu, and A. Cardama. The Koch monopole: a small fractal antenna. *IEEE Transactions on Antennas and Propagation*, 48(11):1773–1781, Nov 2000.

[32] J. Pourahmadazar, C. Ghobadi, J. Nourinia, and H. Shirzad. Multiband ring fractal monopole antenna for mobile devices. *IEEE Antennas and Wireless Propagation Letters*, 9:863–866, 2010.

[33] Mahdi Jalali and Tohid Sedghi. Very compact UWB CPW-fed fractal antenna using modified ground plane and unit cells. *Microwave and Optical Technology Letters*, 56(4):851–854, 2014.

[34] Basak Ozbakis and Alp Kustepeli. The resonant behavior of the fibonacci fractal tree antennas. *Microwave and Optical Technology Letters*, 50(4):1046–1050, 2008.

[35] Lin Shu, Qiu Jinghui, Ren He, and Yang Caitian. A novel semi-circle fractal multi-band antenna. In *Systems and Control in Aerospace and Astronautics, 2008. ISSCAA 2008. 2nd International Symposium on*, pages 1–4, Dec 2008.

[36] J. S. Petko and D. H. Werner. Dense 3D fractal tree structures as miniature end-loaded dipole antennas. In *Antennas and Propagation Society International Symposium, 2002. IEEE*, volume 4, pages 94–97 vol.4, 2002.

[37] S. R. Best. On the resonant properties of the Koch fractal and other wire monopole antennas. *IEEE Antennas and Wireless Propagation Letters*, 1(1):74–76, 2002.

[38] V. Rajeshkumar and S. Raghavan. Bandwidth enhanced compact fractal antenna for uwb applications with 56 ghz band rejection. *Microwave and Optical Technology Letters*, 57(3):607–613, 2015.

[39] L. Ghanbari, S. Nikmehr, and M. Rezvani. A novel small UWB antenna using new fractal-like geometry. In *Applied Electromagnetics Conference (AEMC), 2011 IEEE*, pages 1–4, Dec 2011.

[40] Bahman Heydari, Zakarya Sanaati, Vorya Waladi, and Yashar Zehforoosh. A novel fractal monopole antenna with wide bandwidth enhancement for UWB applications. *Applied Computational Electromagnetics Society Journal*, 29(11):923–927, Nov 2014.

[41] Raj Kumar and Prem Narayan Chaubey. On the design of tree-type ultra wideband fractal Antenna for DS-CDMA system. *Journal of Microwaves, Optoelectronics and Electromagnetic Applications*, 11:107 – 121, 06 2012.

[42] J. S. Petko and D. H. Werner. Miniature reconfigurable three-dimensional fractal tree antennas. *IEEE Transactions on Antennas and Propagation*, 52(8):1945–1956, Aug 2004.

[43] J. Romeu and S. Blanch. A three dimensional Hilbert antenna. In *Antennas and Propagation Society International Symposium, 2002. IEEE*, volume 4, pages 550–553 vol.4, 2002.

[44] H. Elkamchouchi and M. A. Nasr. 3D-fractal rectangular Koch dipole and Hilbert dipole antennas. In *Microwave and Millimeter Wave Technology, 2007. ICMMT '07. International Conference on*, pages 1–4, April 2007.

[45] H. Elkamchouchi and M. A. Nasr. 3D-fractal Hilbert antennas made of conducting plates. In *Microwave and Millimeter Wave Technology, 2007. ICMMT '07. International Conference on*, pages 1–4, April 2007.

[46] H. Rmili, O. El Mrabet, J. M. Floc'h, and J. L. Miane. Study of an electrochemically-deposited 3-d random fractal tree-monopole antenna. *IEEE Transactions on Antennas and Propagation*, 55(4):1045–1050, April 2007.

[47] Kathryn L. Smith. The use of fractals and non-Foster circuits for wideband metamaterials and antennas. Master's thesis, University of North Carolina at Charlotte, Charlotte, N.C., U.S.A., 2015.

[48] K. L. Smith and R. S. Adams. A novel ultra-wideband fractal monopole antenna. In *2015 IEEE International Symposium on Antennas and Propagation USNC/URSI National Radio Science Meeting*, pages 2315–2316, July 2015.

[49] Nathan Cohen. Fractals' new era in military antenna design. *Journal of RF design*, 2005.

[50] R. H. Patnam. Broadband CPW-fed planar Koch fractal loop antenna. *IEEE Antennas and Wireless Propagation Letters*, 7:429–431, 2008.

[51] Rajeev Mathur1, Sunil Joshi, and Krishna C Roy. A novel multiband Koch loop antenna using fractal geometry for wireless communication system. *International Journal of Wireless & Mobile Networks*, 3(5):161–172, October 2011.

[52] M. Zeng, A. S. Andrenko, Hong-Zhou Tan, Chong Lu, and Xianluo Liu. Fractal loop antenna with novel impedance matching for rf energy harvesting. In *2016 Asia-Pacific International Symposium on Electromagnetic Compatibility (APEMC)*, volume 01, pages 966–968, May 2016.

[53] F. Arazm, R. K. Baee, C. Ghobadi, and J. Norinia. Square loop antenna miniaturization using new fractal geometry. In *Advanced Communication Technology, 2004. The 6th International Conference on*, volume 1, pages 164–169, Feb 2004.

[54] A. S. Andrenko. Conformal fractal loop antennas for RFID tag applications. In *2005 18th International Conference on Applied Electromagnetics and Communications*, pages 1–6, Oct 2005.

[55] Jaume Anguera, Carles Puente, Carmen Borja, Raquel Montero, and Jordi Soler. Small and high-directivity bow-tie patch antenna based on the Sierpinski fractal. *Microwave and Optical Technology Letters*, 31(3):239–241, 2001.

[56] J. Anguera, C. Puente, C. Borja, and R. Montero. Bowtie microstrip patch antenna based on the Sierpinski fractal. In *Antennas and Propagation Society International Symposium, 2001. IEEE*, volume 3, pages 162–165 vol.3, July 2001.

[57] P. Dehkhoda and A. Tavakoli. A crown square microstrip fractal antenna. In *IEEE Antennas and Propagation Society Symposium, 2004.*, volume 3, pages 2396–2399 Vol.3, June 2004.

[58] P. Dehkhoda and A. Tavakoli. Crown-Sierpinski microstrip antenna: further reduction of the size of a crown square fractal. In *2005 IEEE Antennas and Propagation Society International Symposium*, volume 1B, pages 247–250 vol. 1B, 2005.

[59] P. Athira and V.P. Joseph. Multiband fractal patch antenna: Modification and miniaturization of Sierpinski gasket. *International Journal of Science and Research*, 4(12):825–829, Dec 2015.

[60] S. Kohli, S. S. Dhillon, and A. Marwaha. Design and optimization of multiband fractal microstrip patch antenna for wireless applications. In *2013 5th International Conference and Computational Intelligence and Communication Networks*, pages 32–36, Sept 2013.

[61] R. Kumar, Y. B. Thakare, and M. Bhattacharya. Novel design of star shaped circular fractal antenna. In *Recent Advances in Microwave Theory and Applications, 2008. MICROWAVE 2008. International Conference on*, pages 239–241, Nov 2008.

[62] Yong Zhang, Bing-Zhong Wang, Xue-Song Yang, and Weixia Wu. A fractal Hilbert microstrip antenna with reconfigurable radiation patterns. In *2005 IEEE Antennas and Propagation Society International Symposium*, volume 3A, pages 254–257 vol. 3A, July 2005.

[63] D. H. Werner, R. L. Haupt, and P. L. Werner. Fractal antenna engineering: the theory and design of fractal antenna arrays. *IEEE Antennas and Propagation Magazine*, 41(5):37–58, Oct 1999.

[64] Douglas H. Werner, Pingjuan L Werner, Dwight L. Jaggard, Aaron D Jaggard, Carles Puente, and Randy L. Haupt. The theory and design of fractal antenna arrays. In Douglas H. Werner and Raj Mittra, editors, *Frontiers in Electromagnetics*, chapter 3, pages 94–203. IEEE Press, Piscataway, NJ, 2000.

[65] Dwight L. Jaggard and Aaron D. Jaggard. Fractal ring arrays. *Wave Motion*, 34(3):281 – 299, 2001. Electrodynamics in Complex Environments.

[66] Vandita Rajiv Pai Raikar. Metamaterial loading of electrically small patch antennas to enable beam steering up to the horizon. Master's thesis, University of North Carolina at Charlotte, Charlotte, N.C., U.S.A., 2015.

[67] A. Alu, F. Bilotti, N. Engheta, and L. Vegni. Subwavelength, compact, resonant patch antennas loaded with metamaterials. *IEEE Transactions on Antennas and Propagation*, 55(1):13–25, Jan 2007.

[68] T. Agrawal, S. Srivastava, and M. Dadel. Dual and triple band rectangular patch antenna using complementary split ring resonator (CSRR). In *2015 IEEE Applied Electromagnetics Conference (AEMC)*, pages 1–2, Dec 2015.

[69] F. Bilotti, A. Alu, N. Engheta, and L. Vegni. Miniaturized circular patch antenna with metamaterial loading. In *2006 First European Conference on Antennas and Propagation*, pages 1–4, Nov 2006.

[70] M. Li, K. M. Luk, L. Ge, and K. Zhang. Miniaturization of magnetoelectric dipole antenna by using metamaterial loading. *IEEE Transactions on Antennas and Propagation*, 64(11):4914–4918, Nov 2016.

[71] R. A. Shelby, D. R. Smith, and S. Schultz. Experimental verification of a negative index of refraction. *Science*, 292(5514):77–79, 2001.

[72] K. Buell, H. Mosallaei, and K. Sarabandi. A substrate for small patch antennas providing tunable miniaturization factors. *Microwave Theory and Techniques, IEEE Transactions on*, 54(1):135–146, Jan 2006.

[73] J. B. Pendry. Negative refraction makes a perfect lens. *Physical Review Letters*, 85(18):3966–3969, 2000.

[74] J. B. Pendry, D. Schurig, and D. R. Smith. Controlling Electromagnetic Fields. *Science*, 312(5781):1780–1782, 2006.

[75] D. Schurig, J. J. Mock, B. J. Justice, S. A. Cummer, J. B. Pendry, A. F. Starr, and D. R. Smith. Metamaterial Electromagnetic Cloak at Microwave Frequencies. *Science*, 314(5801):977–980, 2006.

[76] D.J. Gregoire, C.R. White, and J.S. Colburn. Wideband artificial magnetic conductors loaded with non–Foster negative inductors. *Antennas and Wireless Propagation Letters, IEEE*, 10:1586–1589, 2011.

[77] J. B. Pendry. Time Reversal and Negative Refraction. *Science*, 322(5898):71–73, 2008.

[78] Martin W. McCall, Alberto Favaro, Paul Kinsler, and Allan Boardman. A spacetime cloak, or a history editor. *Journal of Optics*, 13(2):024003.1–024003.9, February 2011.

[79] Ruopeng Liu, Aloyse Degiron, Jack J. Mock, and David R. Smith. Negative index material composed of electric and magnetic resonators. *Applied Physics Letters*, 90(26), 2007.

[80] L. Zhou, C. T. Chan, and P. Sheng. Theoretical studies on the transmission and reflection properties of metallic planar fractals. *Journal of Physics D Applied Physics*, 37:368–373, February 2004.

[81] F. Miyamaru, Y. Saito, M. W. Takeda, B. Hou, L. Liu, W. Wen, and P. Sheng. Terahertz electric response of fractal metamaterial structures. *Phys. Rev. B*, 77:045124, Jan 2008.

[82] K. L. Smith, R. S. Adams, and T. Weldon. A novel broadband fractal metamaterial unit cell. In *2014 IEEE Antennas and Propagation Society International Symposium (APSURSI)*, pages 549–550, July 2014.

[83] Xueqin Huang, Shiyi Xiao, Lei Zhou, Weijia Wen, C. T. Chan, and Ping Sheng. Photonic metamaterials based on fractal geometry. In Tie Jun Cui, David R. Smith, and Ruopeng Liu, editors, *Metamaterials: Theory, Design, and Applications*, chapter 10, pages 215–245. Springer, New York, 2010.

[84] V. Crnojevic-Bengin, V. Radonic, and B. Jokanovic. Complementary split ring resonators using square Sierpinski fractal curves. In *2006 European Microwave Conference*, pages 1333–1335, Sept 2006.

[85] M. Palandoken and H. Henke. Fractal spiral resonator as magnetic metamaterial. In *Applied Electromagnetics Conference (AEMC), 2009*, pages 1–4, Dec 2009.

[86] M. Palandoken and H. Henke. Fractal negative-epsilon metamaterial. In *Antenna Technology (iWAT), 2010 International Workshop on*, pages 1–4, March 2010.

[87] Juan D. Baena, Ricardo Marqués, Francisco Medina, and Jesús Martel. Artificial magnetic metamaterial design by using spiral resonators. *Phys. Rev. B*, 69:014402, Jan 2004.

[88] A. Kumar, J. Mohan, and H. Gupta. Microstrip patch antenna loaded with metamaterial for multiband applications. In *2016 International Conference on Signal Processing and Communication (ICSC)*, pages 43–47, Dec 2016.

[89] Lili Wang, Yue Zhang, and Pei Dong. Dual-band dipole antenna loaded with metamaterial based structure. In *2016 2nd IEEE International Conference on Computer and Communications (ICCC)*, pages 1728–1731, Oct 2016.

[90] M. A. Antoniades, S. A. Rezaeieh, and A. M. Abbosh. Bandwidth and directivity enhancement of metamaterial-loaded loop antennas for microwave imaging applications. In *2017 International Workshop on Antenna Technology: Small Antennas, Innovative Structures, and Applications (iWAT)*, pages 249–252, March 2017.

[91] N. V. Rajasekhar, H. Adhithya, and D. S. Kumar. Bandwidth enhancement of planar monopole antenna by loading metamaterial based via-less crlh unit cells. In *2016 IEEE Indian Antenna Week (IAW 2016)*, pages 29–33, June 2016.

[92] T. F. Khanum and S. Amit. A compact wideband Sierpinski antenna loaded with metamaterial. In *2016 International Conference on Electrical, Electronics, and Optimization Techniques (ICEEOT)*, pages 348–351, March 2016.

[93] Y. Cai, Y. Zhang, L. Yang, Y. Cao, and Z. Qian. Design of low-profile metamaterial-loaded substrate integrated waveguide horn antenna and its array applications. *IEEE Transactions on Antennas and Propagation*, 65(7):3732–3737, July 2017.

[94] Y. J. Zheng, J. Gao, Y. L. Zhou, X. Y. Cao, L. M. Xu, S. J. Li, and H. H. Yang. Metamaterial-based patch antenna with wideband rcs reduction and gain enhancement using improved loading method. *IET Microwaves, Antennas Propagation*, 11(9):1183–1189, 2017.

[95] J. Li, Q. Zeng, R. Liu, and T. A. Denidni. Beam-tilting antenna with negative refractive index metamaterial loading. *IEEE Antennas and Wireless Propagation Letters*, 16:2030–2033, 2017.

[96] S. Ahdi Rezaeieh, M. A. Antoniades, and A. M. Abbosh. Compact wideband loop antenna partially loaded with mu-negative metamaterial unit cells for directivity enhancement. *IEEE Antennas and Wireless Propagation Letters*, 15:1893–1896, 2016.

[97] Gopikrishnan G., Z. Akhter, and M. J. Akhtar. A novel corrugated four slot vivaldi antenna loaded with metamaterial cells for microwave imaging. In *2016 Asia-Pacific Microwave Conference (APMC)*, pages 1–4, Dec 2016.

[98] J. Tingyong and Z. Heng. Simulation and experiment study of horn antenna loaded with enz metamaterial. In *2016 11th International Symposium on Antennas, Propagation and EM Theory (ISAPE)*, pages 307–310, Oct 2016.

[99] A. J. Simmons. Phase shift by periodic loading of waveguide and its application to broad-band circular polarization. *IRE Transactions on Microwave Theory and Techniques*, 3(6):18–21, December 1955.

[100] X. Ma, C. Huang, W. Pan, B. Zhao, J. Cui, and X. Luo. A dual circularly polarized horn antenna in ku-band based on chiral metamaterial. *IEEE Transactions on Antennas and Propagation*, 62(4):2307–2311, April 2014.

[101] D. R. Smith, Willie J. Padilla, D. C. Vier, S. C. Nemat-Nasser, and S. Schultz. Composite medium with simultaneously negative permeability and permittivity. *Phys. Rev. Lett.*, 84(18):4184–4187, May 2000.

[102] J. B. Pendry. A chiral route to negative refraction. *Science*, 306(5700):1353–1355, 2004.

[103] K.L. Smith and R.S. Adams. A $\lambda_\circ/60$ spherical spiral metamaterial for negative permeability and negative permittivity. In *Antennas and Propagation Society International Symposium (APSURSI), 2016 IEEE*, 2016.

[104] Z. Szabó and, Gi-Ho Park, R. Hedge, and Er-Ping Li. A unique extraction of metamaterial parameters based on Kramers-Kronig relationship. *Microwave Theory and Techniques, IEEE Transactions on*, 58(10):2646–2653, Oct. 2010.

[105] S. Arslanagic, T.V. Hansen, N.A. Mortensen, A.H. Gregersen, O. Sigmund, R.W. Ziolkowski, and O. Breinbjerg. A review of the scattering-parameter extraction method with clarification of ambiguity issues in relation to metamaterial homogenization. 55(2):91–106, Apr. 2013.

[106] Constantine A. Balanis. *Antenna Theory*. John Wiley and Sons, Inc., 3rd edition, 2005.